THE UNIVERSITY OF CHICAGO

MOLECULAR BEAM EXPERIMENTS AND THEORETICAL STUDIES ON THE DYNAMICS AND PHOTOCHEMISTRY OF SEVERAL SMALL MOLECULES

A DISSERTATION SUBMITTED TO

THE FACULTY OF THE DIVISION OF THE PHYSICAL SCIENCES

IN CANDIDACY FOR THE DEGREE OF

DOCTOR OF PHILOSOPHY

DEPARTMENT OF CHEMISTRY

BY

PRESTON GARRIETH SCRAPE

CHICAGO, ILLINOIS

AUGUST 2017

TABLE OF CONTENTS

LIST OF FIGURES

LIST OF TABLES

ACKNOWLEDGMENTS

And on the pedestal these words appear:

'My name is Ozymandias, king of kings:

Look on my works, ye Mighty, and despair!'

Nothing beside remains. Round the decay

Of that colossal wreck, boundless and bare

The lone and level sands stretch far away.

—*Percy Shelley, "Ozymandias", 9-14.*

"The means by which we live are marvelous indeed. And yet something is missing. We have learned to fly the air like birds and swim the sea like fish, but we have not learned the simple art of living together as brothers. . . . The means by which we live have outdistanced the ends for which we live. Our scientific power has outrun our spiritual power. We have guided missiles and misguided men."

—*Martin Luther King, Jr., in "Strength to Love", speaking on Luke 12:20*

Space would fail me to mention everyone who contributed either to the work in this dissertation or to my professional development. We must content ourselves with an abbreviated list instead.

Many thanks are owed to Professor Laurie Butler, a wonderful advisor who gently pushes even the most trepidatious students to do great things. Thanks are also owed to Professor Gregory Engel, who provided further professional guidance and career advice.

I am glad to have worked with former students (now Doctors) Lei Wang, Matthew Brynteson, Ryan Booth, and Jonathan Adams, as well as postdoctoral researcher Martin Lam. Lei, Matt, and Ryan trained me in the use of scattering instruments; Jon and Martin, in imaging instruments. The scattering data in this dissertation were collected with the help of Lei, Matt, and Jon.

Jon Adams was my constant companion in the lab, and provided many helpful ideas and conversations. My undergraduate assistants Trevor Roberts, Rosalind Xu, and Jeremy Schroeder did great work in analyzing data and maintaining instrumentation.

I am deeply grateful to my many collaborators, without whom most of this work would have been impossible: Professors Yuan-Pern Lee, Shih-Huang Lee, and John Stanton, as well as their students and assistants.

Garth Moritz has been a friend and supporter since before the topic of graduate education even entered my mind. We walk together now on to our next adventure.

ABSTRACT

These experimental and computational studies characterize the dynamics and thermochemistry of several species that are important in atmospheric, combustion, and interstellar chemistry. The species are selected both as interesting problems in their own right, and as proxies that give insight into even more complex problems. In crossed laser-molecular beam experiments, this work probes the ultraviolet photochemistry of $BrCH_2CH_2ONO$ and CH_2Cl_2, revealing rich excited-state dynamics including the unexpected photoelimination of HNO from $BrCH_2CH_2ONO$ and an unusual trimodal kinetic energy release in HCl photoelimination from CH_2Cl_2. In the case of CH_2Cl_2, C-Cl photofission produces the CH_2Cl radical, allowing a first characterization of its photoionization cross section. $BrCH_2CH_2ONO$ also generates the open-shell nitrite CH_2CH_2ONO, which dissociates predominately via its lowest-barrier pathway to NO_2 + ethene; however, this radical evinces significant dissociation to HNO + vinoxy, even though the barrier to this process (calculated via the G4 method) is prohibitively high. This result implies a non-intrinsic reaction coordinate pathway to HNO that circumvents the classical transition state; thus, HNO production from nitrite radicals is likely a more important channel than was previously believed. In a theoretical study, this work develops a new model of energy partitioning in dissociation reactions that estimates the distribution of vibrational energy based solely on the intrinsic reaction coordinate surface; the predictions of this model agree quite well with experimental measurements in the case of HCl photoelimination from acryloyl chloride. Finally, in support of future dynamics studies, this work assesses a novel composite thermochemical protocol by calculating the singlet-triplet gap of CH_2 and the dissociation threshold of $(H_2O)_2$. The protocol agrees exceptionally well with experimental values, giving confidence that it may be applied to other systems.

CHAPTER 1

INTRODUCTION

1.1. Overview

Unimolecular dissociation of energized species is central to the chemistry of atmospheres, combustion mixtures, and interstellar space; yet many aspects of dissociation dynamics, as well as entire classes of energized species, remain mystifying. The following chapters describe experimental and theoretical efforts to elucidate the dynamics of specific energized molecules, both as interesting problems in their own right and as proxies to larger, more complex problems.

1.2. Chemical systems studied

1.2.1. Photochemistry of $BrCH_2CH_2ONO$ and dissociation of hot CH_2CH_2ONO

Gas-phase alkyl nitrites are important intermediates in the formation of chemical smog and in the regulation of ozone levels.[1-3] Recent work has suggested that these nitrites, in addition to the well-known NO and NO_2 loss channels, may also evolve HNO under collision-free conditions, opening up a new branch of possible reaction pathways.[4-8] The mechanism by which HNO might be produced, however, is unclear. Substituted alkyl nitrites, including alkyl nitrite radicals, have received less attention, even though they may exhibit vastly different dynamics than their closed-shell analogues (indeed, one conclusion of Chapter 2 is that they do so).

Chapter 2 explores the photodissociation at 193 nm of 2-bromoethyl nitrite, $BrCH_2CH_2ONO$, under collision-free conditions, as a prototypical substituted alkyl nitrite. The photodissociation also produces the radical CH_2CH_2ONO, allowing the study to probe the unimolecular dissociation of an

open-shell nitrite as well. Among other conclusions, this chapter reports intriguing evidence of unimolecular production of HNO from both nitrites: photochemical production of HNO from $BrCH_2CH_2ONO$, and dissociation of vibrationally hot CH_2CH_2ONO radical to HNO + vinoxy. The data and calculations strongly imply an unexpected non-intrinsic reaction coordinate mechanism leading to HNO from the radical.

1.2.2. Photochemistry of CH_2Cl_2 as a route to CH_2Cl

In Chapter 3, the photochemical dynamics of CH_2Cl_2 (dichloromethane) are studied, in particular as a route to produce the CH_2Cl (chloromethyl) radical. A key result of this chapter is a determination of the photoionization cross section of CH_2Cl at 13.7 eV. Methyl radicals and their derivatives are important intermediates in atmospheric and combustion processes: they participate in the formation and destruction of larger species and, in the stratosphere, they catalyze the decomposition of ozone.[1,9] Halogen-substituted methyl radicals such as CH_2Cl are generated by decomposition of organic solvents, as well as by the action of atmospheric Cl or Cl_2 on organic species; these radicals serve as sources of atomic halogens in addition to their usual functions.[10]

The photochemistry of CH_3Cl has been explored in detail by others.[11] However, the study in Chapter 3 shows that the additional halogen atom in CH_2Cl_2 leads to much greater complexity in the dynamical processes, seemingly due to the relative richness of the excited-state manifold (including the possibility of rapid intersystem crossing). These results will be useful for future theoretical studies that attempt to rigorously treat complex potential energy surface landscapes involving heavier atoms.

1.2.3. A post-transition state Franck-Condon model for estimating partitioning to product vibration in diatomic elimination

The partitioning of energy during a molecular dissociation into translations, rotations, and vibrations of the products is a key dynamical phenomenon that reflects the elementary quantum-chemical processes underlying chemical reactivity. However, there is currently no theoretical model that reliably estimates how the available energy will be partitioned. Chapter 4 describes a new model that estimates the vibrational energy of a departing diatomic fragment in a dissociation with a substantial exit barrier. The only input required by the model is a calculated intrinsic reaction coordinate surface; thus, it has the advantages of being computationally efficient, general in scope, and free of empirical parameters. This model will be useful in larger studies of gas-phase mixtures where the energy distribution among the dissociation products is key to the subsequent dynamics.

By way of example, the model is applied to the photodissociation of acryloyl chloride, $CH_2CHC(O)Cl$, at 193 nm. This species exhibits rich photochemistry due to its enone (C=C-C=O) group and chloride moiety; one product channel at this wavelength is HCl photoelimination. Based on *ab initio* calculations and experimental data,[12] the study in Chapter 4 first shows that the mechanism of HCl photoelimination begins with internal conversion to the ground state; dissociation on the ground state then occurs via two different channels. It is then shown that the new model qualitatively predicts the vibrational energy imparted to the HCl fragments formed in the two dissocaition channels.

1.2.4. Thermochemistry of CH_2 and $(H_2O)_2$

Thermochemical calculations are indispensable to computational studies of chemical dynamics. The quality of predictive kinetic and dynamic models depends in part on the accuracy of

calculated heats of formation and barrier heights, especially when the energetic budget of the reacting species has a narrow distribution, as in ultracold reactions or monochromatic photochemistry. Chapter 5 assesses the strengths and robustness of a composite thermochemical protocol known as "high-accuracy extrapolated *ab initio* thermochemistry" (HEAT)[13-15] by applying the protocol to two classic chemical problems: the singlet-triplet gap of CH_2, and the dissociation energy of the water dimer. The protocol is found to perform remarkably well, matching the best experimental results to within 0.5 kJ/mol; at the same time, the protocol is less computationally expensive than previous methods that reached the same level of accuracy. These results show that the HEAT protocol is well-suited to provide enthalpies for dynamics studies.

1.3. Methods

1.3.1. Crossed laser-molecular beam scattering apparatus

All of the data in Chapters 2 and 3 were collected using the crossed laser-molecular beam scattering instrument at the U9 endstation of the National Synchrotron Radiation Research Center in Hsinchu, Taiwan. The instrument consists of a rotating source chamber with a heated pulsed nozzle that fires a molecular beam of the species of interest (~2% by weight in neon) into a larger main chamber. The source chamber is set at an angle with respect to the axis of the detector for all photodissociation experiments. The molecular beam is then crossed perpendicularly with a laser beam focused to an area of ~12 mm^2 at its intersection with the molecular beam. After photodissociation by the laser, those fragments with net velocity vectors (the vector sum of the precursor molecule's velocity and the velocity imparted to recoiling fragments of photodissociation and secondary dissociation) pointing along the axis of the detector travel 10.05 cm to enter the detector's ionizer, where they are photoionized by tunable VUV radiation from the synchrotron. This

synchrotron output is first passed through an argon gas cell to filter out higher harmonics. Ionized fragments are then propelled by a series of ion lenses through a quadrupole mass filter, and finally the mass-filtered ions are counted in a Daly detector. The time-dependent ion signal is binned by a multichannel scaler in 1 μs intervals measured from the time of the laser shot; the flight time of the ions is calculated using the calibrated ion flight constant of the detector, 5.43 μs amu$^{-1/2}$.

The internal energy distribution, $E_{int}(R)$, of a radical R arising from photodissociation of a precursor R-X is calculated by conservation of energy:

$$E_{int}(R\text{-}X) + h\nu = \Delta H_{0K} + E_T + E_{int}(R) + E_{int}(X) \quad (1)$$

where $E_{int}(R\text{-}X)$ is the internal energy of the precursor, $h\nu$ is the photon energy, E_T is the recoil kinetic energy imparted to the photoproducts, and $E_{int}(R)$ and $E_{int}(X)$ are the internal energies of the departing fragments R and X. In these experiments, supersonic expansion of the precursor cools molecular rotations, so $E_{int}(R\text{-}X)$ is simply the thermal vibrational energy at the nozzle temperature of 60 °C. The energy of the laser photons is known. The value of ΔH_{0K} is calculated using electronic structure theory. Recoil kinetic energy distributions, $P(E_T)$, were derived by forward convolution fitting: the $P(E_T)$s for all dissociations were iteratively adjusted to make the forward-convolution prediction of neutral flight times well-fitted to the experimentally observed neutral flight times at all masses. Recoil kinetic energy distributions for all dissociation events were fitted to the TOF spectra by forward convolution fitting using the CMLAB2 program.[17]

1.3.2. The HEAT protocol

The high-accuracy *ab initio* protocol of Chapter 5 includes several terms summed together. The total energy of a species within the HEAT paradigm is calculated as the sum:

$$E_{\mathrm{HEAT}} = E_{\mathrm{HF}}^{\infty} + \Delta E_{\mathrm{CCSD(T)}}^{\infty} + \Delta E_{\mathrm{CCSDT}} + \Delta E_{\mathrm{HLC}} + \Delta E_{\mathrm{REL}} + \Delta E_{\mathrm{ZPE}} + \Delta E_{\mathrm{DBOC}} \quad (2)$$

Here E_{HF}^{∞} is the Hartree-Fock energy, extrapolated to the complete basis set limit via a three-point method using the basis sets aug-cc-pCVXZ, with either X = T, Q, and 5 or X = Q, 5, and 6. $\Delta E_{\mathrm{CCSD(T)}}^{\infty}$ is the electronic correlation energy calculated by CCSD(T) (not the total CCSD(T) energy), which is extrapolated by a two-point method using the basis sets aug-cc-pCVXZ, with X = Q and 5 or X = 5 and 6 for HEAT456. $\Delta E_{\mathrm{CCSDT}}$ is a frozen-core correction to the CCSD(T) energy, obtained by calculating the difference between the frozen-core CCSD(T) and CCSDT energies. The extrapolation to the complete basis-set limit is performed using cc-pVTZ and cc-pVQZ basis sets.

ΔE_{HLC} is a frozen-core "high-level correlation" correction, obtained by calculating the difference between the frozen-core CCSDT and higher-level CC energies. Due to the computational expense of high-level correlation, only CCSDTQ and CCSDT(Q) are typically used; in this study, however, CCSDTQPH is also used for methylene, to investigate whether the inclusion of such a high level of correlation is useful. ΔE_{REL} is a correction for scalar relativistic effects, which is calculated at the CCSD(T)/aug-cc-pCVTZ level of theory. This correction includes one-electron mass-velocity terms and one- and two-electron Darwin terms.

ΔE_{ZPE} is the zero-point vibrational energy, calculated at the CCSD(T)/cc-pVQZ level of theory. The zero-point energy includes a treatment of anharmonicity via second-order vibrational perturbation theory.

Finally, ΔE_{DBOC} is the diagonal Born-Oppenheimer correction, which is a first-order correction to the Born-Oppenheimer approximation. In this study, ΔE_{DBOC} it is calculated at both the HF/aug-cc-pVTZ and CCSD/aug-cc-pCVQZ levels of theory; in the case of CH_2 it is moreover calculated at the CCSDT level of theory, using the aug-cc-pCVQZ basis set.

Molecular geometries were optimized at the CCSD(T)/cc-pVQZ level of theory. RHF reference wavefunctions were used for $^1CH_2$, H_2O, and $(H_2O)_2$; UHF references were used for $^3CH_2$.

1.4. References

1. Wayne, R. P. *Chemistry of Atmospheres*, 3rd ed. Oxford: Oxford University Press, 2000.

2. Calvert, J. G.; Pitts, J. N., Jr. *Photochemistry*. New York: Wiley, 1966.

3. McMillan, G. R.; Kumari, J.; Snyder, D. L. The Photolysis and Photooxidation of Alkyl Nitrites. In Tuesday, C. S., ed., *Chemical Reactions in Urban Atmospheres*, New York: Elsevier, 1971, pp. 35-43.

4. Zhu, R. S.; Raghunath, P.; Lin, M. C. Effect of Roaming Transition States upon Product Branching in the Thermal Decomposition of CH_3NO_2. *J. Phys. Chem. A* **2013**, *117*, 7308−7313.

5. Homayoon, Z.; Bowman, J. M. Quasiclassical Trajectory Study of CH_3NO_2 Decomposition via Roaming Mediated Isomerization Using a Global Potential Energy Surface. *J. Phys. Chem A* **2013**, *117*, 11665-11672.

6. Bowman, J. M. Roaming. *Mol. Phys.* **2014**, *112*, 2516-2528.

7. Prozument, K.; Suleimanov, Y. V.; Buesser, B.; Oldham, J. M.; Green, W. H.; Suits, A. G.; Field, R. W. A Signature of Roaming Dynamics in the Thermal Decomposition of Ethyl Nitrite: Chirped-Pulse Rotational Spectroscopy and Kinetic Modeling. *J. Phys. Chem. Lett.* **2014**, *5*, 3641-3648.

8. Liu, Y.; Li, X.; Tian, G.; Li, X.; Sun, Z. Theoretical Study on the Reaction Mechanism of CH_3CH_2O Radical with NO. *Comp. Theoret. Chem.* **2014**, *1032*, 84-89.

9. Finlayson-Pitts, B. J.; Pitts, J. N. *Chemistry of the Upper and Lower Atmosphere: Theory, Experiments, and Applications*. Academic: New York, 1999.

10. Tsang, W. Mechanisms for the formation and destruction of chlorinated organic products of incomplete combustion. *Combust. Sci. Technol.* **1990**, *74*, 99-116.

11. Lin, J. J.; Chen, Y.; Lee, Y. Y.; Lee, Y. T.; Yang, X. Photodissociation Dynamics of CH_3Cl at 157.6 nm: Evidence for $CH_2(\tilde{X}^3B_1/\tilde{a}^1A_1)$+HCl Product Channels. *J. Chem. Phys. Lett.* **2002**, *361*,

374−382.

12. Lee, P.-W.; Scrape, P. G.; Butler, L. J.; Lee, Y.-P. Two HCl-Elimination Channels and Two CO-Formation Channels Detected with Time-Resolved Infrared Emission upon Photolysis of Acryloyl Chloride [$CH_2CHC(O)Cl$] at 193 nm. *J. Phys. Chem. A* **2015**, *119*, 7293-7304.

13. Tajti, A.; Szalay, P. G.; Császár, A. G.; Kállay, M.; Gauss, J.; Valeev, E. F.; Flowers, B. A.; Vásquez, J.; Stanton, J. F. HEAT: High accuracy extrapolated ab initio thermochemistry. *Journal of Chemical Physics* **2004,** *121*, 11599-11613.

14. Bomble, Y. J.; Vásquez, J.; Kállay, M.; Michauk, C.; Szalay, P. G.; Császár, A. G.; Gauss, J.; Stanton, J. F. High-accuracy extrapolated ab initio thermochemistry. II. Minor improvements to the protocol and a vital simplification. *Journal of Chemical Physics* **2006,** *125*, 064108.

15. Harding, M. E.; Vásquez, J.; Ruscic, B.; Wilson, A. K.; Gauss, J.; Stanton, J. F. High-accuracy extrapolated ab initio thermochemistry. III. Additional improvements and overview. *Journal of Chemical Physics* **2008,** *128*, 114111.

CHAPTER 2

DISSOCIATION PATHWAYS OF THE CH_2CH_2ONO RADICAL: NO_2 + ETHENE, NO + OXIRANE, AND A NON-INTRINSIC REACTION COORDINATE HNO + VINOXY PATHWAY

This work was previously published in: Scrape, P. G.; Roberts, T. D.; Lee, S.-H.; Butler, L. J. *J. Phys. Chem. A* **2016**, *120*, 4973–4987, copyright 2016 American Chemical Society. Reproduced with permission. A new and expanded version of Figure 2.3, which includes more stationary points on the potential energy surface, is provided in Appendix A.

2.1. Introduction

Gaseous alkyl nitrites (R-ONO, where R is an alkyl group) are important intermediates in the formation of chemical smog and in the regulation of ozone levels.[1-3] Both photolysis and thermal decomposition of these species are rapid; photolysis under ultraviolet light occurs readily via photoabsorption in the nitrite moiety, which has absorption bands near 350 nm and 200 nm. The atmospheric impact of alkyl nitrite chemistry and photochemistry has motivated studies on nitrous acid (HONO),[4-7] methyl nitrite (CH_3ONO),[8-15] and a number of higher nitrites.[16-24]

A common reaction pathway is dissociation to an alkoxy radical and nitric oxide, RONO $\longrightarrow$ RO + NO.[2,3] In studies of the bulk kinetics of alkyl nitrites, nitrosoalkyl products (R-NO) are also observed, and the primary and secondary nitrites moreover evolve HNO + aldehyde or ketone.[19-21] A disproportionation mechanism for these pathways has been proposed, in which nascent NO radicals recombine with nascent alkoxy radicals, leading either to H-atom abstraction or C-C bond cleavage:[3,22,23]

$$\text{R-CH}_2\text{ONO} \longrightarrow \text{R-CH}_2\text{O}\cdot + \cdot\text{NO} \quad (1)$$

$$\text{R-CH}_2\text{O}\cdot + \cdot\text{NO} \longrightarrow \text{R-CHO} + \text{HNO} \quad (2)$$

$$\text{R-(CHO}\cdot\text{)-R`} + \cdot\text{NO} \longrightarrow \text{R-CHO} + \text{R`-NO} \quad (3)$$

There is also recent evidence of a unimolecular mechanism for HNO elimination. Zhu et al. have reported a roaming-mediated transition state for this process in methyl nitrite,[13] and Liu et al. did likewise for ethyl nitrite.[25] Homayoon and Bowman calculated a global potential energy surface for nitromethane and conducted a quasiclassical trajectory study on this surface;[14,15] they observed roaming trajectories leading to HNO from methyl nitrite (an isomer of nitromethane), mediated by the existence of a loosely-bound van der Waals complex. Experimentally, Prozument et al. studied the pyrolysis of ethyl nitrite, concluding based on their data and a reaction mechanism model that the molecule evolves HNO by a unimolecular roaming mechanism.[24] One of the goals of the present study was to probe HNO production under collision-free conditions in photoexcited and vibrationally excited substituted nitrites.

Substituted alkyl nitrites, in which one or more H are replaced by another functional group such as a halogen (F, Cl, Br), pseudo halogen (OH), or radical center, are an interesting special case that has received less attention. The photochemistry of haloalkyl nitrites may differ from that of alkyl nitrites, for instance because of competition between absorption in the halogen and nitrite chromophores. The prevalence of halocarbons and atomic halogens in arctic and marine atmospheres[26,27] suggests that haloalkoxy and haloalkyl nitrite chemistry may be significant in those regions. There is also recent evidence of significant inland sources of Cl.[28] Hydroxyalkoxy radicals (HO-R-O), related to hydroxyalkyl nitrites by the mechanisms described previously, appear in the atmospheric oxidation of alkenes.[29] Radicals of alkyl nitrites are formed by addition of NO_2 to a C=C double bond,[30] and evince an unexpected absorption band at visible

wavelengths that is not present in the closed-shell nitrites.[18,30]

The work reported here explores the photodissociation at 193 nm of 2-bromoethyl nitrite, $BrCH_2CH_2ONO$, under collision-free conditions, as a prototypical substituted alkyl nitrite. The photodissociation also produces the radical CH_2CH_2ONO (2-nitrosooxy ethyl), allowing us to probe the unimolecular dissociation of that species as well. This is an extension and conclusion of three previous studies of $BrCH_2CH_2ONO$ by Chhantyal-Pun et al.[31] and Wang et al.[32] at 351/355 nm, and by Wang et al. at 193 nm.[33] Photodissociation of this molecule at 351/355 nm was found to proceed through O-NO bond fission, leading to the products NO + $BrCH_2CH_2O$.[31,32] No competition from either C-Br photofission or HBr photoelimination was observed; unimolecular dissociation to HNO was not considered. Photodissociation at 193 nm was found to proceed through both O-NO and C-Br bond fission, with a branching ratio between the two channels on the order of 4:1.[33] That study characterized the O-NO and C-Br primary photodissociation channels, as well as the secondary dissociation of vibrationally excited $BrCH_2CH_2O$ following O-NO bond photofission, by 200 eV electron ionization detection of photoproducts. Moreover, the angular momentum of the CH_2CH_2ONO product following C-Br bond photofission was predicted by conservation of angular momentum using the measured Br photofragment velocity.

Herein, we present evidence of photoelimination of the $BrCH_2CH_2ONO$ precursor leading to HNO + $BrCH_2CHO$, and dissociation of the vibrationally excited CH_2CH_2ONO radical (formed in C-Br photofission) to HNO + vinoxy. We also complement the previous study at 193 nm by characterizing all the secondary dissociation channels of CH_2CH_2ONO using tunable VUV photoionization detection. These results are presented in Sections 2.3.2 and 2.3.3. It was moreover necessary to analyze several other dissociation channels of the precursor and

products, including multiphoton dissociations; we report the most interesting of these results in Sections 2.3.4 and 2.3.5, and provide the remainder of the data and analysis in Appendix A. Moreover, we slightly refine a few of the conclusions of the work by Wang et al. in light of the new results of this study.

2.2. Methods

2.2.1. Preparation of 2-bromoethyl nitrite ($BrCH_2CH_2ONO$)

The photolytic precursor, $BrCH_2CH_2ONO$, was synthesized by the usual method of mixing the corresponding alcohol with sulfuric acid and sodium nitrite. We followed the same procedure as was used in the previous studies.[31-33] In short, 100 mL of aqueous $NaNO_2$ (4 M concentration) was cooled to 0 °C in an ice bath; to this solution was added a mixture of 0.4 mol $BrCH_2CH_2OH$, 0.2 mol concentrated H_2SO_4, and 7 mL H_2O, dropwise over 20 minutes with constant stirring. The organic layer of the product, containing $BrCH_2CH_2ONO$, was collected by separation from the aqueous layer; no further purification was performed. The product was stored in dry ice and used within one week.

2.2.2. Crossed laser-molecular beam scattering apparatus

All data in this chapter were collected at the National Synchrotron Radiation Research Center (NSRRC) in Hsinchu, Taiwan, using the U9 Chemical Dynamics Beamline and a crossed laser-molecular beam scattering apparatus. This apparatus has been described in detail elsewhere.[34-36] A molecular beam of $BrCH_2CH_2ONO$ was created by first seeding the pure liquid, held at -10 °C, to its equilibrium vapor pressure in neon. The total backing pressure was approximately 600 torr. The gas mixture was supersonically expanded into a rotating source

chamber through a pulsed nozzle operating at 100 Hz, which was held at 60 °C to inhibit the formation of nitrite clusters. The rotating source was set at an angle of 15° with respect to the axis of the detector for all photodissociation experiments. The resulting molecular beam was then crossed perpendicularly with the unpolarized 193 nm output of a LPF 200 Lambda Physik Laser Technik laser, timed to fire approximately 240 μs after the nozzle so as to intersect the most dense region of the molecular beam pulse. The laser beam was focused to an area of ~12 mm^2 at its intersection with the molecular beam, and the pulse energy was maintained near 40 mJ.

After photodissociation, those fragments with net velocity vectors (the vector sum of the precursor molecule's velocity and the velocity imparted to recoiling fragments of photodissociation and secondary dissociation) pointing along the axis of the detector traveled 10.05 cm to enter the detector's ionizer, where they were photoionized by tunable VUV radiation from the synchrotron. This synchrotron output was first passed through a 7 cm gas cell containing ~10 torr of argon to filter out higher harmonics. Ionized fragments were then propelled by a series of ion lenses through a quadrupole mass filter, and finally the mass-filtered ions were counted in a Daly detector. The time-dependent ion signal was binned by a multichannel scaler in 1 μs intervals measured from the time of the 193 nm laser shot, so this signal included both the neutral and ion flight times. The neutral flight time is recovered from the total by subtracting the ion's flight time, which is calculated using the calibrated ion flight constant of 5.43 μs $amu^{-1/2}$; all of the time-of-flight (TOF) spectra in this report show only the neutral flight time.

Recoil kinetic energy distributions ($P(E_T)$s) for all dissociation events were fitted to the TOF spectra by forward convolution fitting using the CMLAB2 program.[37] The molecular beam velocity, which contributes to the fragments' net velocity vectors, was characterized using the

photodepletion (hole-burning) method: the rotating source chamber was set on-axis with the detector and the laser was operated at 50 Hz instead of 100 Hz, so that only one half of all molecular beam pulses underwent photodissociation. Subtraction of the "laser-on" ion signal from the "laser-off" ion signal gives the TOF distribution of the part of the molecular beam that photodissociates, which is easily transformed to a velocity distribution. Typical beam speeds were on the order of 700 m/s.

2.2.3. Computational methods

All geometries and energies were calculated at the G4//B3LYP/6-311++G(3df,2p) level of theory using the Gaussian 09 software package.[38] All energies are zero-point corrected, and only the ground electronic state of each species is considered. Molecular geometries were rendered in the MOLDEN program.[39] To predict the rotational and vibrational energy imparted to nascent CH_2CH_2ONO radicals, and to obtain a first guess for the angular distribution of secondary dissociations from this radical, we used a model based on conservation of angular momentum and the observed C-Br primary photofission $P(E_T)$, described in detail elsewhere.[40-42]

2.3. Results

2.3.1. Overview

In the following subsections we present time-of-flight data, derived recoil kinetic energy distributions, and angular distributions for fragments arising from primary and secondary dissociation events. By "primary photodissociation" we refer to the dissociation of the $BrCH_2CH_2ONO$ precursor to two products upon absorption of a 193 nm photon; subsequent unimolecular dissociation of the nascent vibrationally excited photoproducts are termed

"secondary dissociation". The key results of this study are found in Section 2.3.2, in which we characterize the primary photodissociation channels including HNO photoelimination, and in Section 2.3.3, in which we examine the title system. For completeness, Sections 2.3.4 and 2.3.5 describe dissociation channels of the primary $BrCH_2CHO$ and $BrCH_2CH_2O$ photofragments, including multiphoton effects; these channels contribute to the signal at m/e=79 (Br^+) and m/e=43 (vinoxy cation). Additional data and analysis that may be of interest to some readers are supplied in Appendix A.

Our results indicate that three primary photodissociation pathways occur upon irradiation at 193 nm:

$$BrCH_2CH_2ONO + h\nu \longrightarrow BrCH_2CHO + HNO \quad (4)$$

$$\Delta H_{0K} = 10.3 \text{ kcal/mol}$$

$$BrCH_2CH_2ONO + h\nu \longrightarrow Br\bullet + \bullet CH_2CH_2ONO \quad (5)$$

$$\Delta H_{0K} = 68.8 \text{ kcal/mol}$$

$$BrCH_2CH_2ONO + h\nu \longrightarrow BrCH_2CH_2O\bullet + \bullet NO \quad (6)$$

$$\Delta H_{0K} = 39.0 \text{ kcal/mol}$$

As was noted by Wang et al.,[33] $BrCH_2CH_2ONO$ has multiple conformers: the C-Br bond may be *anti* or *gauche* with respect to the C-O bond, and the terminal N=O bond may be *cis* or *trans* with respect to the C-C bond. Analogously, each of $BrCH_2CH_2O$, $BrCH_2CHO$, and CH_2CH_2ONO has multiple conformers. The (zero-point corrected) enthalpies of the reactions shown in eqs. 4, 5, and 6 were calculated using the lowest-energy conformer of each species. The barriers to interconversion are low, on the order of a few kcal/mol, so we expect nontrivial populations of each possible conformer in these experiments. Our results should therefore be considered a population-weighted average of the photochemistry of the individual conformers.

The products of primary photodissociation are formed with a range of internal energies. In our discussions of secondary dissociation, we compare the internal energy of a product to the energetic barriers along its potential energy surface to assess which dissociation pathways are energetically favorable. The internal energy distribution, $E_{int}(R)$, of a radical R arising from photodissociation of a precursor R-X (herein, $BrCH_2CH_2ONO$) is calculated by conservation of energy:

$$E_{int}(R\text{-}X) + h\nu = \Delta H_{0K} + E_T + E_{int}(R) + E_{int}(X) \qquad (7)$$

where $E_{int}(R\text{-}X)$ is the internal energy of the precursor, $h\nu$ is the photon energy, E_T is the recoil kinetic energy imparted to the photoproducts, and $E_{int}(R)$ and $E_{int}(X)$ are the internal energies of the departing fragments R and X. In these experiments, supersonic expansion of the precursor cools molecular rotations, so $E_{int}(BrCH_2CH_2ONO)$ is simply the thermal vibrational energy at the nozzle temperature of 60 °C, which we calculate as 3 kcal/mol. The energy of a 193 nm photon is $h\nu$ = 147.8 kcal/mol. For a primary photodissociation process, the value of ΔH_{0K} is one of those given in eqs. 4, 5, or 6. Recoil kinetic energy distributions, $P(E_T)$, were derived by forward convolution fitting: the $P(E_T)$s for all dissociations were iteratively adjusted to make the forward-convolution prediction of neutral flight times well-fitted to the experimentally observed neutral flight times at all masses. $E_{int}(X)$ is the internal energy of the cofragment X of species R; this term is discussed for X = Br, NO, and HNO in the relevant sections below.

In much of the data, there is a broad signal beginning at a neutral flight time of approximately 100 μs, rising to a peak near 220 μs. The signal does not depend on the 193 nm laser pulse, so it is assuredly not from any photodissociation event, including photodissociation of clusters; we therefore attribute it to time-dependent background from the scattered molecular beam pulse. (The data in this study show no observable contribution from photodissociation of

clusters, because the appearance energy of daughter ions from photoionization of $BrCH_2CH_2ONO$ is higher than the photon energy used. Wang et al., in their prior study at 193 nm using 200 eV electron bombardment ionization, observed a significant amount of signal from photodissociation of clusters.) This signal causes no complications for the analysis of most fragments, as it is typically either too far from the photofragment peaks to overlap them, or else is insignificantly small. In three cases (namely at m/e=29, 30, and 44), it was helpful to collect background data with the laser off and subtract that background from the "laser-on" data to eliminate the background that overlapped the product signals. In all of the figures below, we show the data with no background subtraction; the "laser-off" signal and background-subtracted data are provided in Appendix A.

2.3.2. Primary photodissociation channels of $BrCH_2CH_2ONO$

2.3.2.1. Primary photodissociation leading to Br + CH_2CH_2ONO

Primary C-Br photofission was characterized by the TOF data at m/e=79 (Br^+) shown in Figure 2.1, collected at a synchrotron energy of 15.34 eV. The forward convolution fit corresponding to primary Br is depicted as a solid brown line peaking near 55 μs; the $P(E_T)$ for this fit is given in Figure 2.2 as a brown line, which extends from approximately 15 kcal/mol to approximately 45 kcal/mol, with a maximum near 30 kcal/mol. (This experiment could not distinguish the spin-orbit states of Br nor the conformers of $BrCH_2CH_2ONO$. For this reason, the $P(E_T)$ should be considered an ensemble average.) Other contributions to the signal are: dissociative ionization of primary $BrCH_2CHO$ (Section 2.3.2.2), fitted as a solid green line; dissociative ionization of $BrCH_2CHO$ formed by dissociation of $BrCH_2CH_2O$, discussed in Appendix A and fitted as a solid blue line; photodissociation of the secondary CH_2Br fragment

from primary $BrCH_2CH_2O$, discussed in Section 2.3.5.2 and fitted as a dashed purple line; and secondary photodissociation of primary $BrCH_2CHO$, the co-fragment of HNO, discussed in Section 2.3.4.1 and fitted as a dashed blue line.

Primary C-Br photodissociation was first observed in the previous study at 193 nm by Wang et al.[33] The distribution of recoil kinetic energy, $P(E_T)$, imparted to the C-Br photofission products reported by Wang et al. differs slightly from that in Figure 2.2: theirs is overall slower by a few kcal/mol, extending from approximately 10 kcal/mol to approximately 40 kcal/mol, with a maximum just under 30 kcal/mol. This disagreement is explained in Section 2.3.5.1; briefly, it is an artifact of the large signal due to nitrite clusters in the previous experiment, which interfered with analysis of the data at m/e=93 (CH_2Br^+).

The CH_2CH_2ONO radical co-fragment from C-Br photofission is formed with a range of internal energies determined by conservation of energy; key stationary points along its potential energy surface are plotted in Figure 2.3. The lowest barrier to dissociation is a transition state 11.1 kcal/mol higher in energy than the *trans* conformer, which leads to the products NO_2 + ethene. Given the $P(E_T)$ of Figure 2.2, assuming that all of the Br is formed in its ground $^2P_{3/2}$ spin-orbit state, and letting ΔH_{0K} = 68.7 kcal/mol (the endoergicity of transformation from the lowest-energy conformer of $BrCH_2CH_2ONO$ to the lowest-energy conformer of the radical), the radicals are formed with an internal energy ranging from 38 to 68 kcal/mol (see the conservation-of-energy equation, eq. 7). As was noted in the previous study, a significant fraction of this E_{int} is partitioned into rotation. To estimate the amount of vibrational energy in these fragments, we use a model based on conservation of angular momentum, described previously.[40-42] Briefly, this model assumes that the dissociating molecule behaves essentially classically, with the departing Br applying an instantaneous impulse along the C-Br bond, which

produces the measured kinetic energy release of the dissociation. The angular momentum of the CH_2CH_2ONO "moiety" is readily calculated from the measured velocity imparted to the Br atom from the impulsive force (because linear and total angular momentum is conserved) and mapped onto the minimum-energy geometry of the CH_2CH_2ONO radical. The rotational energy E_{rot} of the radical is calculated from its angular momentum, and then its vibrational energy is simply $E_{vib} = E_{int} - E_{rot}$. The model then accounts for thermal vibrational energy in the precursor by repeating this calculation at several geometries along a normal vibrational mode of $BrCH_2CH_2ONO$. Due to thermal vibration, each E_T leads to many values of E_{vib}, the latter depending on the molecular geometry at the moment of impulse.

We require additional assumptions to apply this model to $BrCH_2CH_2ONO$. First, since both the precursor and the radical have *trans*-ONO and *cis*-ONO conformers, we assume that both of the *trans* conformers of the precursor photodissociate to the *trans* conformer of the radical, and likewise for the *cis* configuration (noting that, in both the precursor and the radical, the terminal NO may lie in or out of the plane of the CCO atoms). This association seems eminently reasonable, as alkyl bromides excited at 193 nm access a repulsive excited state, so the ONO moiety might be expected not to isomerize on the time scale of the dissociation. Second, we assume that the six conformers of the precursor are thermally populated at the nozzle temperature. Third, since this experiment is unable to determine the branching ratio between the two spin-orbit states of bromine (which differ in energy by 10.5 kcal/mol), we derive the vibrational energy distribution for CH_2CH_2ONO radicals assuming they are formed in co-incidence with $Br(^2P_{3/2})$. This assumption leads us to predict a higher average E_{vib} than if $Br(^2P_{1/2})$ were also considered.

The predictions of our model for the partitioning of E_{int} between rotation and vibration

are included in Figure 2.2 and Figure 2.3. Overlaid on Figure 2.3 is the predicted $P(E_{vib})$, a statistical average of the $P(E_{vib})$ for dissociation from each of the precursor conformers. The model has allowed us to divide the $P(E_T)$ of Figure 2.2 into three components. The red dashed line peaking near 25 kcal/mol represents the portion of the $P(E_T)$ leading to CH_2CH_2ONO radicals with E_{vib} above the dissociation barrier to NO + oxirane. The blue dashed line peaking near 30 kcal/mol is the portion leading to radicals with E_{vib} below the barrier to NO + oxirane but above the lowest-energy barrier to NO_2 + ethene. The bimodal black dashed line is the portion leading to radicals with E_{vib} below the lowest-energy barrier to NO_2 + ethene; these latter radicals are stable to all secondary dissociations, so they can enter the ionizer and be dissociatively ionized. Dissociative ionization of stable CH_2CH_2ONO is observed as NO^+ at m/e=30, discussed in Section 2.3.2.3. Secondary unimolecular dissociation of the radicals formed with higher vibrational energies is discussed in Section 2.3.3.

2.3.2.2. Primary photoelimination leading to HNO + $BrCH_2CHO$

Figure 2.4 shows the time-of-flight (TOF) data for m/e=31, representing fragments that ionize to HNO^+, taken with a synchrotron energy of 12.07 eV. We have fitted the data by a sum of two contributions: primary photodissociation of $BrCH_2CH_2ONO$ to HNO + $BrCH_2CHO$ (2-bromoacetaldehyde), with the HNO photoproduct signal fit in a green line with a peak near 40 μs, and secondary dissociation of CH_2CH_2ONO radicals to HNO + CH_2CHO (vinoxy), with the fit to the HNO products shown in dashed red line with a peak near 30 μs. The latter channel is discussed in Section 2.3.3.3. The sum of the two gives the total fit, shown as a black line. (The rising signal at long times, which is not from photofragments, is discussed in Section 2.3.1.) Figure 2.5 shows the recoil kinetic energy distribution, $P(E_T)$, for the

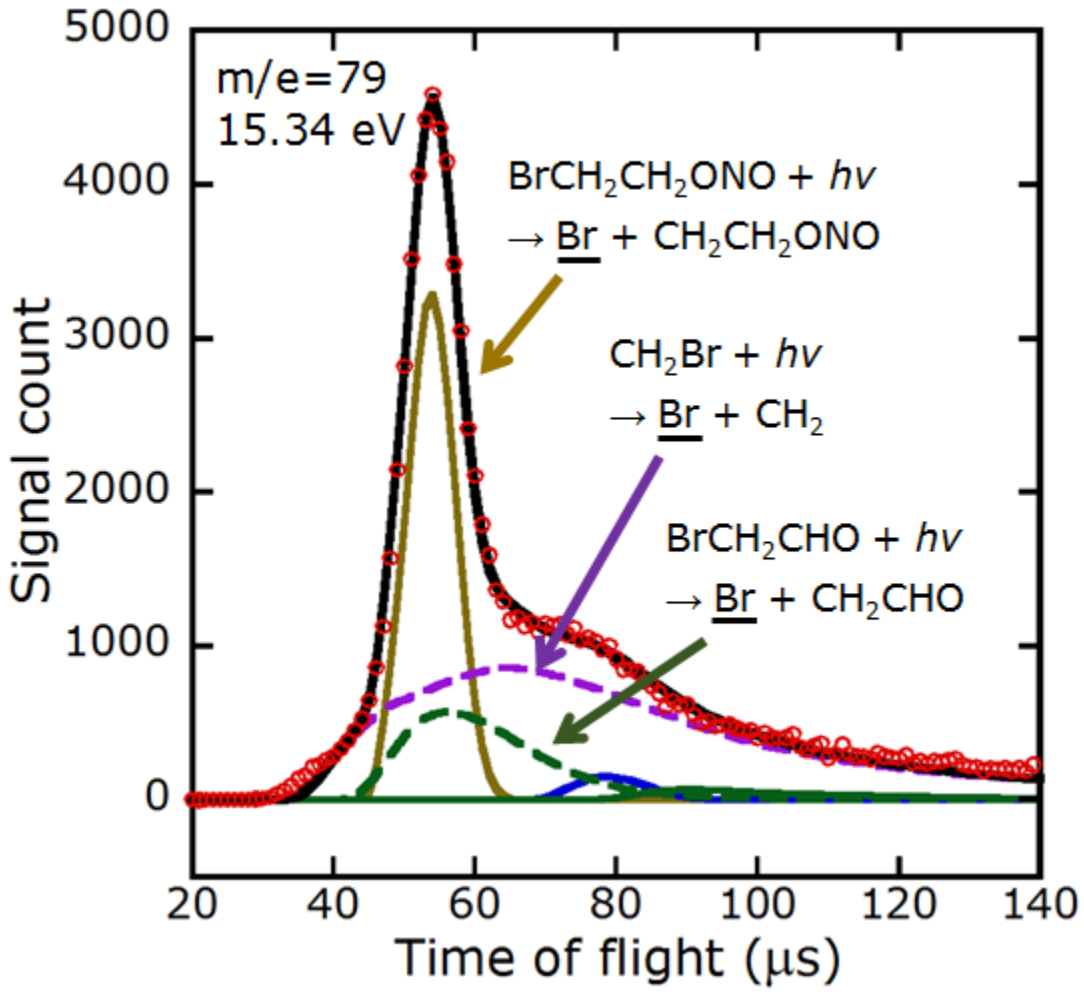

Figure 2.1. Time-of-flight spectrum of the signal at m/e = 79 (Br^+) with a photon energy of 15.34 eV. The sharp signal arises from primary photodissociation of $BrCH_2CH_2ONO$ to Br + CH_2CH_2ONO, fit by a solid brown line peaking around 55 μs. The other two labeled contributions are: photodissociation of the CH_2Br product of secondary dissociation of $BrCH_2CH_2O$ (dashed purple line, Section 2.3.5.2); and photodissociation of the $BrCH_2CHO$ formed by photoelimination of HNO from $BrCH_2CH_2ONO$ (dashed green line, Section 2.3.4.1). The two minor, unlabeled contributions are dissociative ionization of $BrCH_2CHO$ from secondary dissociation of $BrCH_2CH_2O$ (solid blue line peaking near 80 μs, Section 2.3.5.3) and from photoelimination of HNO from $BrCH_2CH_2ONO$ (solid green line with a maximum near 90 μs, Section 2.3.2.2).

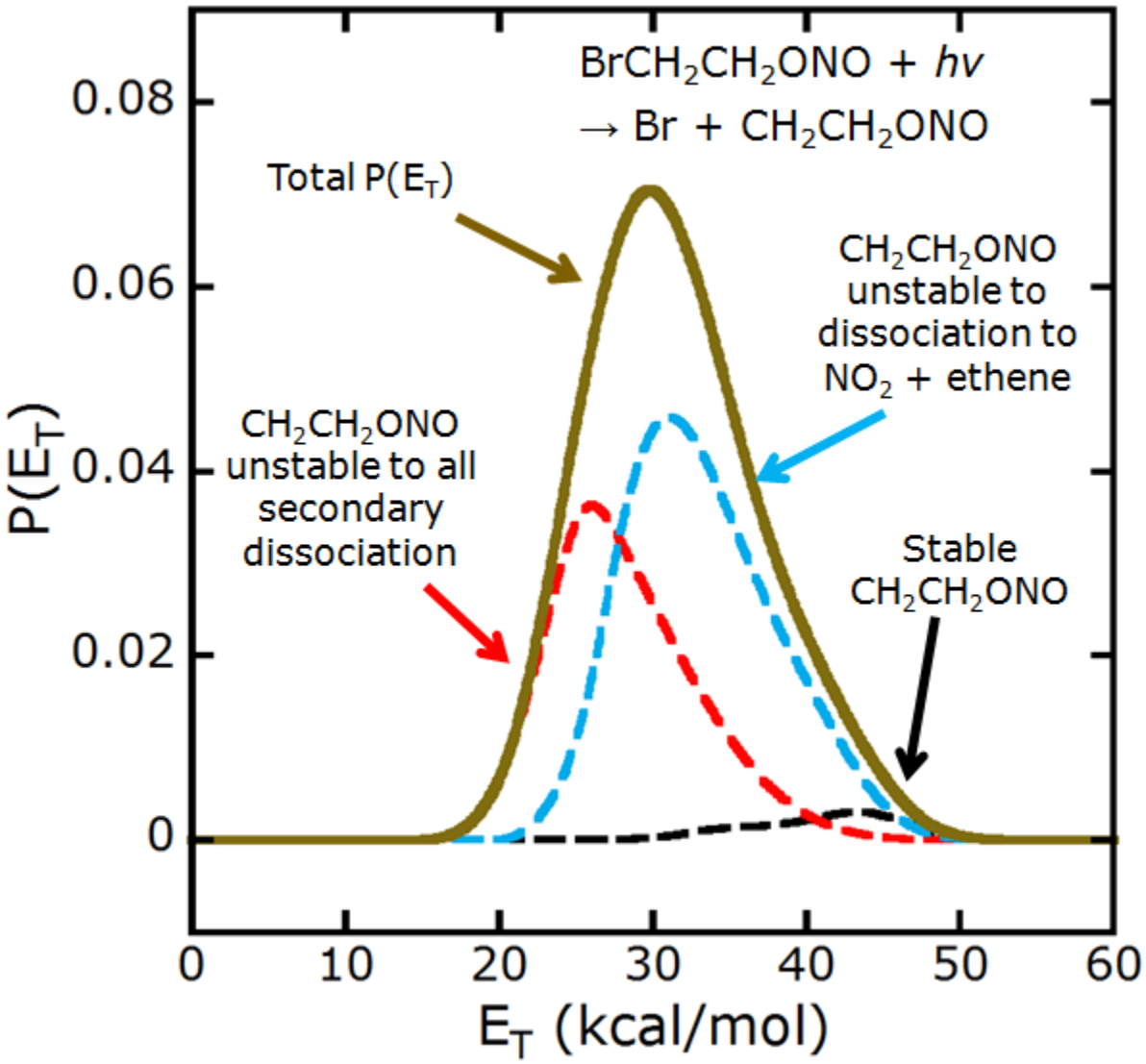

Figure 2.2. Photofragment recoil kinetic energy distribution, $P(E_T)$, of the Br and CH_2CH_2ONO co-fragments resulting from C-Br bond photofission in $BrCH_2CH_2ONO$. The total $P(E_T)$ (solid brown line), peaking near 30 kcal/mol, is derived by forward convolution fitting of the signal at m/e=79 (Br^+), shown in Figure 2.1; the total $P(E_T)$ gives the fit of the solid brown line in that figure. The total $P(E_T)$ is partitioned into three components, corresponding to the amount of vibrational energy that the CH_2CH_2ONO fragment is expected to acquire at each E_T. See the text for details.

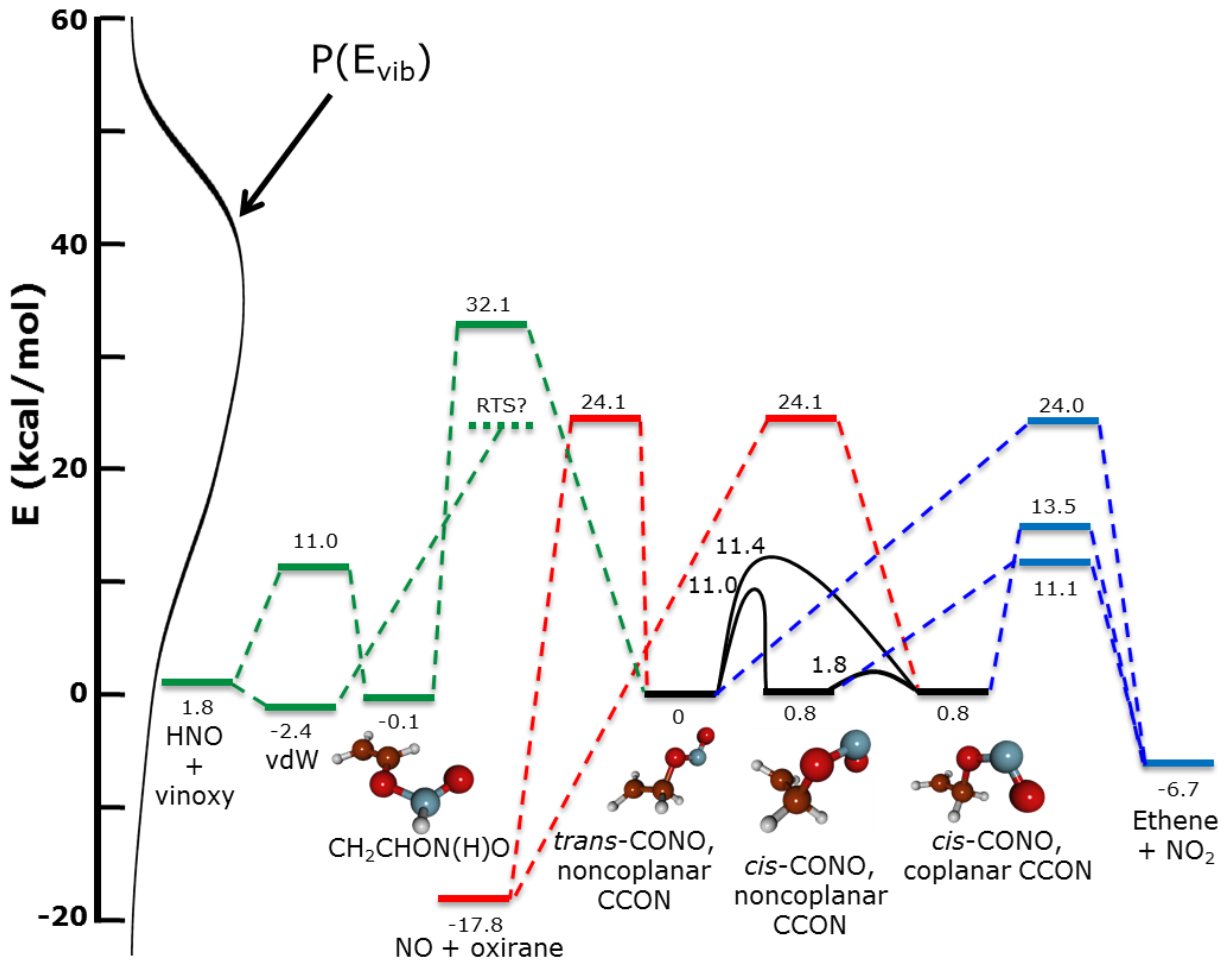

Figure 2.3. Stationary points along the potential energy surface of CH_2CH_2ONO, calculated using the G4//B3LYP/6-311++G(3df,2p) method. Energies are zero-point corrected and are given relative to the *trans* conformer. We have not found a transition state leading to the HNO + vinoxy van der Waals well, but estimate that the energetic barrier (labeled RTS?) to this roaming or non-IRC channel is best approximated by the barrier to NO + oxirane. The calculation of the vibrational energy distribution of the *trans* conformer of the radical, $P(E_{vib})$, is described in the text.

$BrCH_2CH_2ONO \rightarrow HNO + BrCH_2CHO$ photofragmentation channel, derived by fitting the contribution to the signal shown in green line to Figure 2.4. The $P(E_T)$ is broad, with a maximum at approximately 20 kcal/mol. The velocity distribution of the momentum-matched $BrCH_2CHO$ co-fragment is also accurately fitted by this $P(E_T)$, manifesting as dissociative ionization of $BrCH_2CHO$ to CH_3^+ (data in Section 2.3.4.2) and CHO^+ (data in Appendix A); thus the derived $P(E_T)$ is verified.

This photodissociation produces HNO and $BrCH_2CHO$ with a large amount of internal energy, which can lead to secondary dissociation. Using the $P(E_T)$ of Figure 2.5 and $\Delta H_{0K} = 10.3$ kcal/mol (implicitly assuming that the dissociation correlates adiabatically to the ground electronic states of the two products), conservation of energy (see eq. 7) requires that the sum of the internal energies of the two fragments, $E_{int}(HNO) + E_{int}(BrCH_2CHO)$, lie in a range from 107 to 140 kcal/mol. The dissociation limit for HNO is 47.0 kcal/mol,[43] leading to the products H + NO with no barrier above the endoergicity.[44] We estimate the dissociation limit of $BrCH_2CHO$ to be no less than the endoergicity of transformation to $Br + CH_2CHO$, $\Delta H_{0K} = 60.3$ kcal/mol. (The transformation to $CH_2Br + CHO$ has a greater endoergicity, 78.5 kcal/mol; the transformation to HBr + ketene (H_2CCO) has a transition state 62 kcal/mol above $BrCH_2CHO$.) Any photodissociation event imparting greater than 47.0 + 60.3 = 107.3 kcal/mol of *vibrational* energy to the HNO and $BrCH_2CHO$ fragments must therefore lead to secondary dissociation of at least one of them. Lesser amounts of vibrational energy can also lead to secondary dissociation if the energy is, by chance, partitioned mainly into one fragment. Although the available E_{int} is always greater than 107 kcal/mol, an unknown fraction of the total is partitioned into rotational energy, which (to first order) cannot contribute to dissociation. We are unable to assess the amount of partitioning to rotational energy. Because there must be nonzero rotational energy,

however, we conclude that not every primary photodissociation to HNO + $BrCH_2CHO$ must lead to secondary dissociation, but secondary dissociation of one fragment is energetically allowed if E_{rot} is low.

2.3.2.3. Primary photodissociation leading to NO + $BrCH_2CH_2O$

Photolysis to NO + alkoxy is a standard product channel for alkyl nitrites. The NO + $BrCH_2CH_2O$ channel in this molecule was previously observed in studies at 193 nm and at 351/355 nm. We characterize this channel using data collected at m/e=30 (NO^+, H_2CO^+) at several synchrotron energies below and above the 10.89 eV[45,46] ionization threshold of H_2CO, another major product of mass 30. Figure 2.6 shows TOF spectra and our forward convolution fits using 9.845 eV and 11.06 eV photoionization; in Appendix A we include the data and fits at 10.5 eV, 10.84 eV, and 11.27 eV. (The rising signal at long times, which is not from photofragments, is discussed in Section 3.1.) The contribution of primary NO photofragments is a sharp signal represented by the solid blue line peaking near 30 μs. Given in Figure 2.7 is the $P(E_T)$ of this dissociation, indicating that the kinetic energy release extends from approximately 20 kcal/mol to approximately 45 kcal/mol, peaking near 33 kcal/mol. This is essentially identical to the $P(E_T)$ of the previous study at 193 nm, differing from it by approximately 3 kcal/mol in the peak position and in the length of the tail of the distribution at higher energies.

Other contributions to the data in Figure 2.6 are: a strong, broad signal of H_2CO formed by secondary dissociation of $BrCH_2CH_2O$ (dashed red line with a maximum near 40 μs, only at 11.09 eV, Section 2.3.5.1); primary HNO undergoing secondary dissociation to H + NO (solid green line, Appendix A); the NO product of secondary dissociation of CH_2CH_2ONO to NO + oxirane (dashed black curve, Section 2.3.3.2); an NO product formed by photodissociation of

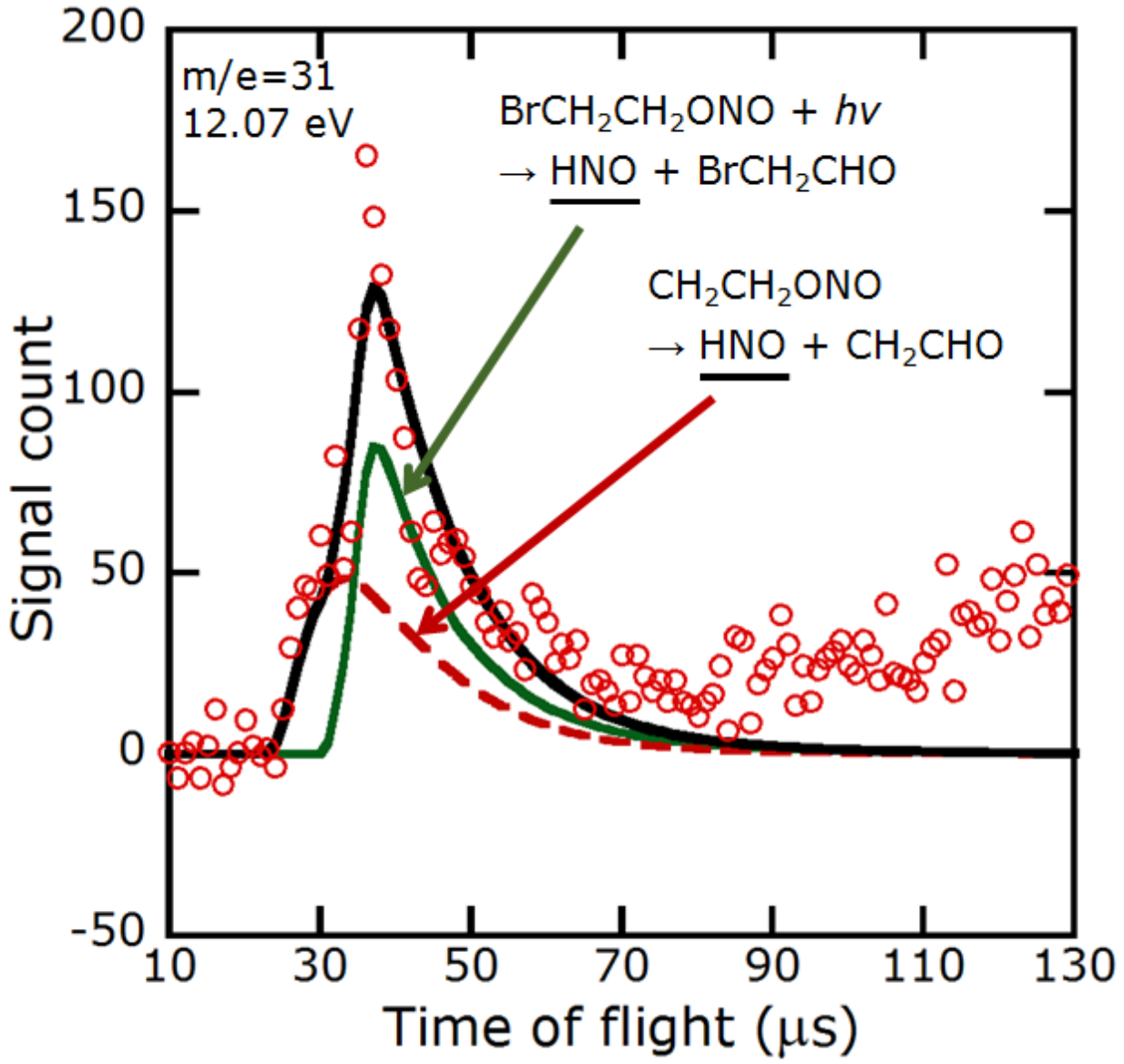

Figure 2.4. Time-of-flight spectrum of the signal at m/e = 31 (HNO^+) with a synchrotron energy of 12.07 eV. Primary photodissociation of $BrCH_2CH_2ONO$ to $BrCH_2CHO$ + HNO is fit by the solid green line, peaking near 40 μs. Secondary dissociation of CH_2CH_2ONO radicals to CH_2CHO (vinoxy) + HNO is fit by the dashed red line, peaking near 30 μs.

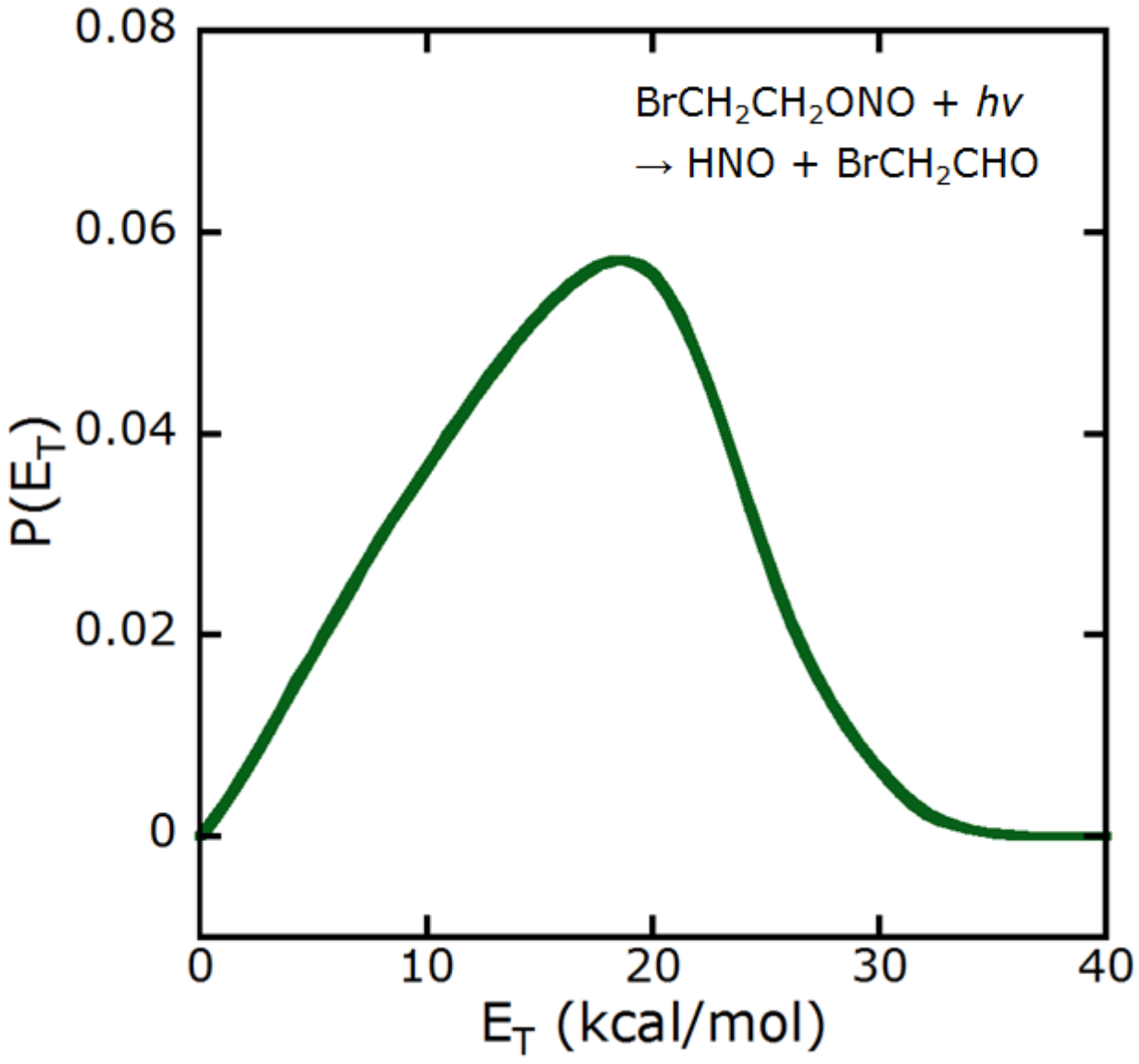

Figure 2.5. Photofragment recoil kinetic energy distribution, $P(E_T)$, of the HNO and $BrCH_2CHO$ fragments resulting from photoelimination of HNO from $BrCH_2CH_2ONO$ at 193 nm. The $P(E_T)$ is derived by forward convolution fitting of the signal at m/e = 31 (HNO^+).

NO_2, a secondary product of CH_2CH_2ONO radicals (dashed purple line, Section 2.3.3.1); and dissociative ionization of CH_2CH_2ONO radicals that are stable to secondary dissociation (bimodal solid brown line near 47 μs, discussed presently). No other fragment has a sharply-peaked neutral flight time near 47 μs, so we deduce that the sharply-peaked signal in that region must be from dissociative ionization of stable CH_2CH_2ONO.

The TOF distribution of the CH_2CH_2ONO channel is derived using the portion of the C-Br photofission $P(E_T)$ that is predicted, by our angular momentum model, to produce CH_2CH_2ONO radicals with less vibrational energy than the dissociation threshold. In Figure 2.2, this portion is represented by a black dashed line. The fit is remarkably good, given the assumptions of Section 2.3.2.1. There is some signal at slightly longer flight times than the fitted peak, near 53 μs, which is not accounted for by the model; this signal is easily explained by supposing that some of the primary Br is likely produced as spin-orbit excited $Br(^2P_{1/2})$, and any stable CH_2CH_2ONO co-fragments to these Br would, by conservation of energy, have lower E_T and longer flight times.

The internal energy of the $BrCH_2CH_2O$ co-fragment to primary NO photoproduct depends in part, by conservation of energy, on the rotational and vibrational energy of the departing NO fragment. Wang et al. gave a thorough assessment of these energetic sinks in the previous report, concluding that the average $E_{int}(NO)$ is likely on the order of 30.0 kcal/mol. Given this value, the $P(E_T)$ of Figure 2.7, and $\Delta H_{0K} = 39.0$, we find that the E_{int} of $BrCH_2CH_2O$ fragments fall in a range from approximately 30 kcal/mol to approximately 55 kcal/mol. These radicals therefore certainly can access the dissociation channels leading to $CH_2Br + H_2CO$ and to H loss (as in the previous study), but higher-barrier products such as HBr + vinoxy, Br + oxirane, and Br + acetaldehyde are far less favorable. In Appendix A we discuss evidence of a very small

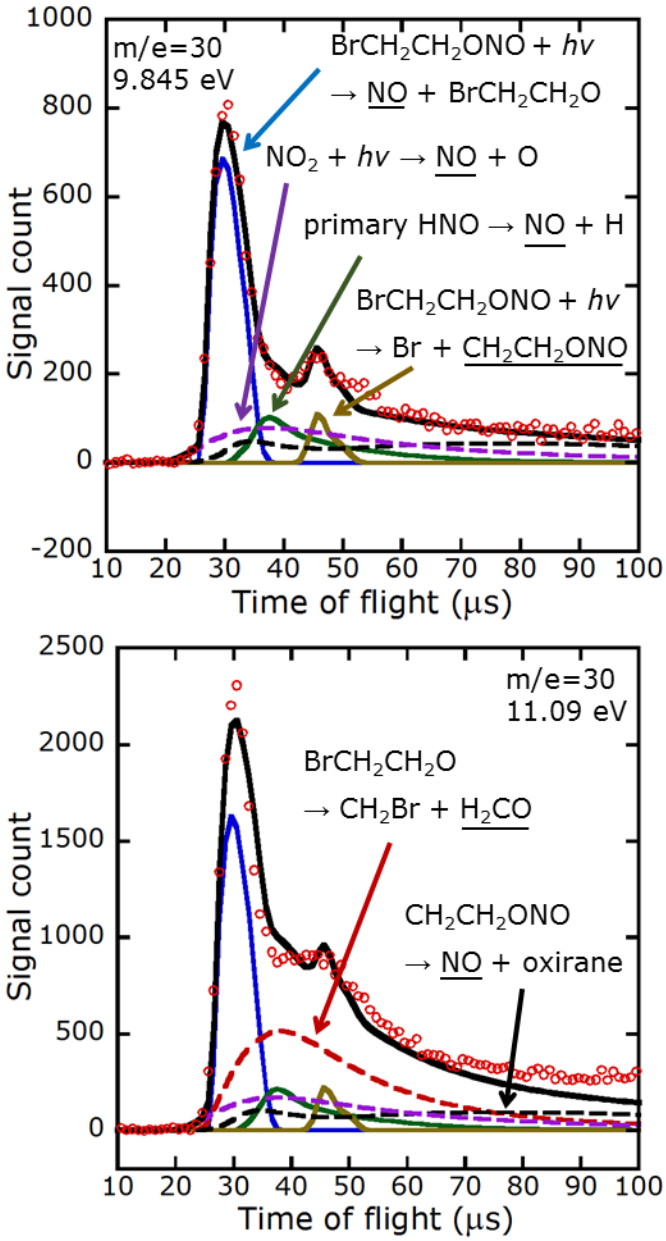

Figure 2.6. Time-of-flight spectrum of the signal at m/e=30 (NO^+, H_2CO^+) at photoionization energies of 9.845 eV (upper frame) and 11.09 eV (lower frame). The sharply peaked signal near 30 μs is from primary O-NO bond photofission in $BrCH_2CH_2ONO$, and is fitted by the solid blue line. Data and fits at other energies are provided in Appendix A. Contributions to the signal are: the H_2CO product of $BrCH_2CH_2O$ (red dashed line, Section 2.3.5.1, visible only at high photon energy); secondary dissociation of HNO formed by photoelimination from $BrCH_2CH_2ONO$ (solid green line peaking near 40 μs, Appendix A); dissociative ionization of CH_2CH_2ONO radicals that are stable to secondary dissociation (solid brown line peaking near 45 μs, Section 2.3.2.1); the NO product of CH_2CH_2ONO (black dashed line, Section 2.3.3.2); and photodissociation of NO_2 formed with high internal energy from CH_2CH_2ONO (purple dashed line, Section 2.3.3.1).

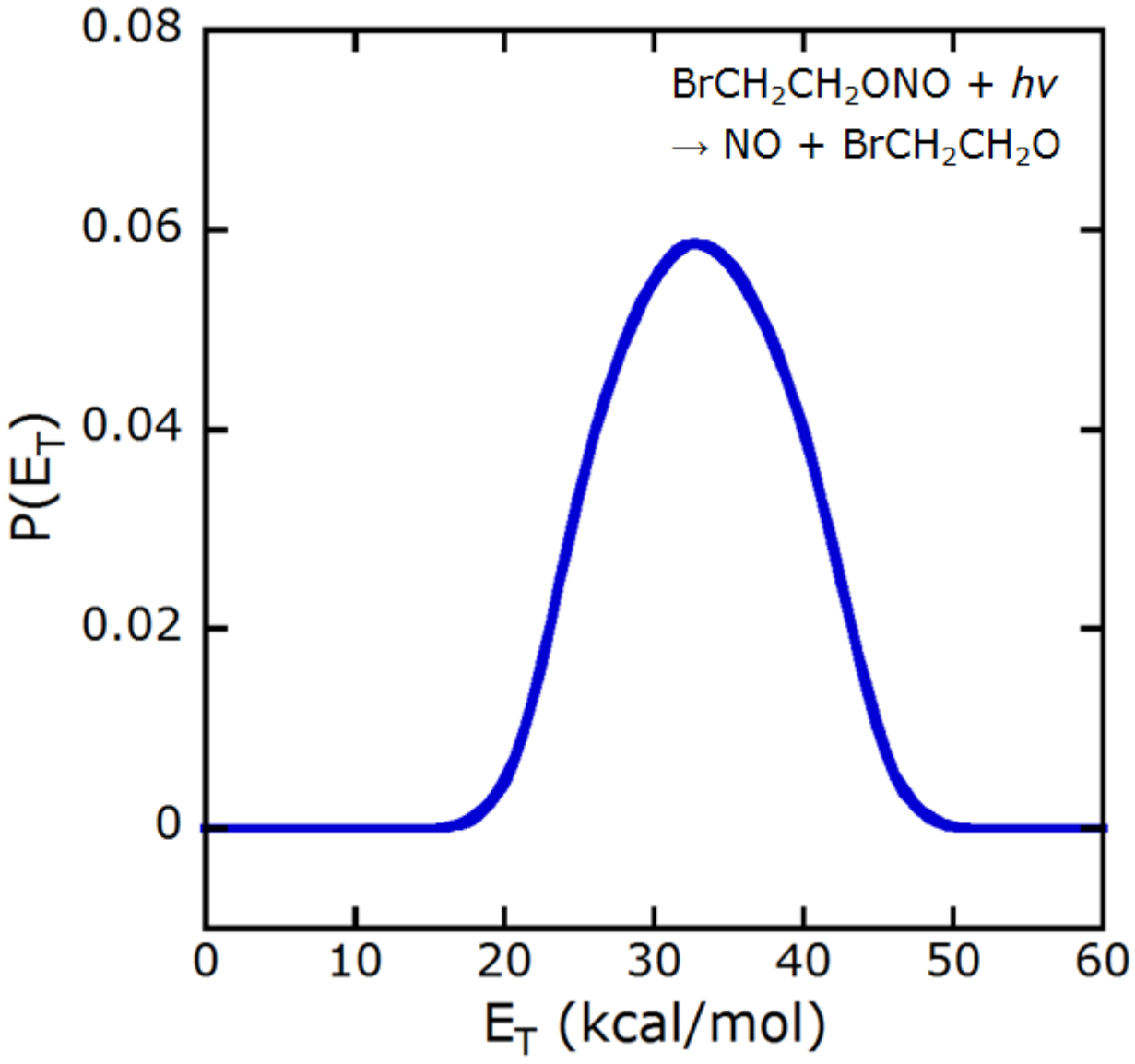

Figure 2.7. Photofragment recoil kinetic energy distribution, $P(E_T)$, of the NO + $BrCH_2CH_2O$ resulting from primary photodissociation. The $P(E_T)$, peaking near 35 kcal/mol, is derived by forward convolution fitting of the signal near 35 μs in the data at m/e=30 shown in Figure 2.6. The TOF distribution predicted by this $P(E_T)$ is shown as the solid blue line in that figure.

branching to HBr + vinoxy from $BrCH_2CH_2O$.

2.3.3. Secondary dissociation of CH_2CH_2ONO radicals

2.3.3.1. The NO_2 + ethene channel

Secondary dissociation of CH_2CH_2ONO radicals to NO_2 + ethene is characterized by data collected at m/e=28 ($CH_2CH_2^+$) and m/e=46 (NO_2^+), both with a synchrotron energy of 10.84 eV. The TOF data for both masses are shown in Figure 2.8. The data are fitted solely by this channel (solid black line), with no other contributions, because in this system NO_2 and ethene are formed exclusively as co-fragments. (Our data show no evidence of dissociative ionization of stable CH_2CH_2ONO radicals to either ion.) In fitting the data, we have used only the portion of the primary C-Br photofission $P(E_T)$ leading to unstable radicals, i.e., the sum of the red-dashed and blue-dashed contributions in Figure 2.2.

The data evince an asymmetric $I(\theta)$: there is backward-scattering of the NO_2 fragments and forward-scattering of the ethene fragments. To obtain a first approximation to the true $I(\theta)$, we employed the angular momentum model of Brynteson and Butler,[42] which predicts the speed and angular distributions of fragments of a dissociating species (here, CH_2CH_2ONO) based on a calculation of its time-dependent angular velocity. The complete results of the model are provided in Appendix A; in sum, dissociation of CH_2CH_2ONO was predicted to strongly favor forward-scattering of ethene. Using this prediction as a template, we fitted the data at m/e=28 by iteratively adjusting both the $I(\theta)$ and the $P(E_T)$ for this dissociation. The derived $P(E_T)$ and $I(\theta)$ are shown in Figure 2.9, with the $P(E_T)$ plotted as a solid black line. The fit to the data is shown in the top frame of Figure 2.8.

The NO_2^+ data are not well-fitted by the total $P(E_T)$ of Figure 2.9. However, a good fit is

obtained by slightly decreasing the $P(E_T)$ at low values of E_T. The adjusted $P(E_T)$ is plotted as the dashed black line in the lower frame of Figure 2.9; it differs from the total $P(E_T)$ only for $E_T < 14$ kcal/mol. The fit to the data at m/e=46 given by this adjusted $P(E_T)$ is shown in the lower frame of Figure 2.8. The necessity of this "adjustment" indicates that some of the NO_2 fragments formed with low kinetic energy cannot be detected as NO_2^+, but rather are lost to another process. Booth et al.[50] and Butler et al.[51] observed that NO_2 fragments formed with high internal energy can photodissociate at 193 nm to form NO + O; the $P(E_T)$ for this photodissociation was determined in ref. 51. We infer that the same process occurs here: some NO_2 fragments formed with low kinetic energy have sufficient internal energy to undergo photodissociation, and thus cannot be detected as NO_2^+. The NO product of this photodissociation is observed as NO^+ in the fits at m/e=30 of Figure 2.6. The contribution due to this channel is represented by the dashed purple line in that figure. Its TOF distribution was determined by forward convolution using, for primary photodissociation, the portion of the C-Br photofission $P(E_T)$ leading to unstable CH_2CH_2ONO radicals; for secondary dissociation, the $I(\theta)$ of Figure 2.9 and the portion of the $P(E_T)$ of that figure leading to unstable NO_2, i.e., the difference between the solid line and the dashed line; and for this photodissociation, an isotropic $I(\theta)$ and the $P(E_T)$ of Butler et al. (reproduced from ref. 51 in Appendix A). The fit to the data at m/e=30 is quite satisfactory.

2.3.3.2. The NO + oxirane channel

Those CH_2CH_2ONO radicals with the highest vibrational energies can surmount a barrier of 24.1 kcal/mol from the *trans* conformer or 23.3 kcal/mol from the coplanar *cis* conformer to dissociate to NO + oxirane. Data taken at m/e=44 (oxirane cation) with a synchrotron energy of 10.84 eV are plotted in Figure 2.10, with the fit in black line. This channel is the only contributor

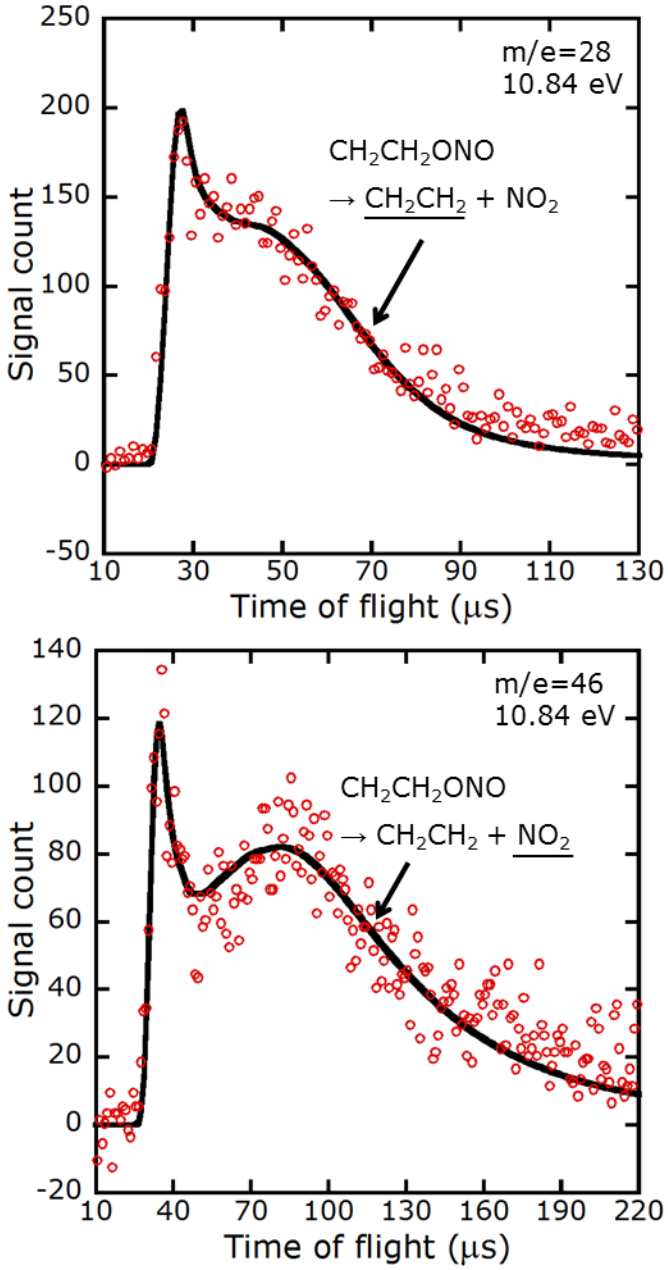

Figure 2.8. Time-of-flight spectra and forward convolution fits of m/e = 28 ($CH_2CH_2^+$, top frame) and m/e = 46 (NO_2^+, bottom frame) at a photoionization energy of 10.84 eV. These two species are formed exclusively as co-fragments from secondary dissociation of CH_2CH_2ONO. The fitting of this channel is explained in the text.

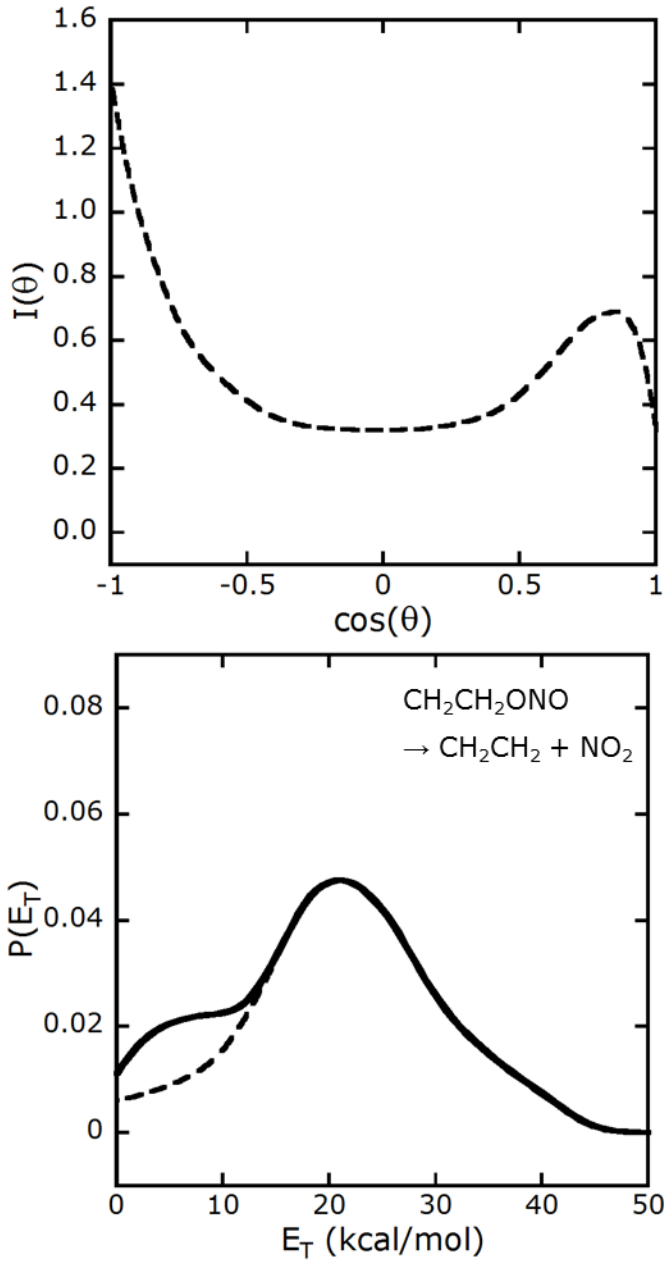

Figure 2.9. Angular distribution, I(θ), and product recoil kinetic energy distribution, $P(E_T)$, for the dissociation of CH_2CH_2ONO radicals to NO_2 + ethene. Shown here is the I(θ) for NO_2, which is backward-scattered; the angular distribution for its co-fragment, ethene, is the mirror image of this distribution, where the mirror plane is θ = 0°. The total $P(E_T)$, shown in solid black line, gives the fit to the data at m/e=28 of Figure 2.8; the altered $P(E_T)$, shown in dashed black line but coinciding with the solid line above 14 kcal/mol, gives the fit to the data at m/e=46 of Figure 2.8. The fitting of this channel is explained in the text.

of fragments of m/e=44. The $P(E_T)$ and $I(\theta)$ derived by fitting the data are shown in Figure 2.11. The dissociation to NO + oxirane evinces a similar $I(\theta)$ to that of dissociation to NO_2 + ethene, with strongly forward-scattered oxirane. The fit to oxirane is verified by the fit at its dissociative ionization product, CH_3^+. The TOF distribution of oxirane fragments is shown as a black dashed line in the fit for m/e=15 (CH_3^+) in Section 2.3.4.2; the predicted oxirane TOF distribution is found to agree with the data. The NO co-fragment to this oxirane is detected as NO^+ in the m/e=30 data of Figure 2.6; this channel is the major contributor to the NO signal at long flight times (aside from the background signal discussed in Section 2.3.1).

2.3.3.3. The HNO + vinoxy channel

In this work we sought to determine whether the CH_2CH_2ONO radical undergoes unimolecular dissociation to form HNO + vinoxy. The transformation is endoergic by 1.8 kcal/mol, as plotted in Figure 2.3. Data in support of this channel appear at m/e=31 (HNO^+, Figure 2.4) and at m/e=43 (vinoxy cation, Figure 2.12). In both figures, our forward convolution fit for this HNO + vinoxy channel is represented by the dashed red line, which has a maximum near 30 μs for HNO and near 35 μs for vinoxy. We suppose that the barrier to this dissociation is not greater than the barrier to NO + oxirane (vide infra), so for these fits we use the portion of the primary C-Br photofission $P(E_T)$ leading to radicals with enough vibrational energy to surmount the barrier to NO + oxirane, i.e., the red curve of Figure 2.2. We also use the sideways-scattered secondary angular distribution of Figure 2.13. The $P(E_T)$ for this dissociation is shown in Figure 2.14.

Photodissociation of the precursor cannot lead to HNO + $BrCH_2CHO$ with enough kinetic energy to account for the HNO signal at short flight times, as the TOF distributions of

their $BrCH_2CHO$ cofragments would not fit the data at m/e=15 (Section 3.4.2). Therefore this HNO is from a secondary channel, and according to our analysis the only secondary channel that can lead to HNO from this precursor is the dissociation $CH_2CH_2ONO \longrightarrow HNO + vinoxy$. The fit at m/e=43 is consistent with this conclusion. Moreover, since vinoxy from this channel is (by conservation of energy) formed with a low E_{int}, it is stable to further dissociation, and can dissociatively ionize to CH_3^+. In the m/e=15 data of Section 2.3.4.2, the dashed red line with a maximum near 40 μs represents the contribution of dissociative ionization of this source of vinoxy.

2.3.4. Secondary dissociation following the HNO + $BrCH_2CHO$ primary channel

2.3.4.1. Photodissociation of $BrCH_2CHO$ to produce Br + vinoxy

Figure 2.12 shows TOF data and forward convolution fits at m/e=43 (vinoxy, CH_2CHO^+) taken with a synchrotron energy of 10.01 eV. We attribute most of the signal to photodissociation of nascent $BrCH_2CHO$ to Br + vinoxy. This is, then, a two-photon process: the $BrCH_2CH_2ONO$ precursor absorbs a 193 nm photon and dissociates to HNO + $BrCH_2CHO$ (Section 3.2.2), whereupon the latter absorbs a 193 nm photon and dissociates to Br + vinoxy, analogously to the photodissociation of $ClCH_2CHO$ at 193 nm to Cl + vinoxy.[48] (In Appendix A we explain why this signal should not be ascribed to a single-photon process.) The contribution from this source is represented by the green dashed line in Figure 2.12, and the photodissociation $P(E_T)$ derived by forward convolution fitting of this contribution is shown by the red dashed line in Figure 2.15. This fit requires an $I(\theta)$ peaking near 90°, plotted in Figure 2.13; that is, the Br and vinoxy fragments are scattered preferentially orthogonally to the velocity vector of the primary $BrCH_2CHO$ fragments. The fit is supported by the data at m/e=15 (CH_3^+, Section

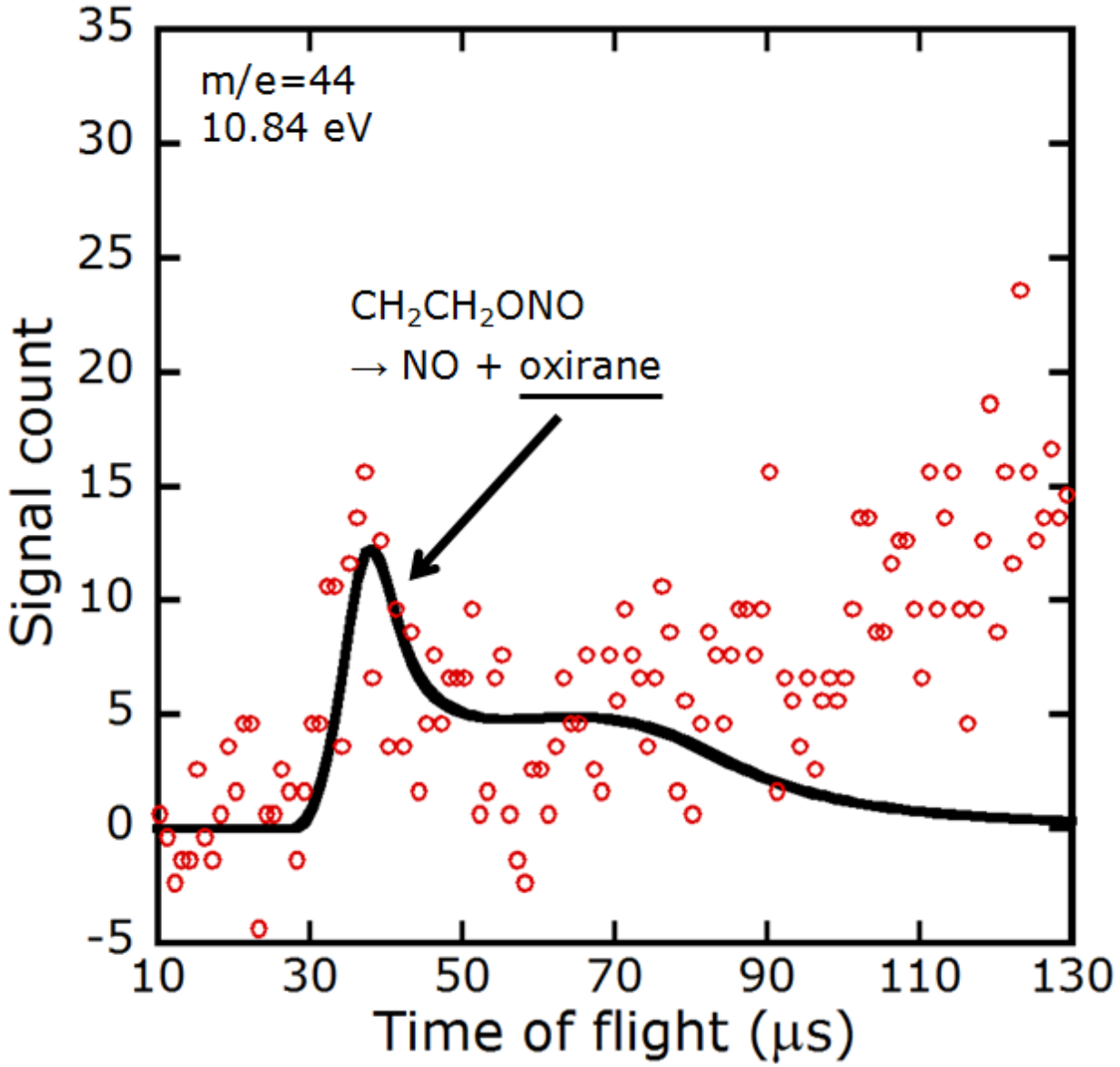

Figure 2.10. Time-of-flight spectrum and forward convolution fit of the signal at m/e=44 (oxirane cation) at a photoionization energy of 10.84 eV. Oxirane is formed exclusively from secondary dissociation of CH_2CH_2ONO.

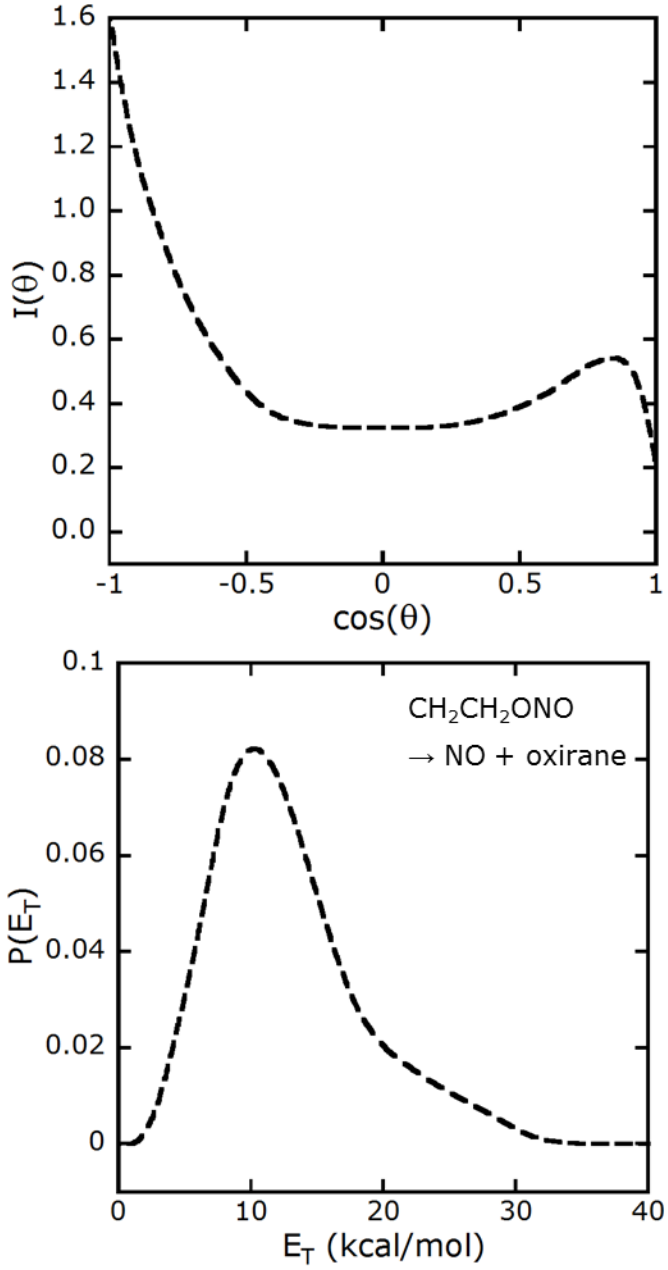

Figure 2.11. Angular distribution, I(θ), and product recoil kinetic energy distribution, $P(E_T)$, for the dissociation of CH_2CH_2ONO to NO + oxirane. Shown here is the I(θ) for the NO fragment, which is backward-scattered; the I(θ) for the oxirane is the mirror image of this distribution, where the mirror plane is θ = 0°. These distributions were derived by forward convolution fitting of the data at m/e=44 (oxirane cation) of Figure 2.10, and are supported by data at other masses as noted in the text.

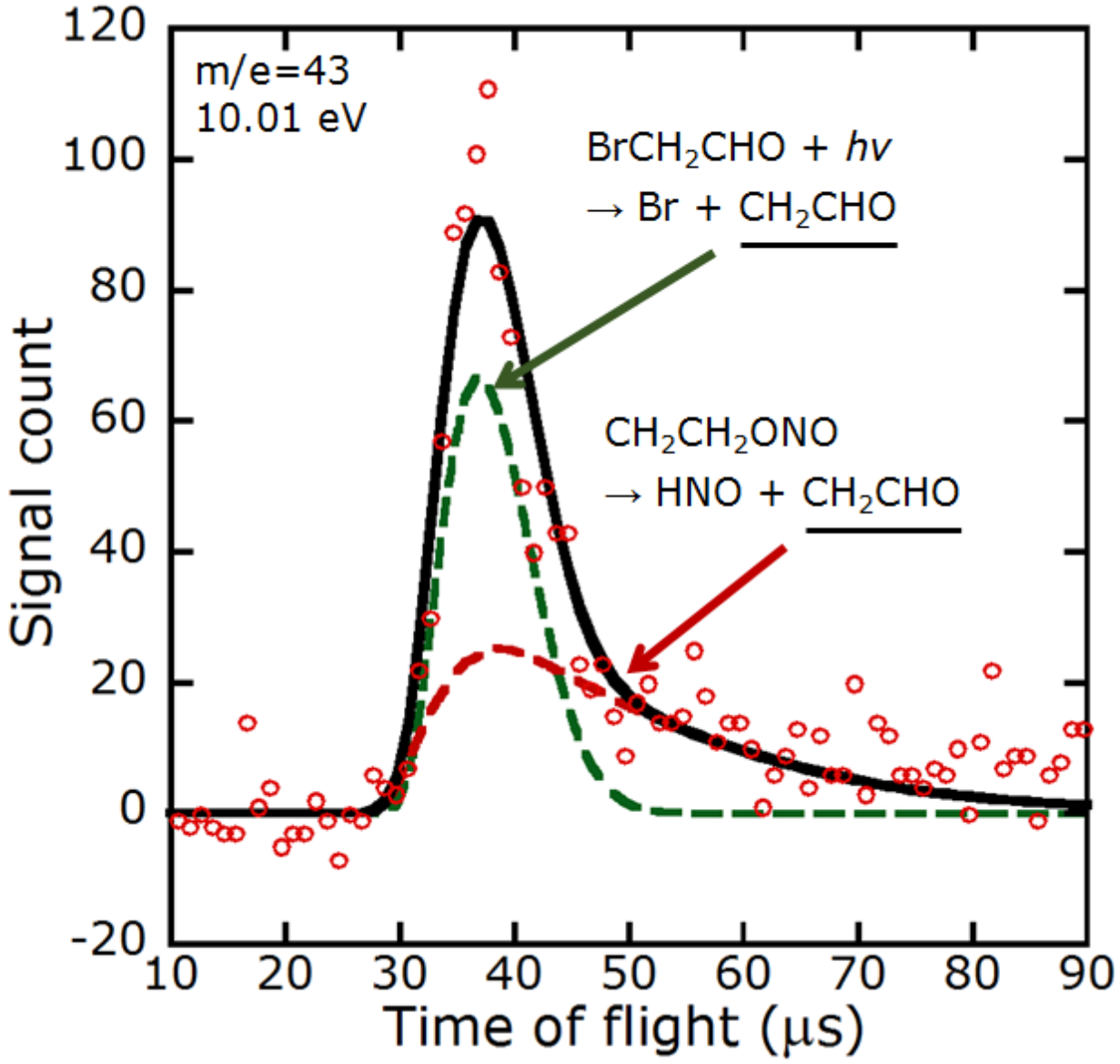

Figure 2.12. Time-of-flight spectrum of the signal at m/e=43 (vinoxy cation: CH_2CHO^+) at a photoionization energy of 10.01 eV. Two contributions are observed: photodissociation of the $BrCH_2CHO$ formed with primary photoelimination of HNO from $BrCH_2CH_2ONO$ (green dashed line, Section 2.3.4.1), and secondary dissociation of CH_2CH_2ONO to HNO + vinoxy (red dashed line, Section 2.3.3.3). This fit does not represent all photodissociation of $BrCH_2CHO$, as some of the vinoxy produced in that process is unstable to further dissociation, and cannot be observed as CH_2CHO^+. For details, see the text.

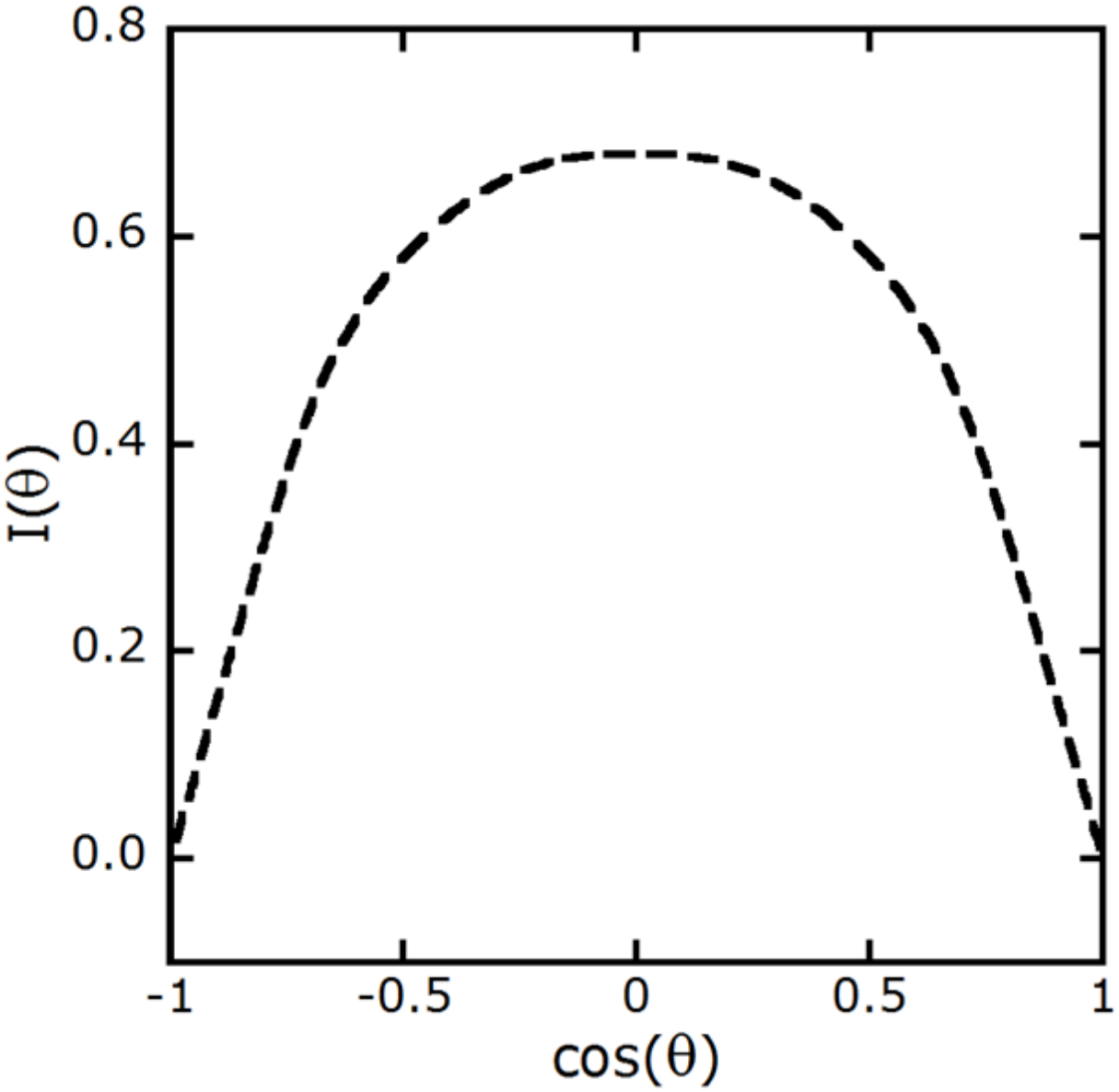

Figure 2.13. Angular distribution, I(θ), indicating "sideways-scattering": the secondary dissociation event preferentially scatters both fragments perpendicularly to the velocity vector of the dissociating fragment.

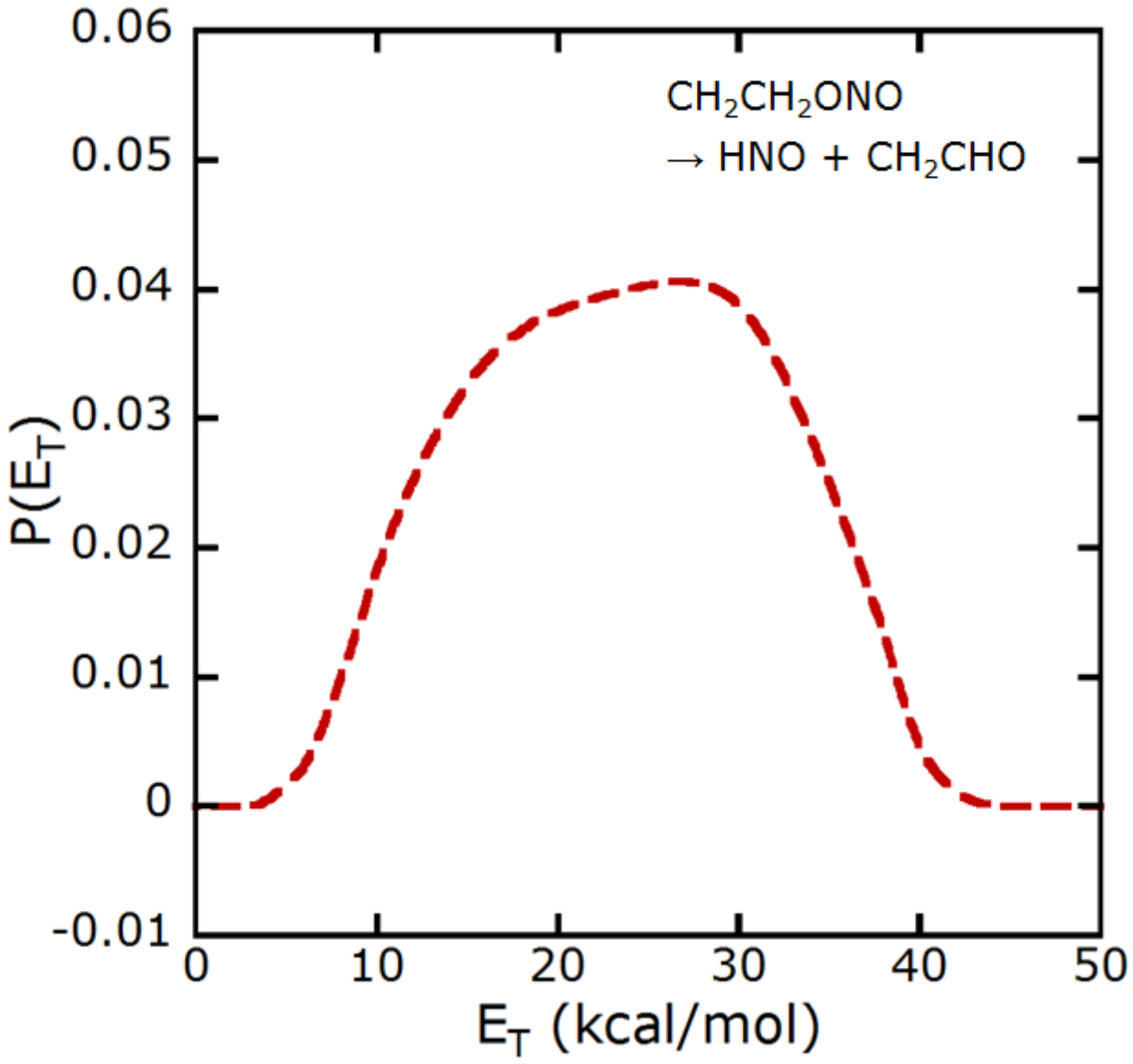

Figure 2.14. Recoil kinetic energy distribution, $P(E_T)$, for the secondary dissociation of CH_2CH_2ONO radicals to HNO + vinoxy. The dissociation follows the sideways-scattered angular distribution of Figure 2.13.

2.3.4.2). The other contribution to the data is secondary dissociation of CH_2CH_2ONO radicals to vinoxy + HNO (dashed red line, Section 2.3.3.3).

As in the 193 nm photodissociation of $ClCH_2CHO$, photodissociation events of $BrCH_2CHO$ having lower kinetic energy release are expected to produce vinoxy radicals with sufficient E_{vib} to dissociate to CH_3 + CO. Br + vinoxy produced with lower E_T are observed in the data at m/e=79 (Br^+) but not at m/e=43. The total $P(E_T)$ of Figure 2.15 thus includes a low-E_T contribution leading to vibrationally unstable vinoxy, plotted as a dashed blue line with a maximum near 22 kcal/mol, which was derived by forward convolution fitting to the Br^+ data of Figure 2.1. The fit to this channel in the Br^+ data is shown as a dashed green line and is predicted by the entire $BrCH_2CHO$ photodissociation $P(E_T)$ of Figure 2.15; whereas the highest E_Ts of this dissociation lead solely to stable vinoxy and are observed and fitted at m/e=43. (Interestingly, the total $P(E_T)$ resembles the one derived by Miller et al. in their study of the photodissociation of $ClCH_2CHO$ to Cl + vinoxy at 193 nm.[48])

2.3.4.2. Tertiary dissociation of vinoxy

The unstable vinoxy indicated in Section 3.4.1 is expected, based on a previous study of $ClCH_2CHO$,[48] to dissociate to CH_3 + CO. In Figure 2.16 we present data acquired at m/e=15 (CH_3^+) with a synchrotron energy of 15.12 eV, with which we characterize this channel. The kinetic energy release of this dissociation is not conclusively known, though in ref. 48 it was found to be quite small. Our fit for this channel is shown as the dashed brown curve with a maximum near 40 μs in Figure 2.16; for the kinetic energy release of this channel we used a roughly half-normal distribution of standard deviation 5 kcal/mol, modified slightly to include a greater contribution of low E_T. The $P(E_T)$ is shown in Figure 2.17. The TOF distribution of this

channel was determined by forward convolution up to this "tertiary" dissociation, using: for primary photodissociation, the HNO photoelimination $P(E_T)$ of Figure 2.5, which produces $BrCH_2CHO$; for the secondary photodissociation, the low-kinetic energy portion of the $BrCH_2CHO$ photodissociation $P(E_T)$ of Figure 2.15 (plotted as a blue dashed line in that figure), which leads to vibrationally unstable vinoxy, with the sideways-scattered $I(\theta)$ of Figure 2.13; and, for the "tertiary" dissociation of vinoxy, an isotropic $I(\theta)$ and the $P(E_T)$ of Figure 2.17. The fit to the fast edge of the m/e=15 data is overall quite satisfactory.

2.3.4.3. Secondary dissociation of HNO and minor dissociation pathways of $BrCH_2CHO$

We observed a small signal at m/e=82 ($H^{81}Br^+$), which we attribute to photoelimination of HBr from $BrCH_2CHO$. We also observed some signal at m/e=29 (HCO^+) arising largely from dissociative ionization of $BrCH_2CHO$, H_2CO, and oxirane, and possibly also including photodissociation of $BrCH_2CHO$ to $CH_2Br + HCO$. Moreover, some of the HNO produced in the primary photodissociation of $BrCH_2CH_2ONO$ has sufficient vibrational energy to dissociate to H + NO, detected as m/e=30 (NO^+, Figure 2.6). We include these data and some analysis of these product channels in Appendix A.

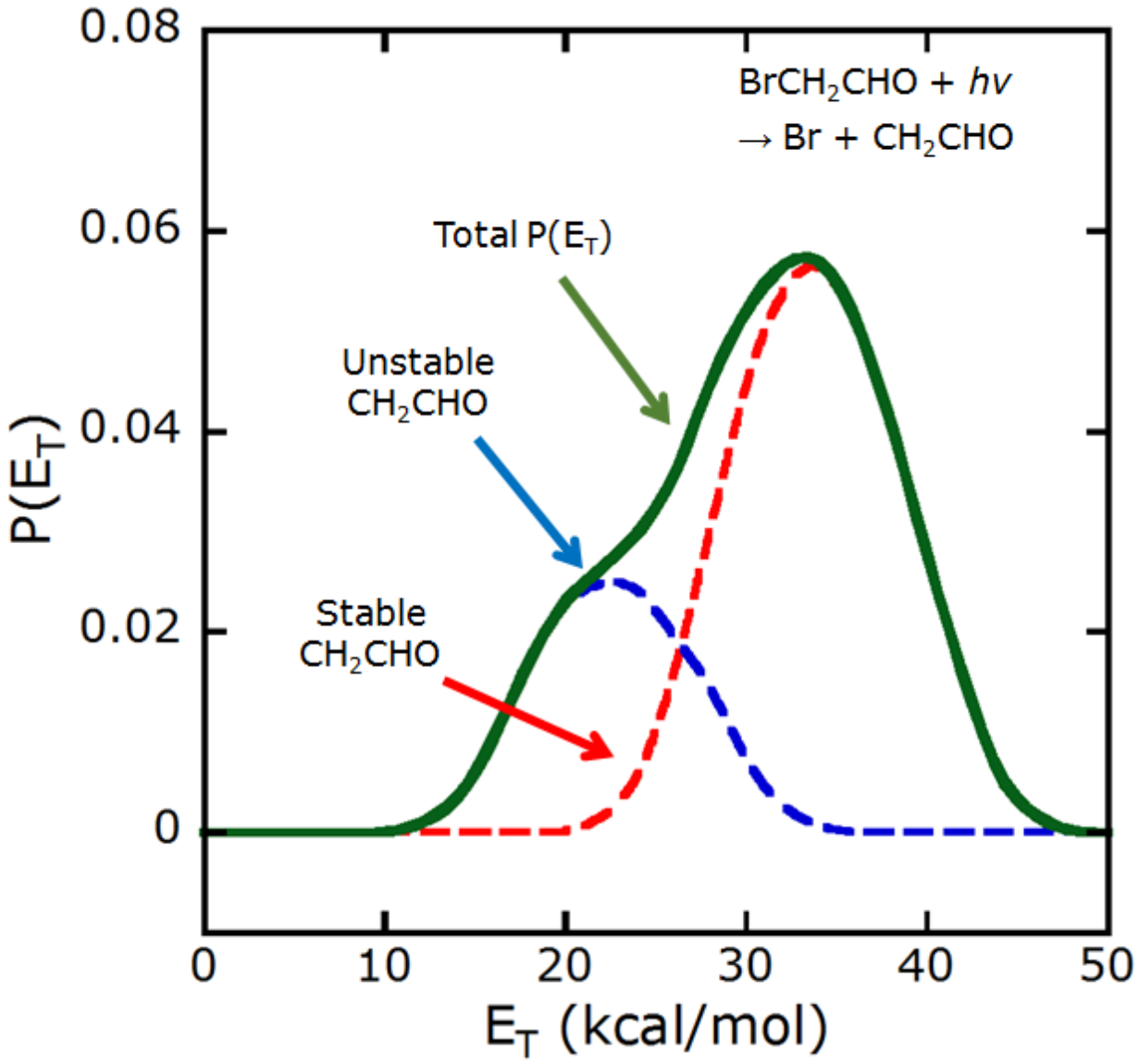

Figure 2.15. Recoil kinetic energy distribution, $P(E_T)$, for the photodissociation of $BrCH_2CHO$ to Br + vinoxy (CH_2CHO). The dashed red line is obtained by fitting the data at m/e=43 (vinoxy cation, dashed green line in Figure 2.12) and only represents kinetic energy release leading to vinoxy that is stable to subsequent dissociation. The total $P(E_T)$, shown in solid green line, is obtained by fitting the data at m/e=79 (Br^+, dashed green line in Figure 2.1). The blue dashed line represents kinetic energy release leading to vinoxy that undergoes subsequent dissociation to CH_3 + CO, and is obtained by subtracting the red-dashed distribution from the solid-green distribution.

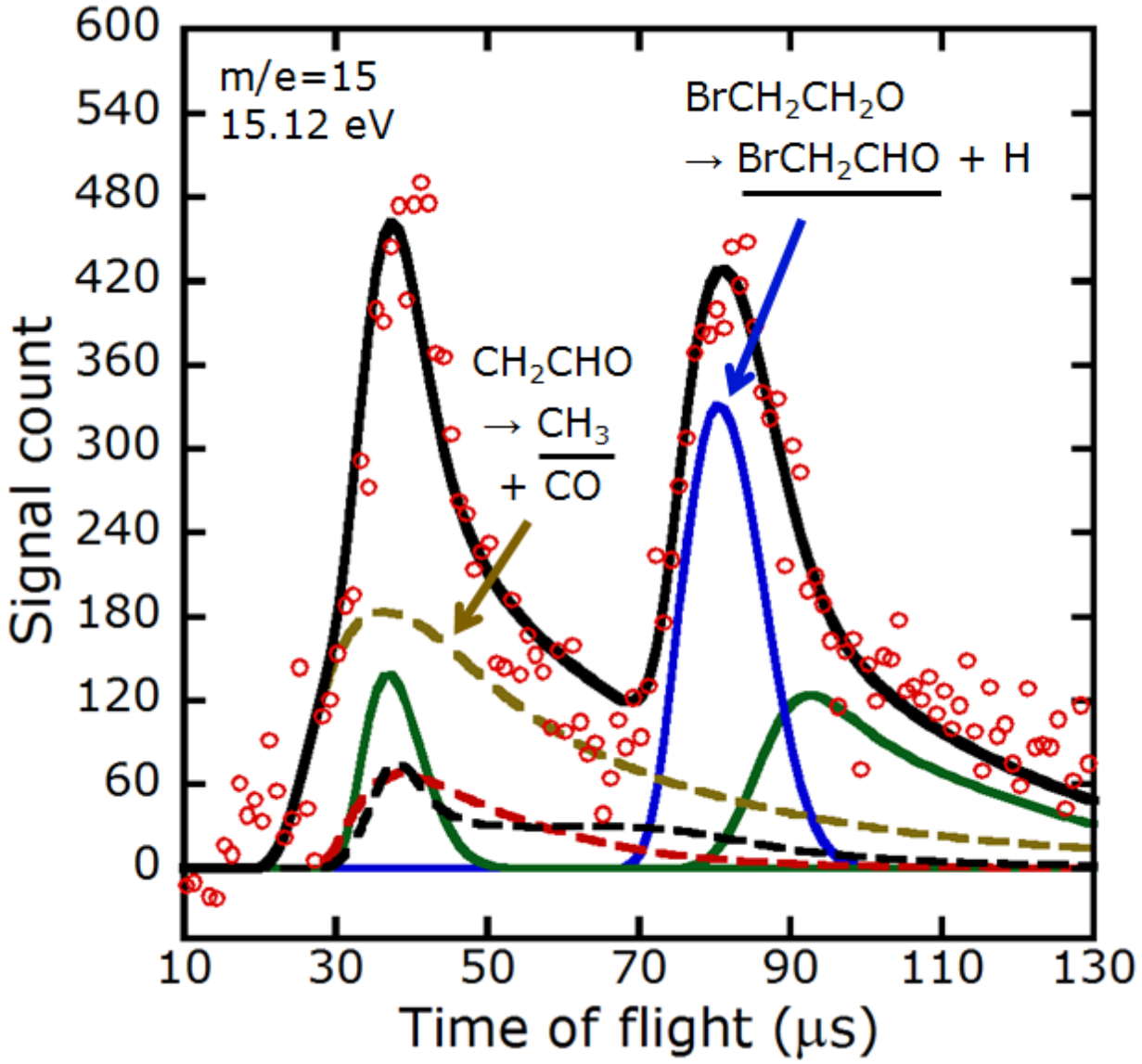

Figure 2.16. Time-of-flight spectrum of the signal at m/e=15 (CH_3^+) at a synchrotron energy of 15.12 eV. The most important feature is the strong contribution of CH_3 due to dissociation of vibrationally unstable vinoxy (dashed brown line with a maximum near 40 μs, Section 2.3.4.2). Other contributions are: dissociative ionization of $BrCH_2CHO$ from secondary dissociation of $BrCH_2CH_2O$ (solid blue line peaking near 80 μs, Section 2.3.5.3) and from photoelimination of HNO from $BrCH_2CH_2ONO$ (solid green line with a maximum near 90 μs, Section 2.3.2.2); dissociative ionization of vibrationally stable vinoxy formed from photodissociation of $BrCH_2CHO$ (solid green line, Section 2.3.4.1) and from secondary dissociation of CH_2CH_2ONO (dashed red line, Section 2.3.3.3); and dissociative ionization of vibrationally hot oxirane (dashed black line, Section 2.3.3.2).

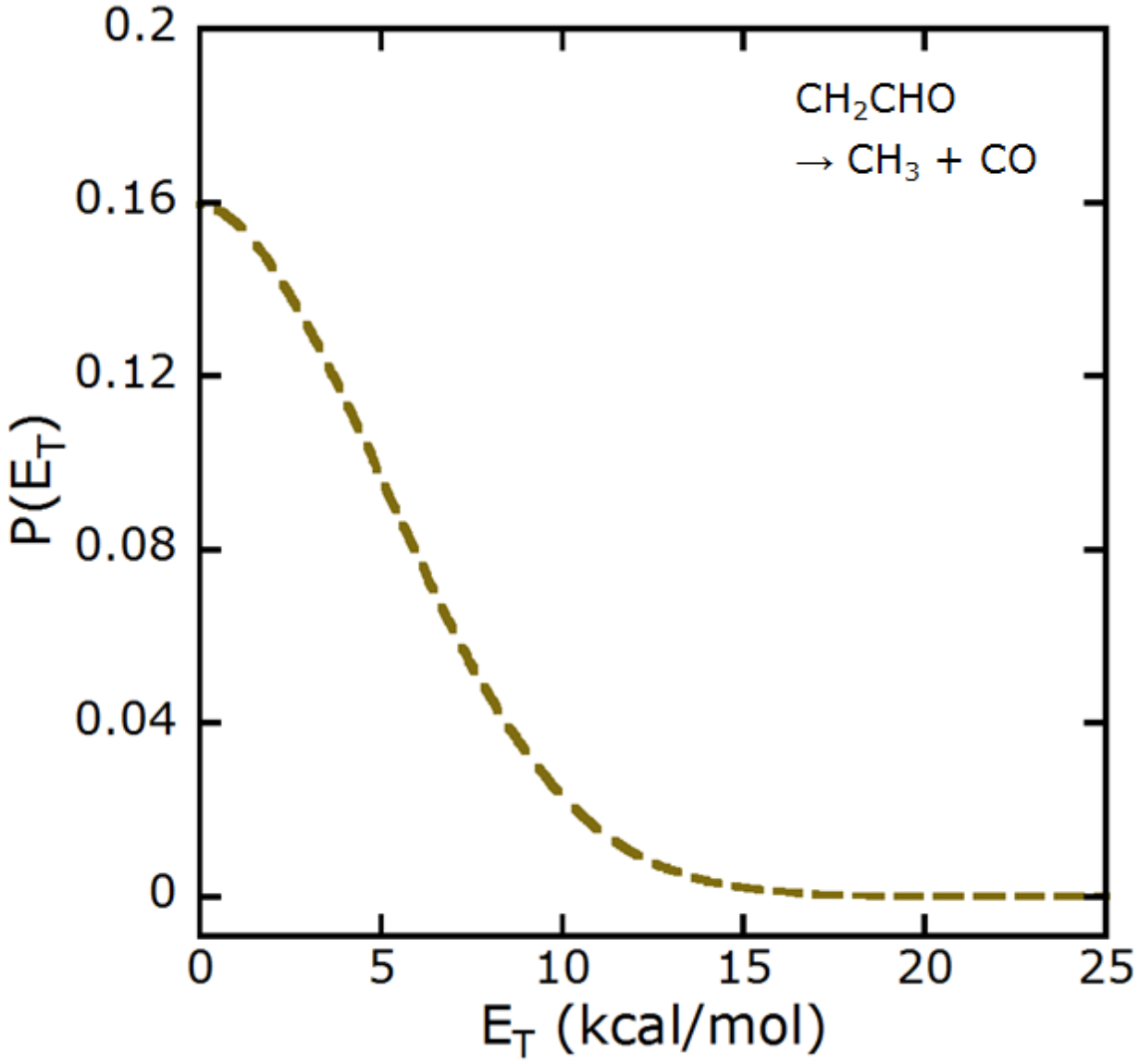

Figure 2.17. Product recoil kinetic energy distribution, $P(E_T)$, for the dissociation of vibrationally unstable vinoxy, $CH_2CHO \longrightarrow CH_3 + CO$. The distribution is approximately half-normal, with a standard deviation near 5 kcal/mol, and was derived by forward convolution fitting of the signal at m/e=15 (CH_3^+) of Figure 2.16. The TOF distribution predicted by this $P(E_T)$ is the dashed brown line in that figure.

2.3.5. Secondary dissociation of the $BrCH_2CH_2O$ radical formed from primary O-NO photofission

2.3.5.1. The $CH_2Br + H_2CO$ channel

This channel is easily characterized using the data at m/e=93 (CH_2Br^+), plotted in Figure 2.18. The signal is clearly forward-backward scattered with respect to the velocity vector of the primary $BrCH_2CH_2O$ fragments, so we used an angular distribution of $I(\theta)$ close to $1/\sin(\theta)$ (truncated near $\theta = 0°$ and 180°), shown in Figure 2.19. Figure 2.19 also shows the $P(E_T)$ giving the fit of Figure 2.18; it extends from 0 kcal/mol to approximately 40 kcal/mol, with a maximum near 15 kcal/mol. This $P(E_T)$ is similar to the one derived by Wang et al. for this channel,[33] but includes a contribution from higher E_T. However, the previous study assumed an isotropic $I(\theta)$ for this dissociation, because they were unable to distinguish signal due to backward-scattered CH_2Br fragments from signal due to photodissociation of clusters in the molecular beam. In this work, photoionization detection eliminates the contribution from the photodissociation of clusters, so all of the signal of Figure 2.18 arises from this CH_2Br channel. (We note in passing that the tail of the data at long time could include a contribution from the background signal described in Section 2.3.1. The background contribution, however, reaches its maximum near 220 μs, a time fairly well-separated from the more important data at 60-150 μs.)

The momentum-matched formaldehyde co-fragment of these CH_2Br fragments can be observed at m/e=30 (NO^+, H_2CO^+) at synchrotron energies above the 10.89 eV ionization threshold of H_2CO. In this experiment, the effective ionization threshold is somewhat lower, as the synchrotron radiation has nontrivial bandwidth (~4% FWHM) and the H_2CO is not vibrationally cold; thus we used a nominal synchrotron energy as low as 9.845 eV to collect data at m/e=30 with signal from NO^+ but none from H_2CO^+, and up to 11.06 eV to guarantee a large

signal from H_2CO^+. (At 11.06 eV, the photoionization cross section of H_2CO is ~11.4 Mb,[46] much larger than that of the other major product, NO, which is ~3.2 Mb.[52,53]) The data and fits at m/e=30 using ionization at 9.845 eV and 11.06 eV are shown in Figure 2.6; data and fits for other energies are presented in Appendix A. A contribution from the H_2CO co-fragment of CH_2Br, drawn as a dashed red line with a maximum near 40 μs, is clearly absent in the data at low synchrotron energy, but predictably increases with increasing energy. For these fits we also kept constant the relative intensities of contributions from different sources of NO, since we do not expect the photoionization cross section of NO from different sources to vary considerably over this energy range. Despite this assumption, the total fit describes the data well, supporting our assignment of the CH_2Br + H_2CO $P(E_T)$ and $I(\theta)$.

2.3.5.2. Photodissociation of CH_2Br

In the data of Figure 2.1 at m/e=79 (Br^+), there is signal at incredibly short flight times, on the order of 40 μs. To produce Br, a heavy fragment, with sufficient speed to have such a short flight time would require, by conservation of energy, more kinetic energy release (on the order of 80 kcal/mol) than is possible for single-photon dissociation of $BrCH_2CH_2ONO$. Consequently this signal must represent Br formed by a two-photon dissociation. It cannot arise from photodissociation of $BrCH_2CHO$, however, as there is no momentum-matched vinoxy signal to this Br. Instead, we fit it as photodissociation of the CH_2Br formed by the pathway described in Section 2.3.5.1. The fit is presented in Figure 2.1 as a dashed purple line. The TOF distribution was predicted by the usual forward convolution fitting process using the entire primary O-NO $P(E_T)$ of Figure 2.7, the entire $P(E_T)$ and $I(\theta)$ for secondary dissociation of $BrCH_2CH_2O$ of Figure 2.19, and a tertiary photodissociation $P(E_T)$ plotted in Figure 2.20 with an

isotropic I(θ). The total fit including this contribution from photodissociation of CH_2Br is seen to be quite satisfactory.

The $P(E_T)$ for this dissociation was estimated as follows. Reisler and co-workers have reported recoil kinetic energy distributions for the photodissociation of CH_2Cl at 312-214 nm, including a significant contribution of hot bands over part of this region.[54-56] The $P(E_T)$s at the shortest wavelengths (see Figure 6 in ref. 54) can be approximated by a normal distribution with a maximum at ~53% of the available energy (i.e., photon energy minus ΔH_{0K}) and a standard deviation of ~3500 cm^{-1}. Separately, others have found that in the photodissociation of both CH_3Cl[57] and CH_3Br[58] at 193 nm, ~96% of the available energy is partitioned into E_T. Given this similarity in the photodissociation dynamics of CH_3Cl and CH_3Br, we make the bold assumption that CH_2Br, like CH_2Cl, will photodissociate with a kinetic energy release normally distributed about a mean of ~53% of its available energy, with a standard deviation of ~3500 cm^{-1}. Since $\Delta H_{0K}(CH_2\text{-}Br)$ = 79.2 kcal/mol and the energy of a 193 nm photon is 147.8 kcal/mol, the available energy is at least 68.6 kcal/mol, and the maximum of the $P(E_T)$ occurs near (68.6 kcal/mol) × (53%) = 36 kcal/mol. We obtained a better fit by shifting this "guess" $P(E_T)$ by 6 kcal/mol, increasing the mean to 42 kcal/mol; this shift may be justified by noting that the vibrational energy of the hot CH_2Br fragments can contribute to E_T. The final $P(E_T)$, shown in Figure 2.20, gives the fit of the dashed purple line in the m/e=79 data of Figure 2.1.

2.3.5.3. The $BrCH_2CHO$ + H channel

$BrCH_2CH_2O$ radicals can undergo secondary dissociation via H loss, producing H + $BrCH_2CHO$. This channel was observed in both this study and the previous study by detecting the dissociative ionization products of $BrCH_2CHO$, which appear in much of the data of this

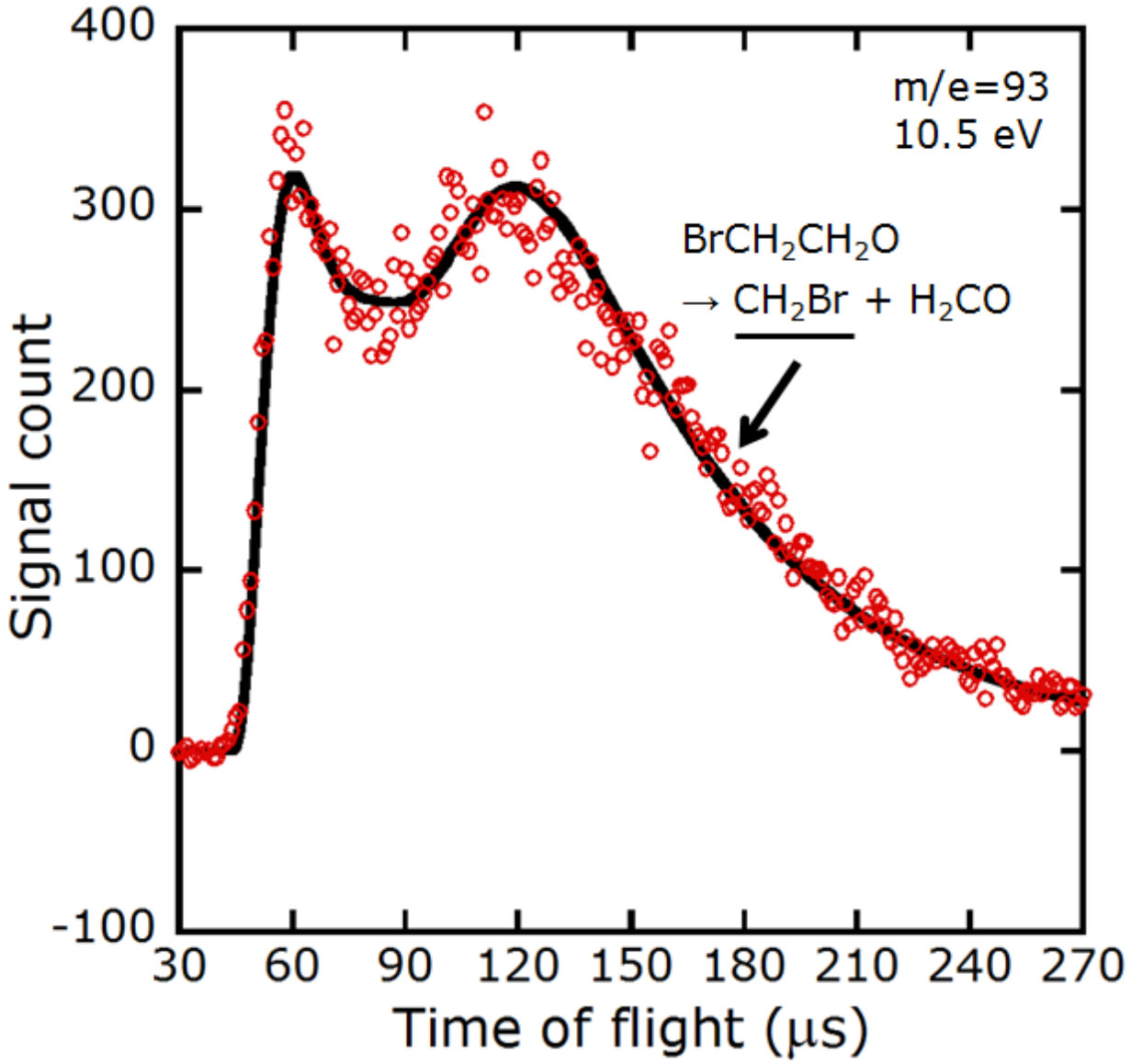

Figure 2.18. Time-of-flight spectrum and forward convolution fit of m/e=93 (CH_2Br^+) signal at a photoionization energy of 10.5 eV. The signal is seen to be forward-backward scattered. The only contribution included here is CH_2Br formed by secondary dissociation of $BrCH_2CH_2O$. There is expected to be some CH_2Br formed by C-C bond photofission in $BrCH_2CHO$; however, we were unable to fit the data well with this contribution included. We believe that the CH_2Br from $BrCH_2CH_2O$ is the overwhelmingly dominant contributor.

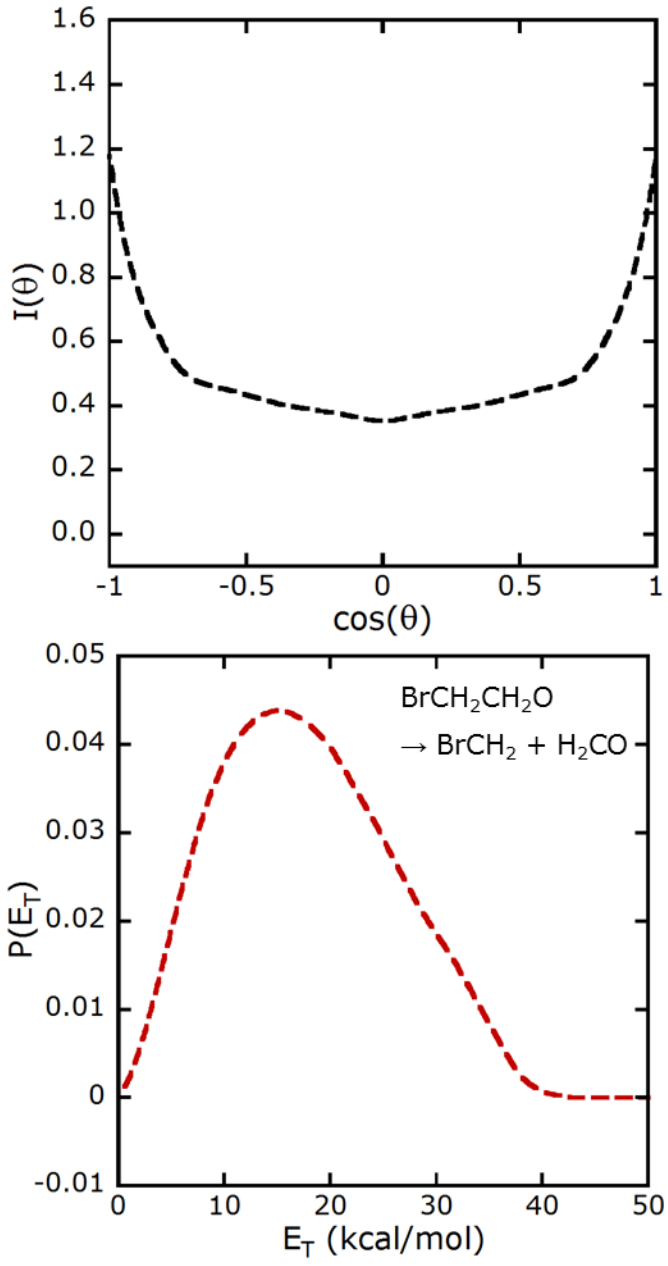

Figure 2.19. Angular distribution, I(θ), and product recoil kinetic energy distribution, $P(E_T)$, for the dissociation of $BrCH_2CH_2O$ radicals to $CH_2Br + H_2CO$. The $P(E_T)$ is derived by forward convolution fitting of the data at m/e=93 (CH_2Br^+) of Figure 2.18.

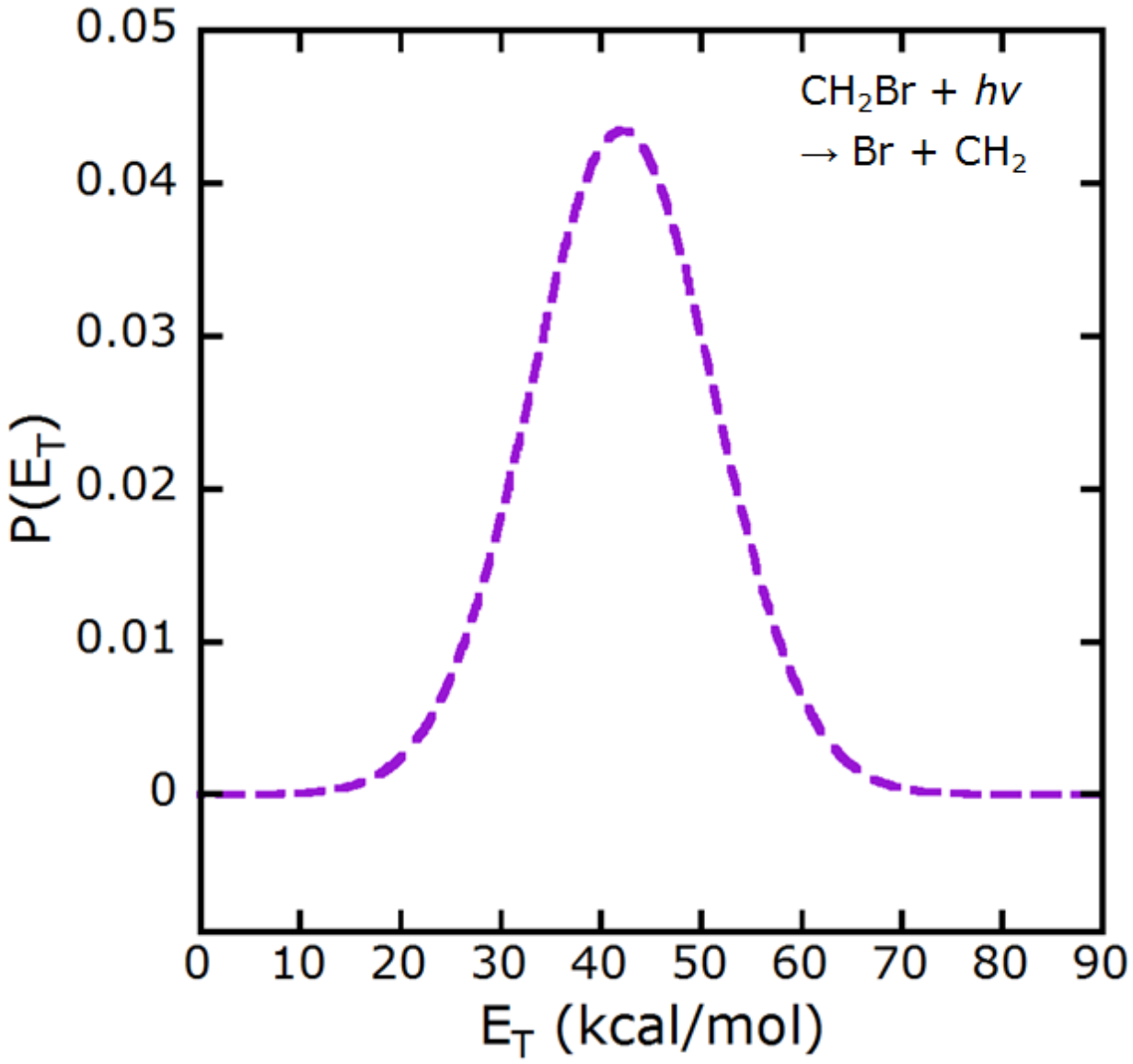

Figure 2.20. Photofragment recoil kinetic energy distribution, $P(E_T)$, used in the TOF prediction for the photodissociation $CH_2Br + h\nu \longrightarrow Br + CH_2$. The $P(E_T)$ is approximately a normal distribution centered at 42 kcal/mol with a standard deviation of 10 kcal/mol. It was derived by shifting the known $P(E_T)$ of the analogous photodissociation of CH_2Cl to higher E_T, as more energy is available to CH_2Br than to CH_2Cl; details are given in Section 2.3.5.2.

report and at m/e=29 and m/e=79 in the previous report; in this study we were moreover able to detect the parent cation at m/e=122. We include some further analysis of this pathway in Appendix A.

2.4. Discussion

The work reported here continues a previous study which explored the photochemistry of $BrCH_2CH_2ONO$ and its photofragment $BrCH_2CH_2O$ using 200 eV electron bombardment ionization. Insofar as this work overlaps theirs, the two are essentially in agreement, with the sole exception of the dissociation of $BrCH_2CH_2O$ to $CH_2Br + H_2CO$, which was fitted using an isotropic I(θ) in the previous study but I(θ) close to 1/sin(θ) here.

Nitrite photochemistry. A key new result of this work is the data and analysis at m/e=31 (HNO^+), which indicates formation of HNO as a primary photodissociation product of $BrCH_2CH_2ONO$ and as a secondary dissociation product of CH_2CH_2ONO. The appearance of HNO from an alkyl nitrite is typically ascribed to the kinetic disproportionation mechanism mentioned in the Introduction. There has been some debate in the literature regarding whether a monomeric nitrite can evolve HNO under collision-free conditions. Most relevant to the present study is that Bergmann and Huber,[22] in a laser-induced fluorescence experiment, observed HNO production from a molecular beam of methyl nitrite clusters ($[CH_3ONO]_n$, n ≈ 400-1000) photoexcited at 365 nm, which they attributed entirely to disproportionation within the clusters. The HNO signal in this work, however, cannot be assigned to photodissociation within nitrite clusters. The ion signal at m/e=31 (Figure 2.4) and m/e=30 (Figure 2.6) near 40 μs, and at m/e=15 (Figure 2.16) and m/e=29 (Appendix A) near 100 μs, is best explained as representing HNO and $BrCH_2CHO$ formed as momentum-matched co-fragments in the primary

photodissociation of $BrCH_2CH_2ONO$. In addition, the ion signal at m/e=31 (Figure 2.4) near 30 μs is best explained as HNO formed in the secondary dissociation of CH_2CH_2ONO, with a vinoxy co-fragment observed as ion signal at m/e=43 (Figure 2.12) near 45 μs and at m/e=15 (Figure 2.16) near 40 μs.

Comparing our conclusions on HNO to the conclusions of Bergmann and Huber, it might be inferred that alkyl nitrites photoexcited in the absorption band near 200 nm can access a unimolecular photoelimination channel leading to HNO, whereas no such channel occurs upon excitation near 350 nm. It is not clear whether this dissociation would occur through the excited state or following internal conversion to the ground state. It is also possible, though perhaps less likely, that a photodissociation channel leading to HNO is accessible exclusively in substituted alkyl nitrites. Further study is required to explore these questions.

Mechanism of dissociation of CH_2CH_2ONO to HNO + vinoxy. Our data and calculations show multiple dissociation pathways of the CH_2CH_2ONO radical. Based on the barrier heights and $P(E_{vib})$ of Figure 2.3, statistical transition state theory would predict overwhelming branching to the NO_2 + ethene products, with some small contribution of NO + oxirane and practically no contribution from HNO + vinoxy. The data do show strong signal due to NO_2 and ethene, but the signal due to HNO + vinoxy is unexpectedly competitive with the signal due to NO + oxirane. In this section we claim that the dissociation to HNO occurs through a non-intrinsic reaction coordinate (non-IRC) mechanism that circumvents the high-energy statistical transition state.

Two conceptually similar dissociations are $CH_3ONO \rightarrow HNO + H_2CO$, the subject of recent calculations by Zhu et al.[13,59], Isegawa et al.,[60] and Homayoon and Bowman;[14,15] and $CH_3CH_2ONO \rightarrow HNO + CH_3CHO$, which was approached theoretically by Liu et al.[25] and

experimentally by Prozument et al.[24] In both cases there is a conventional TS to HNO which is a few kcal/mol higher than the dissociation threshold to NO; the highest-energy TS of Figure 2.3 is analogous. However, the studies of Zhu et al., Isegawa et al., and Prozument et al. also suggest "roaming" pathways leading to HNO, with an energetic barrier approximately equal to the dissociation threshold to NO. In these pathways there is frustrated dissociation of the RO-NO bond, whereupon the RO and NO fragments orbit one another: the molecule samples a large region of its potential energy surface at no energetic penalty, until the geometric trajectory falls into an exoergic well. The existence of such a "roaming" pathway in CH_2CH_2ONO would explain our observation that dissociation to HNO + vinoxy is competitive with dissociation to NO + oxirane; this hypothetical feature is labeled "RTS?" in Figure 2.3. (The connection of RTS? to the HNO + vinoxy van der Waals well is inspired by the result of Homayoon and Bowman that CH_3ONO can dissociate to HNO via an HNO + H_2CO vdW complex, but is otherwise purely speculative.)

The analogy between CH_2CH_2ONO and the closed-shell nitrites is imperfect because the NO channel in CH_2CH_2ONO is exoergic with a high barrier, while in methyl and ethyl nitrite it is endoergic with negligible barrier above the endoergicity. The presence of a barrier to dissociation, from which both the NO and HNO pathways are exoergic, is suggestive of a bifurcation in the potential energy surface in the vicinity of that TS: having surmounted (or nearly surmounted) the dissociation barrier, the molecule may follow nuclear trajectories leading from the TS toward either the NO + oxirane well or the hypothesized NO roaming region. Numerous examples of potential energy surfaces with bifurcations of this type are now known, including unimolecular rearrangements and dissociations[61,62] as well as bimolecular reactions.[63,64] The common feature of such systems is that the dynamics in the vicinity of the

transition state, not the IRC, control the reactive trajectory.

In the case of CH_2CH_2ONO, such a bifurcation could be understood intuitively by supposing (following the argument of ref. 63) that the molecule's vibrational energy is not efficiently channeled into the O-NO stretching coordinate, so the orthogonal vibrational modes retain much of the vibrational energy and avoid the bond-breaking pathway. One feature of the experimental results provide a modicum of support for this interpretation. While the IRC trajectory toward NO + oxirane entails direct repulsion along the O-NO bond, the hypothetical non-IRC trajectory entails moving the NO in a sideways direction to abstract an H atom. Such a non-IRC pathway, then, might be expected to scatter HNO fragments sideways with respect to the NO fragments, as was observed in these experiments. A direct dynamics calculation beginning with the electronically excited precursor is required to fully characterize the angular distribution of the products from this hypothesized roaming channel.

Characterization of multiphoton dissociations. Our data evince significant multiphoton effects, namely in the photodissociation of $BrCH_2CHO$ to Br + vinoxy, CH_2Br to Br + CH_2, and NO_2 to NO + O. The photodissociation of these species has serendipitously allowed us to roughly characterize the photochemistry of $BrCH_2CHO$ and CH_2Br at 193 nm, and to show that vibrationally excited CH_2CH_2ONO can evolve NO_2 with the requisite internal energy to undergo photodissociation. In fitting these channels we have drawn parallels to previous work on the photodissociation of $ClCH_2CHO$ and $ClCH_2$, and the agreement of these fits with the data is quite good. It would be interesting to verify the $P(E_T)$s derived here by conducting a single-photon experiment on photodissociation of vibrationally cold $BrCH_2CHO$ monomers and CH_2Br.

2.5. References

1. Wayne, R. P. *Chemistry of Atmospheres*, 3rd ed. Oxford: Oxford University Press, 2000.

2. Calvert, J. G.; Pitts, J. N., Jr. *Photochemistry*. New York: Wiley, 1966.

3. McMillan, G. R.; Kumari, J.; Snyder, D. L. The Photolysis and Photooxidation of Alkyl Nitrites. In Tuesday, C. S., ed., *Chemical Reactions in Urban Atmospheres*, New York: Elsevier, 1971, pp. 35-43.

4. Dixon, R. N.; Rieley, H. State-selected Photodissociation Dynamics of HONO ($\tilde{A}^1A''$): Characterization of the NO Fragment. *J. Chem. Phys.* **1989**, *91*, 2308−2320.

5. Vasudev, R.; Zare, R. N.; Dixon, R. N. Dynamics of Photodissociation of HONO at 369 nm: Motional Anisotropy and Internal State Distribution of the OH Fragment. *Chem. Phys. Lett.* **1983**, *96*, 399−402.

6. Vasudev, R.; Zare, R. N.; Dixon, R. N. State-Selected Photodissociation Dynamics: Complete Charaterization of the OH Fragment Ejected by the HONO $\tilde{A}$ State. *J. Chem. Phys.* **1984**, *80*, 4863−4878.

7. Brühlmann, U.; Dubs, M.; Huber, J. R. Photodissociation of Methylnitrite: State Distributions, Recoil Velocity Distribution, and Alignment Effects of the NO($X^2\Pi$) Photofragment. *J. Chem. Phys.* **1987**, *86*, 1249−1257.

8. Benoist d'Azy, O.; Lahmani, F.; Lardeux, C.; Solgadi, D. State- Selective Photochemistry: Energy Distribution in the NO Fragment after Photodissociation of the CH_3ONO $n\pi^*$ State. *Chem. Phys.* **1985**, *94*, 247−256.

9. Lahmani, F.; Lardeux, C.; Solgadi, D. Rotational and Electronic Anisotropy in NO $X^2\Pi$ from the Photodissociation of CH_3ONO. *Chem. Phys. Lett.* **1986**, *129*, 24−30.

10. Winniczek, J. W.; Dubs, R. L.; Appling, J. R.; McKoy, V.; White, M. G. A Multiphoton

Ionization Study of the Photodissociation Dynamics of the S_2 State of CH_3ONO. *J. Chem. Phys.* **1989**, *90*, 949−963.

11. Yin, H. M.; Sun, J. L.; Li, Y. M.; Han, K. L.; He, G. Z. Photodissociation Dynamics of the S_2 State of CH_3ONO: State Distributions and Alignment Effects of the NO ($X^2\Pi$) Photofragment. *J. Chem. Phys.* **2003**, *118*, 8248−8255.

12. Jacox, M. E.; Rook, F. L. Photodecomposition of Methyl Nitrite Trapped in Solid Argon. *J. Phys. Chem.* **1982**, *86*, 2899-2904.

13. Zhu, R. S.; Raghunath, P.; Lin, M. C. Effect of Roaming Transition States upon Product Branching in the Thermal Decomposition of CH_3NO_2. *J. Phys. Chem. A* **2013**, *117*, 7308−7313.

14. Homayoon, Z.; Bowman, J. M. Quasiclassical Trajectory Study of CH_3NO_2 Decomposition via Roaming Mediated Isomerization Using a Global Potential Energy Surface. *J. Phys. Chem A* **2013**, *117*, 11665-11672.

15. Bowman, J. M. Roaming. *Mol. Phys.* **2014**, *112*, 2516-2528.

16. Schwartz-Lavi, D.; Bar, I.; Rosenwaks, S. Rotational Alignment and Non-Statistical Λ Doublet Population in NO Following $(CH_3)_3CONO$ Photodissociation. *Chem. Phys. Lett.* **1986**, *128*, 123−126.

17. Schwartz-Lavi, D.; Rosenwaks, S. Scalar and Vectorial Properties in the Photodissociation of tert-Butyl Nitrite from the S1 and S2 States. *J. Chem. Phys.* **1988**, *88*, 6922−6930.

18. Fitzmaurice, D. J.; Frei, H. Electronic Absorption of Alkyl Nitrite Radicals in the 300-700 nm Region. *Chem. Phys. Lett.* **1992**, *192*, 166-172.

19. Furlan, A. Photodissociation of an Alkyl Nitrite at a Liquid Surface: Flight-time Distributions of NO and HNO. *Chem. Phys. Lett.* **1999**, *309*, 157-164.

20. Mátyus, E.; Magyarfalvi, G.; Tarczay, G. Conformers and Photochemistry of Propyl Nitrites:

A Matrix Isolation Study. *J. Phys. Chem. A.* **2007**, *111*, 450-459.

21. Müller, R.-P.; Murata, S.; Nonella, M.; Huber, J. R. HNO, an Intermediate in (Light-induced) Rearrangement Reactions of Nitrosooxy Compounds and Nitrosamines. *Helv. Chim. Acta* **1984**, *67*, 953-958.

22. Bergmann, K.; Huber, J. R. Photoinduced Bimolecular Reactions in Homogeneous $[CH_3ONO]_n$ Clusters. *J. Phys. Chem. A* **1997**, *101*, 259-267.

23. Batt, L.; Milne, R. T. The Gas-Phase Pyrolysis of Alkyl Nitrites. IV. Ethyl Nitrite. *Int. J. Chem. Kineti.* **1977**, *9*, 549-565.

24. Prozument, K.; Suleimanov, Y. V.; Buesser, B.; Oldham, J. M.; Green, W. H.; Suits, A. G.; Field, R. W. A Signature of Roaming Dynamics in the Thermal Decomposition of Ethyl Nitrite: Chirped-Pulse Rotational Spectroscopy and Kinetic Modeling. *J. Phys. Chem. Lett.* **2014**, *5*, 3641-3648.

25. Liu, Y.; Li, X.; Tian, G.; Li, X.; Sun, Z. Theoretical Study on the Reaction Mechanism of CH_3CH_2O Radical with NO. *Comp. Theoret. Chem.* **2014**, *1032*, 84-89.

26. Von Glasow, R.; Crutzen, P. J. Tropospheric Halogen Chemistry. In Keeling, R. F., *The Atmosphere*, Oxford: Oxford University Press, 2007, pp. 21–64.

27. Knipping, E. M.; Lakin, M. J.; Foster, K. L.; Jungwirth, P.; Tobias, D. J.; Gerber, R. B.; Dabdub, D.; Finlayson-Pitts, B. J. Experiments and Simulations of Ion-Enhanced Interfacial Chemistry on Aqueous NaCl Aerosols. *Science* **2000**, *288*, 301−306.

28. Thornton, J. A.; Kercher, J. P.; Riedel, T. P.; Wagner, N. L.; Cozic, J.; Holloway, J. S.; Dube, W. P.; Wolfe, G. M.; Quinn, P. L.; Middlebrook, A. M.; Alexander, B.; Brown, S. S. A Large Atomic Chlorine Source Inferred from Mid-continental Reactive Nitrogen Chemistry. *Nature* **2010**, *464*, 271−274.

29. Calvert, J. G.; Atkinson, R.; Kerr, J. A.; Madronich, S.; Moortgat, G. K.; Wallington, T. J. *The Mechanisms of Atmospheric Oxidation of the Alkenes*. New York: Oxford University Press, 2000.

30. Nakata, M.; Shibuya, K.; Frei, H. Vibronic Excitation of Oxygen-Atom Transfer from NO_2 to Ethylene by Long-Wavelength Visible Light in a Cryogenic Matrix. *J. Phys. Chem.* **1990**, *94*, 8168-8175.

31. Chhantyal-Pun, R.; Chen, M.-W.; Sun, D.; Miller, T. A. Detection and Characterization of Products from Photodissociation of XCH_2CH_2ONO (X = F, Cl, Br, OH). *J. Phys. Chem. A* **2012**, *116*, 12032-12040.

32. Wang, L.; Lam, C.-S.; Chhantyal-Pun, R.; Brynteson, M. D.; Butler, L. J.; Miller, T. A. Imaging and Scattering Studies of the Unimolecular Dissociation of the $BrCH_2CH_2ONO$ Radical from $BrCH_2CH_2ONO$ Photolysis at 351 nm. *J. Phys. Chem. A* **2014**, *118*, 404-416.

33. Wang, L.; Scrape, P. G.; Roberts, T. D.; Joshi, P. P.; Butler, L. J. Competing C-Br and O-NO Photofission upon Excitation of $BrCH_2CH_2ONO$ at 193 nm. *J. Phys. Chem. A* **2015**, in press (DOI: 10.1021/acs.jpca.5b04162).

34. Ratliff, B. J.; Alligood, B. W.; Butler, L. J.; Lee, S.-H.; Lin, J. J.-M. Product Branching from the CH_2CH_2OH Radical Intermediate of the OH + Ethene Reaction. *J. Phys. Chem. A* **2011**, *115*, 9097−9110.

35. Lin, J. J.; Chen, Y.; Lee, Y. Y.; Lee, Y. T.; Yang, X. Photodissociation Dynamics of CH_3Cl at 157.6 nm: Evidence for $CH_2(\tilde{X}^3B_1/\tilde{a}^1A_1)$+HCl Product Channels. *J. Chem. Phys. Lett.* **2002**, *361*, 374−382.

36. Lee, S.-H.; Lee, Y.-Y.; Lee, Y. T.; Yang, X. Photodissociation Dynamics of Propene at 157.6 nm: Kinetic Energy Distributions and Branching Ratios. *J. Chem. Phys.* **2003**, *119*, 827−838.

37. *CMLAB2*, version 6/93, modified by J. D. Myers. This is an interactive version built on the original cmlab2 program: X. Zhao, Ph.D. dissertation, University of California, 1988.

38. M. J. Frisch, G. W. Trucks, H. B. Schlegel et al., GAUSSIAN 09, Revision A.02, Gaussian, Inc., Wallingford, CT, 2009.

39. Schaftenaar, G.; Noordik, J. H. Molden: a Pre- and Post-processing Program for Molecular and Electronic Structures. *J. Comput.-Aided Mol. Design* **2000**, *14*, 123-134.

40. Womack, C. C.; Fang, W.-H.; Straus, D. B.; Butler, L. J. Assessing an Impulsive Model for Rotational Energy Partitioning to Acetyl Radicals from the Photodissociation of Acetyl Chloride at 235 nm. *J. Phys. Chem. A* **2010**, *114*, 13005-13010.

41. McKown, B. G.; Ceriotti, M.; Womack, C. C.; Kamarchik, E.; Butler, L. J.; Bowman, J. M. Effects of High Angular Momentum on the Unimolecular Dissociation of CD_2CD_2OH: Theory and Comparisons with Experiment. *J. Phys. Chem. A* **2013**, *117*, 10951-10963.

42. Brynteson, M. D.; Butler, L. J. Predicting the Effect of Angular Momentum on the Dissociation Dynamics of Highly Rotationally Excited Radical Intermediates. *J. Chem. Phys.* **2015**, *142*, 054301.

43. B. Ruscic, Active Thermochemical Tables (ATcT) values based on ver. 1.112 of the Thermochemical Network (2013); available at ATcT.anl.gov.

44. Bozkaya, U.; Turney, J. M.; Yamaguchi, Y.; Schaefer, H. F., III. The Lowest-lying Electronic Singlet and Triplet Potential Energy Surfaces for the HNO-NOH System: Energetics, Unimolecular Rate Constants, Tunneling and Kinetic Isotope Effects for the Isomerization and Dissociation Reactions. *J. Chem. Phys.* **2012**, *136*, 164303.

45. Niu, B.; Shirley, D. A.; Bai, Y. High Resolution Photoelectron Spectroscopy and Femtosecond Intramolecular Dynamics of H_2CO^+ and D_2CO^+. *J. Chem. Phys.* **1993**, *98*, 4377-

4390.

46. Dodson, L. G.; Shen, L.; Savee, J. D.; Eddingsaas, N. C.; Welz, O.; Taatjes, C. A.; Osborn, D. L.; Sander, S. P.; Okumura, M. VUV Photoionization Cross Sections of HO_2, H_2O_2, and H_2CO. *J. Phys. Chem. A* **2015**, *119*, 1279-1291.

47. Huber, K. P.; Herzberg, G. *Molecular Spectra and Molecular Structure, IV. Constants of Diatomic Molecules*. Van Nostrand Reinhold Company, 1979.

48. Miller, J. L.; McCunn, L. R.; Krisch, M. J.; Butler, L. J.; Shu, J. Dissociation of the Ground State Vinoxy Radical and its Photolytic Precursor Chloroacetaldehyde: Electronic Nonadiabaticity and the Suppression of the H+ketene Channel. *J. Chem. Phys.* **2004**, *121*, 1830-1838.

49. Nelson, L.; Shanahan, I.; Sidebottom, H. W. Kinetics and Mechanism for the Oxidation of 1,1,1-Trichloroethane. *Int. J. Chem. Kinet.* **1990**, *22*, 577-590.

50. Booth, R. S.; Brynteson, M. D.; Lee, S.-H.; Lin, J. J.; Butler, L. J. Further Studies into the Photodissociation Pathways of 2-Bromo-2-nitropropane and the Dissociation Channels of the 2-Nitro-2-propyl Radical Intermediate. *J. Phys. Chem. A* **2014**, *118*, 4707-4722.

51. Butler, L. J.; Krajnovich, D.; Lee, Y. T.; Ondrey, G. S.; Bersohn, R. The Photodissociation of Nitromethane at 193 nm. *J. Chem. Phys.* **1983**, *79*, 1708-1722.

52. Watanabe, K.; Matsunaga, F. M.; Sakai, H. Absorption Coefficient and Photoionization Yield of NO in the Region 580-1350 Å. *Appl. Opt.* **1967**, *6*, 391-396.

53. Watanabe, K.; Matsunaga, F. M.; Sakai, H. Erratum to ref. 50. *Appl. Opt.* **1967**, *6*, 1220.

54. Dribinski, V.; Potter, A. B.; Demyanenko, A. V.; Reisler, H. Photodissociation Dynamics of the CH_2Cl Radical: Ion Imaging Studies of the $Cl+CH_2$ Channel. *J. Chem. Phys.* **2001**, *115*, 7474-7484.

55. Potter, A. B.; Dribinski, V.; Demyanenko, A. V.; Reisler, H. Competitive Channels in the Jet-cooled Photodissociation of the CH_2Cl Radical. *Chem. Phys. Lett.* **2001**, *349*, 257-265.

56. Levchenko, S. V.; Demyanenko, A. V.; Dribinski, V. L.; Potter, A. B.; Reisler, H.; Krylov, A. I. Rydberg-valence Interactions in $CH_2Cl \rightarrow CH_2+Cl$ Photodissociation: Dependence of Absorption Probability on Ground State Vibrational Excitation. *J. Chem. Phys.* **2003**, *118*, 9233-9240.

57. Townsend, D.; Lee, S. K.; Suits, A. G. DC Slice Imaging of CH_3Cl Photolysis at 193.4 nm. *J. Phys. Chem. A* **2004**, *108*, 8106-8114.

58. Wang, F.; Lipciuc, M. L.; Kartakoullis, A.; Glodic, P.; Samartzis, P. C.; Yang, X.; Kitsopoulos, T. N. Slice Imaging of Methyl Bromide Photofragmentation at 193 nm. *Phys. Chem. Chem. Phys.* **2014**, *16*, 599-606.59. Zhu, R. S.; Lin, M. C. CH_3NO_2 decomposition/isomerization mechanism and product branching ratios: An *ab initio* chemical kinetic study. *Chem. Phys. Lett.* **2009**, *478*, 11-16.

60. Isegawa, M.; Liu, F.; Maeda, S.; Morokuma, K. *Ab initio* reaction pathways for photodissociation and isomerization of nitromethane on four singlet potential energy surfaces with three roaming paths. *J. Chem. Phys.* **2014**, *140*, 244310.

61. Ess, D. H.; Wheeler, S. E.; Iafe, R. G.; Xu, L.; Çelebi-Ölçüm, N.; Houk, K. N. Bifurcations on Potential Energy Surfaces of Organic Reactions. *Angew. Chem. Int. Ed.* **2008**, *47*, 7592-7601.

62. Ammal, S. C.; Yamataka, H.; Aida, M.; Dupuis, M. Dynamics-Driven Reaction Pathway in an Intramolecular Rearrangement. *Science* **2003**, *299*, 1555-1557.

63. Lourderaj, U.; Park, K.; Hase, W. L. Classical Trajectory Simulations of Post-transition State Dynamics. *Int. Rev. Phys. Chem.* **2008**, *27*, 361-403.

64. López, J. G.; Vayner, G.; Lourderaj, U.; Addepalli, S. V.; Kato, S.; deJong, W. A.; Windus,

T. L.; Hase, W. L. A Direct Dynamics Trajectory Study of F^- + CH_3OOH Reactive Collisions Reveals a Major Non-IRC Reaction Path. *J. Am. Chem. Soc.* **2007**, *129*, 9976-9985.

CHAPTER 3

A MOLECULAR BEAM STUDY OF DICHLOROMETHANE AND A MEASUREMENT OF THE PHOTOIONIZATION CROSS SECTION OF CHLOROMETHYL RADICAL

This work has been submitted for publication in Chemical Physics Letters.

3.1. Introduction

Methyl radicals and their derivatives are important intermediates in atmospheric and combustion processes: they participate in the formation and destruction of larger species and, in the stratosphere, they catalyze the decomposition of ozone.[1,2] Halogen-substituted methyl radicals such as CH_2Cl are generated by decomposition of organic solvents, as well as by the action of atmospheric Cl or Cl_2 on organic species; these radicals serve as sources of atomic halogens in addition to their usual functions.[3] In the study of reaction mechanisms and product branching ratios in systems involving substituted methyl radicals, one useful tool is photoionization mass spectrometry; however, quantitative analysis of product branching in kinetics experiments requires knowledge of the absolute photoionization cross sections of the species under investigation. These cross sections are often unknown and difficult to determine experimentally, even for small species, due to the difficulty of designing an experiment that can measure the number density of both the neutral species and their ions.[4]

Photofragment translational spectroscopy provides a solution to this quandary for many species: by selecting a photolytic precursor of the form X–Y which undergoes the reaction X–Y + $h\nu \rightarrow$ X + Y, one is assured that the neutrals X and Y are produced in a one-to-one ratio. The

measured ratio of signal due to their ions X^+ and Y^+ is then related to the ratio of their cross sections by a simple proportion; if the cross section of one is known and that of the other is desired, the missing value is easily obtained by correcting the observed ratio of ion signals for kinematic factors.[5] In this work, we apply the method of photofragment translational spectroscopy to determine the photoionization cross section of CH_2Cl at 13.7 eV; this result is sufficient to quantitatively anchor studies of the energy-dependent photoionization cross section of this radical.

Dichloromethane (CH_2Cl_2) photoexcited at 157 nm was chosen for this work because it undergoes the dissociation CH_2Cl_2 + 157 nm → CH_2Cl + Cl, and the absolute photoionization cross section of Cl is known over a wide range of energies.[6-8] We also characterize the other major photodissociation pathway of CH_2Cl_2, namely dissociation to HCl + CHCl. This additional characterization was necessary to accurately determine the photoionization cross section of CH_2Cl, as some of the ion signal at both *m/e*=35 (Cl^+) and *m/e*=49 (CH_2Cl^+) arises from detection of HCl, CHCl, and their dissociative ionization daughter fragments.

3.2. Methods

All data were collected at the National Synchrotron Radiation Research Center (NSRRC) in Hsinchu, Taiwan, using the U9 Chemical Dynamics Beamline. Photofragment translational spectroscopy was performed using a crossed laser-molecular beam scattering apparatus that has been described in detail elsewhere.[9-11] Briefly, a molecular beam of CH_2Cl_2 was created by seeding the equilibrium vapor pressure of the liquid, held at -20 °C, to a total pressure of 600 torr in neon. The gas mixture was supersonically expanded into a rotating source chamber through a pulsed nozzle operating at 100 Hz; the nozzle was held at 60 °C to inhibit the formation of

clusters. The rotating source was set at an angle of 20° with respect to the axis of the detector for all photodissociation experiments. The molecular beam was crossed perpendicularly with the unpolarized 157 nm output of a LPF 200 Lambda Physik Laser Technik laser, timed to fire approximately 240 μs after the nozzle so as to intersect the most dense region of the molecular beam pulse.

In these experiments, the net velocity of the primary photofragments is the vector sum of the precursor molecule's velocity in the beam and the velocity imparted by the photodissociation process. Products from the secondary dissociation of vibrationally hot photofragments or from secondary photodissociation also have additional velocity imparted during the secondary process. Photofragments with net velocity vectors pointing along the axis of the detector traveled 10.05 cm to enter the detector's ionizer, where they were photoionized by tunable VUV radiation from the synchrotron (with higher harmonics filtered by a 30 cm gas cell containing ~10 torr of argon). The resulting ions were propelled by a series of ion lenses through a quadrupole mass filter, and finally the mass-filtered ions were counted in a Daly detector. The time-dependent ion signal was binned by a multichannel scaler in 1 μs intervals measured from the time of the 157 nm laser shot. The ions' flight times, from the ionizer to the Daly detector, were calculated using the instrument's calibrated ion flight constant of 5.43 μs $amu^{-1/2}$; the neutral fragments' flight time is obtained by subtracting the ion flight time from the total measured flight time. All of the time-of-flight (TOF) spectra in this report show only the neutral flight time.

Recoil kinetic energy distributions (P(E_T)s) were fitted to the data using the method of forward convolution fitting. Fitting was performed using the CMLAB2 program.[12] The precursor beam velocity was characterized using the photodepletion (hole-burning) method. Typical beam speeds were 750 m/s with a full width at half maximum of approximately 200 m/s.

All calculations of molecular geometries and energies were performed at the G4//B3LYP/6-311++G(3df,2p) level of theory using the Gaussian 09 software package.[13]

3.3. Results and analysis

3.3.1. Overview

Dichloromethane may undergo four photodissociation channels at 157 nm:

$$CH_2Cl_2 + h\nu \rightarrow Cl + CH_2Cl \quad \Delta H_{0K} = 77.1 \text{ kcal/mol} \quad (1)$$

$$\rightarrow HCl + CHCl \quad \Delta H_{0K} = 75.4 \text{ kcal/mol} \quad (2)$$

$$\rightarrow H + CHCl_2 \quad \Delta H_{0K} = 93.7 \text{ kcal/mol} \quad (3)$$

$$\rightarrow Cl_2 + CH_2 \quad \Delta H_{0K} = 114.2 \text{ kcal/mol} \quad (4)$$

The vibrationally hot products may then undergo dissociation to a variety of secondary products. Figure 3.1 summarizes the endoergicities of the dissociation channels of CH_2Cl_2 and its products (some of the reactions may have substantial barriers to them but they are not shown in the figure). Based on the high endoergicities of the product channels, secondary dissociation of CH_2Cl is highly improbable, while some secondary dissociation of CHCl may be expected. This possibility is explored further in the analysis of the HCl photoelimination channel.

We frame our presentation of the data and analysis as follows. In Section 3.3.2 we discuss the photodissociation channel to Cl + CH_2Cl; the data corresponding to this primary channel are, for the most part, easily fitted. In Section 3.3.3, we discuss the channel to HCl + CHCl; the kinetic energy release of this dissociation is quite complicated, and some of the CHCl fragments undergo dissociative ionization to Cl^+ or secondary dissociation to CCl, so these data are more challenging to interpret. For completeness, we briefly mention the minor products H +

$CHCl_2$ and Cl_2 + CH_2 in Section 3.3.4. The impact of possible errors in these fits are described in Section 3.3.5. The key result of this study is the photoionization cross section of CH_2Cl at 13.7 eV, which we determine in Section 3.3.6 based on the data of Section 3.3.2.

3.3.2. Primary photodissociation to Cl + CH_2Cl

Photoexcitation may cleave one of the two C−Cl bonds directly, producing the fragments Cl + CH_2Cl. This channel is evidenced by detection of Cl^+ and CH_2Cl^+ cations at *m/e*=35 and *m/e*=49, respectively. Time-of-flight (TOF) data collected at *m/e*=35 are plotted in Figure 3.2, and data collected at *m/e*=49 are plotted in Figure 3.3. The fitted TOF distribution arising from this channel is a strong peak at short flight time, and is indicated in the figures. The distribution of recoil kinetic energies, P(E_T), imparted during C−Cl photofission was determined from the forward convolution fit to the TOF data; it is shown in Figure 3.4. The C−Cl photofission P(E_T) has a typical bell shape extending to ~80 kcal/mol with a maximum near 55 kcal/mol; the typical shape and high kinetic energy release indicate that C−Cl photofission is an excited-state process occurring on a repulsive part of the potential energy surface.

A prominent feature of each set of data deserves special mention. First, ions of *m/e*=36 (HCl^+) were also detected at *m/e*=35, due to the low resolution of the quadrupole mass selector. This "background" signal is accounted for by simply including the fitted TOF distribution of $H^{35}Cl^+$, which is discussed in the next section. Second, at *m/e*=49 there was a strong, broad signal produced by the molecular beam at long flight times, which did not depend on the photolysis laser power. This signal was removed by first collecting data at *m/e*=49 without the laser firing, and then subtracting this background from the raw data. For clarity, Figure 3.3 includes subtraction of this background signal. The raw data and the isolated background signal

are provided in Appendix B.

3.3.3. Photoelimination leading to HCl + CHCl

As usual for alkyl chlorides, photoexcitation of CH_2Cl_2 may lead to HCl elimination, with a cofragment of CHCl. This channel must be characterized in this study because $CH^{37}Cl$ may dissociate or dissociatively ionize directly to $C^{37}Cl$, a fragment of mass 49 like $CH_2{}^{35}Cl$; moreover, $H^{35}Cl^+$ and $CH^{37}Cl^+$ produce signal at *m/e*=35 and *m/e*=49, respectively, due to the low resolution of the quadrupole.

TOF data collected at *m/e*=38 ($H^{37}Cl^+$) and the forward convolution fit to the data are shown in Figure 3.5. We fit the data as arising from primary HCl photoelimination, with a broad distribution of kinetic energy. The data must be from this channel, because no significant amount of any other fragment can dissociate to HCl under 157 nm photoexcitation; nor can any fragment that has a TOF distribution matching the *m/e*=38 data dissociatively ionize to HCl^+ at 13.7 eV. Furthermore, photodissociation of a secondary fragment to HCl is excluded by observing that the high kinetic energy TOF signal scales with laser power identically to the other signal in the TOF spectrum. The black line in Figure 3.5 indicates the fitted TOF distribution of primary HCl photofragments, and the corresponding $P(E_T)$ is plotted as a blue dashed line in Figure 3.6.

The $P(E_T)$ includes three key features: a peak near 5 kcal/mol, a peak near 20 kcal/mol, and a flat section stretching from 40 kcal/mol to 70 kcal/mol. The appearance of multiple features likely arises in part because the CHCl fragment may be formed in either its ground singlet state or its lowest triplet state, which lies 6.5 kcal/mol above the ground state. This idea was proposed by Lin et al. when they reported a bimodal $P(E_T)$ for HCl photoelimination from the analogous molecule CH_3Cl at 157 nm.[10] In the case of CH_2Cl_2, the presence of two Cl atoms

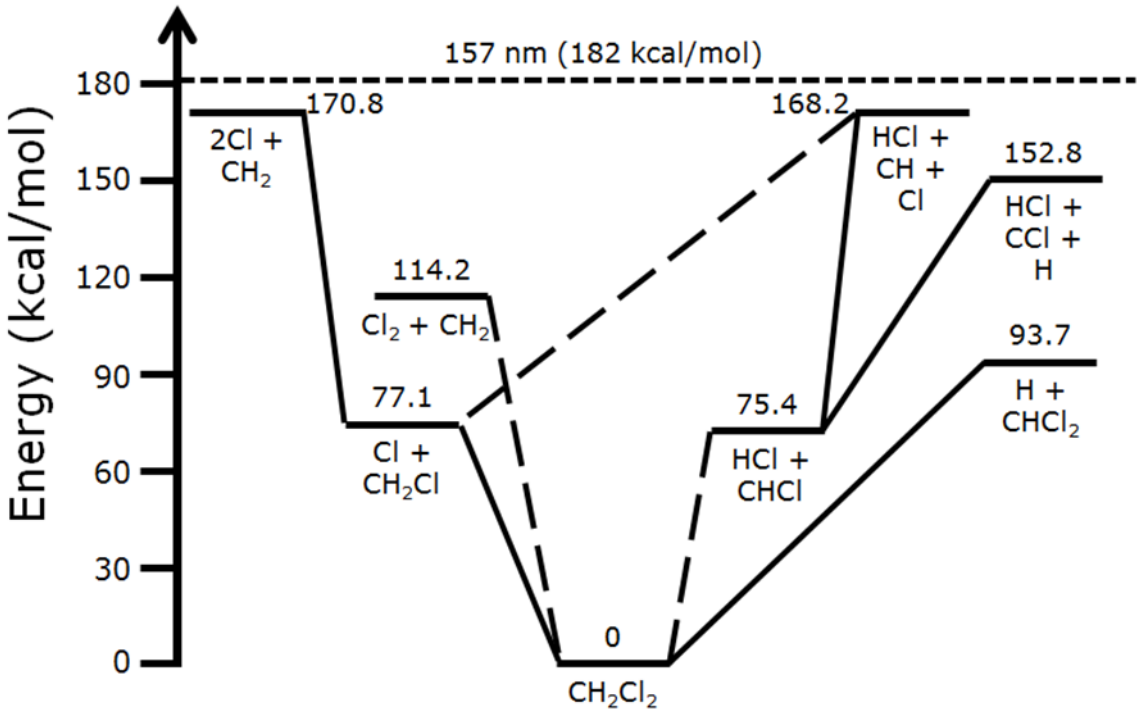

Figure 3.1. Zero-point corrected, ground-state energies of several dissociation products of CH_2Cl_2. Only endoergicities are shown; barrier heights were not calculated. Solid lines indicate simple bond fission pathways which are expected to have no or negligible barrier above the endoergicity, while dashed lines indicate more complex pathways that likely do have a barrier. The triplet state of CHCl lies 6.5 kcal/mol above the singlet ground state.

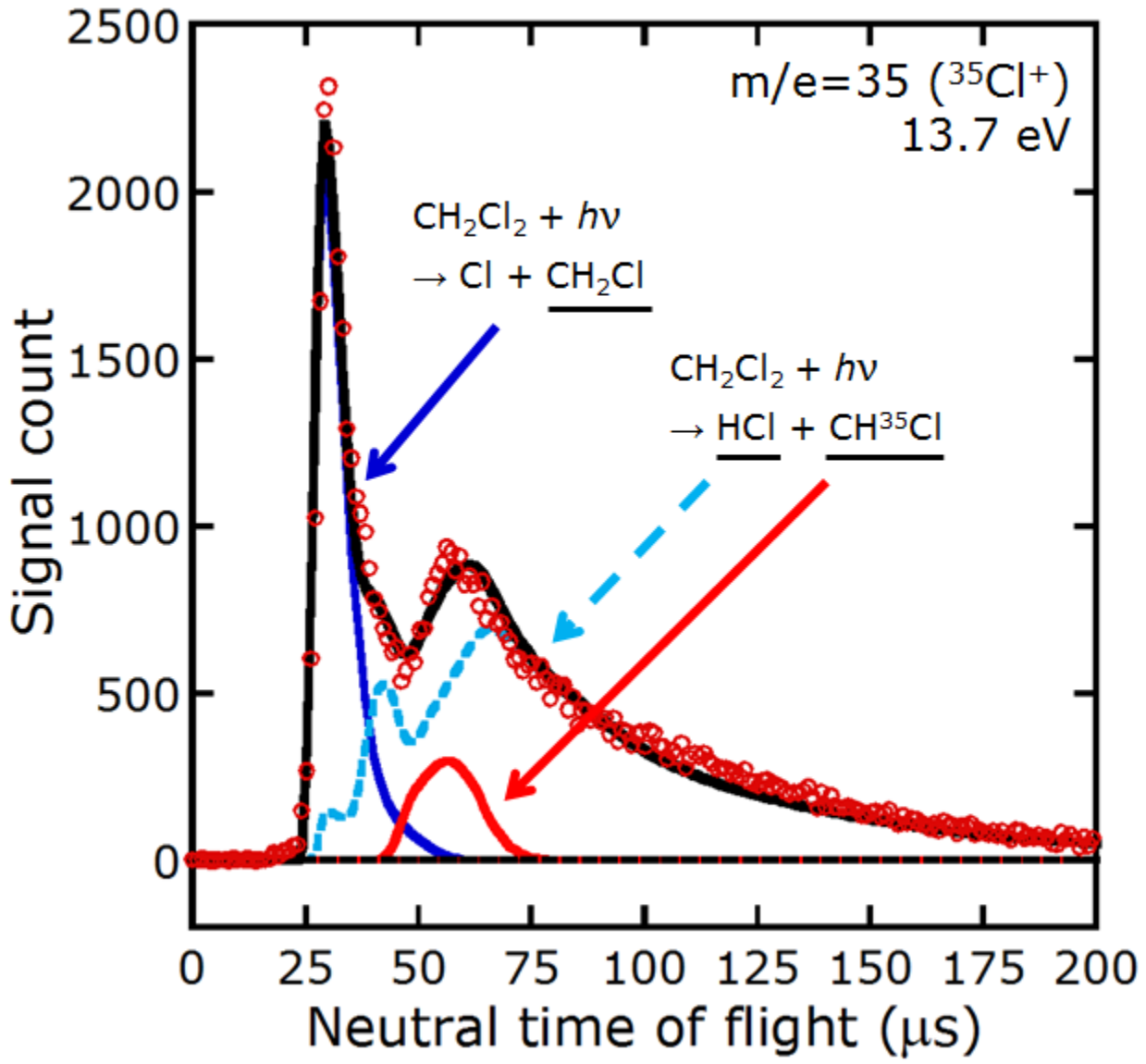

Figure 3.2. Time-of-flight data collected at a mass-to-charge setting of *m/e*=35 ($^{35}Cl^+$). Primary photodissociation produces atomic Cl, with the TOF distribution plotted as the solid blue curve. The data have a contribution from ions of *m/e*=36 (plotted as the dashed light blue line) due to the low resolution of the quadrupole. The red curve peaking near 55 μs arises from dissociative ionization of vibrationally hot CHCl fragments that are stable to secondary dissociation.

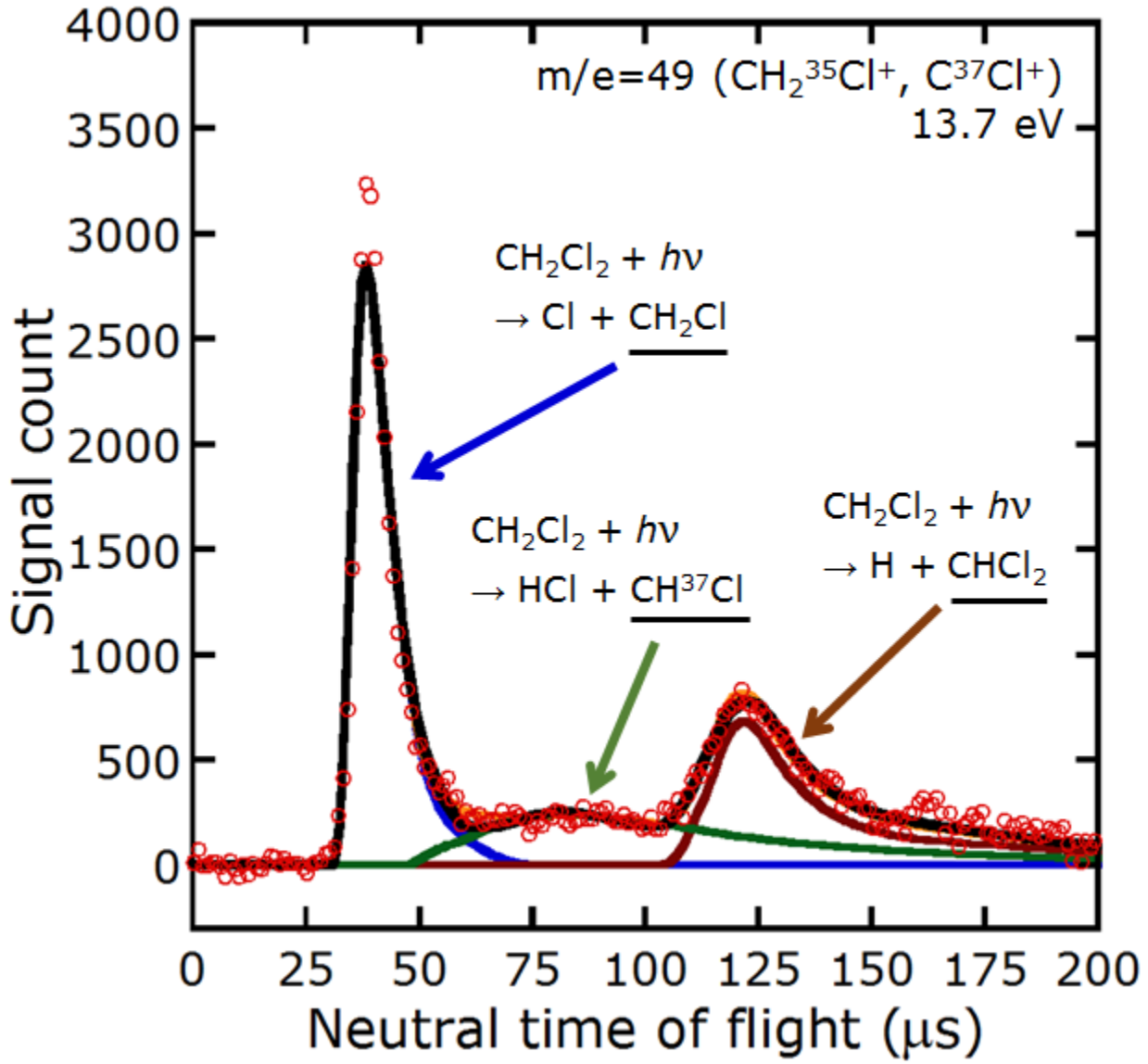

Figure 3.3. Time-of-flight data collected at *m/e*=49 ($CH_2{}^{35}Cl^+$, $C^{37}Cl^+$). The solid blue curve peaking near 40 μs represents the arrival of CH_2Cl fragments formed in the primary C–Cl photofission event, which are cofragments to the primary Cl fragments giving signal in Figure 3.2. The late signal peaking near 125 μs is fitted as dissociative ionization of $CHCl_2$ fragments formed by primary H loss; the $P(E_T)$ of this photodissociation is shown in Figure 3.8. The underlying signal (green curve) arises from secondary dissociation of vibrationally hot $CH^{37}Cl$ to $C^{37}Cl^+$.

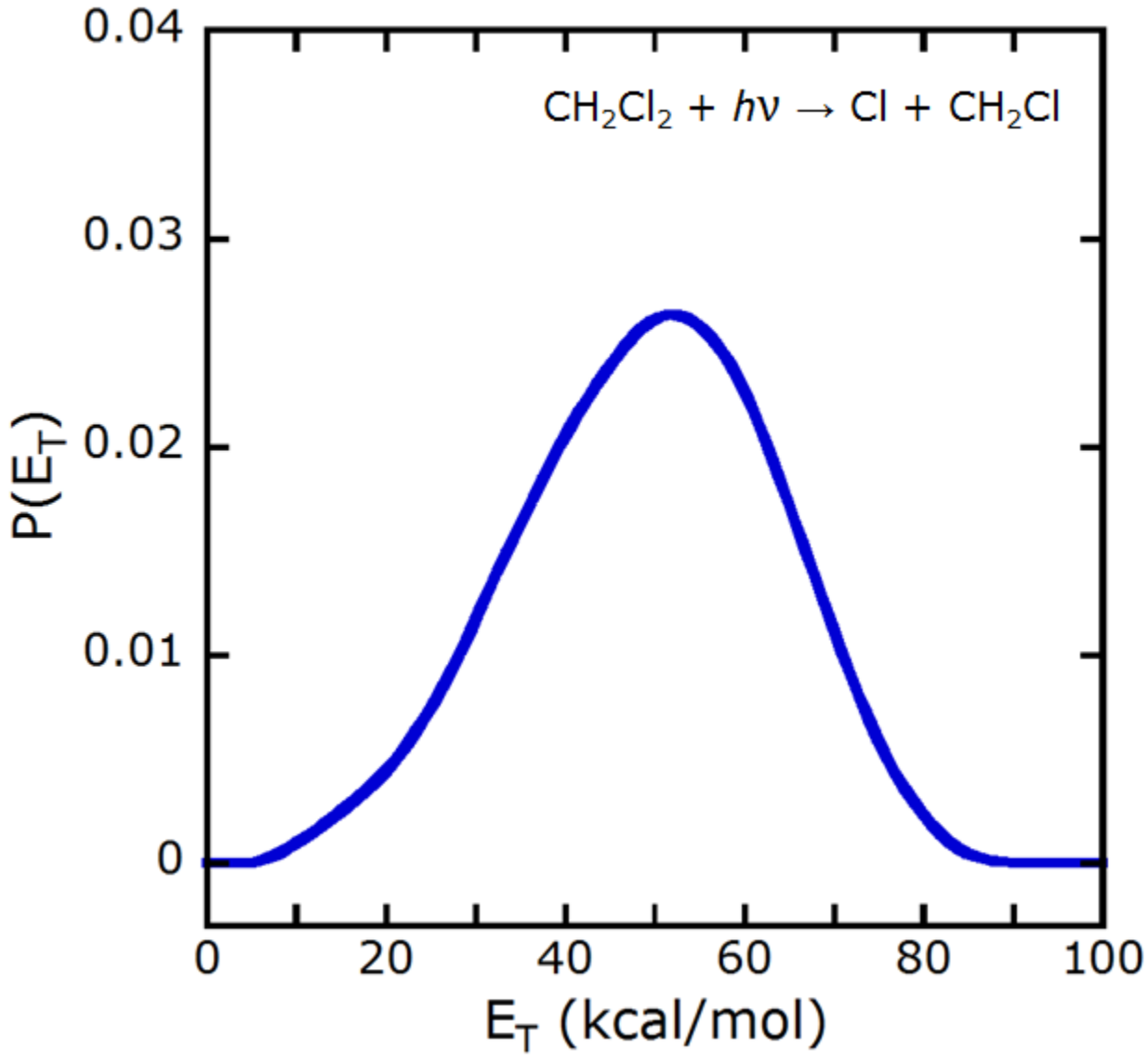

Figure 3.4. The recoil kinetic energy distribution of the C-Cl photofission event, derived from a forward convolution fit to the corresponding signal from Cl atoms and CH_2Cl photoproducts. The resulting fit to the data is shown in blue line in Figures 3.2 and 3.3.

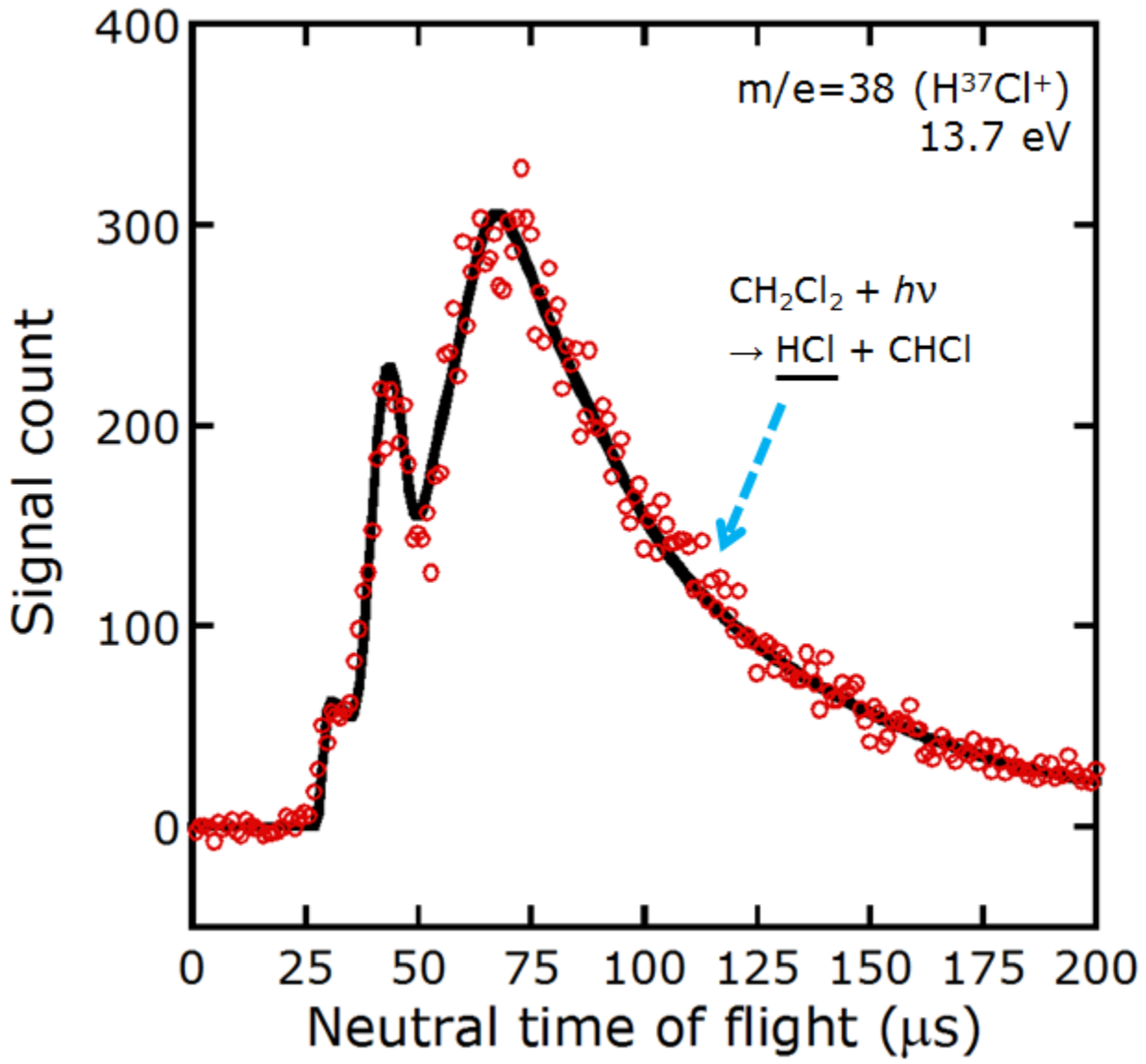

Figure 3.5. Time-of-flight spectrum of ions of *m/e*=38 ($H^{37}Cl^+$). All of this signal is fitted as arising from primary HCl photoelimination from CH_2Cl_2. The trimodal character of the TOF distribution, and of the corresponding P(E_T) in Figure 3.6, are discussed in the text.

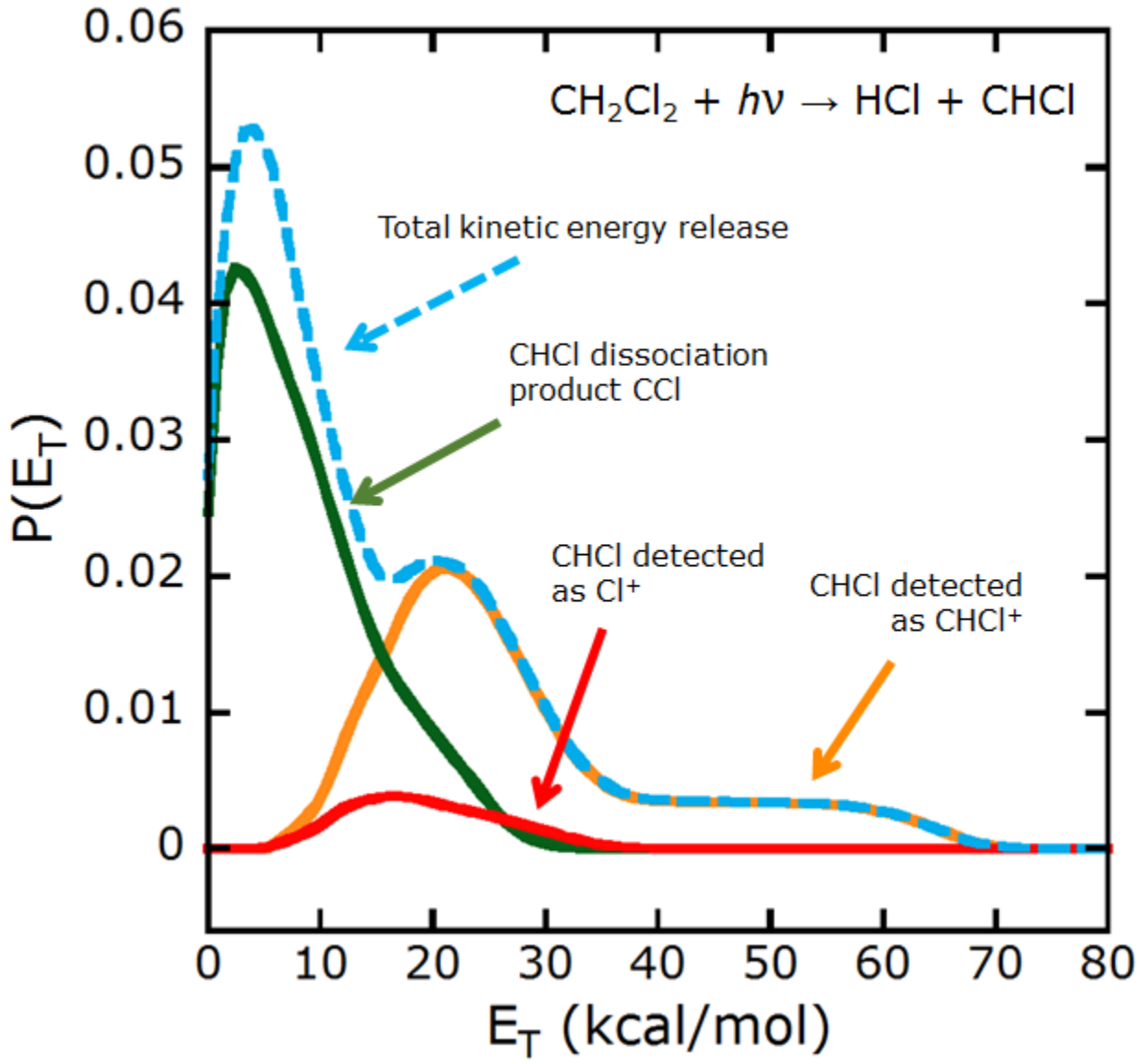

Figure 3.6. Recoil kinetic energy distribution of the primary photoelimination event $CH_2Cl_2 + h\nu \rightarrow HCl + CHCl$. The total distribution, fitted using the *m/e*=38 (HCl^+) data of Figure 3.5, is shown as a dashed blue line. This total distribution is divided into a contribution that produces CHCl fragments that are not stable to vibrational dissociation (green curve), a contribution that produces hot CHCl fragments that are stable but undergo dissociative ionization (red curve), and a contribution that produces cold CHCl fragments that are only detected at parent ion (orange curve). The separation of the total $P(E_T)$ in this manner is described in the text.

induces a complex manifold of excited states near 157 nm; the portion of the P(E_T) representing high kinetic energy release suggests that some HCl photoelimination occurs on an excited-state pathway with a steep exit channel, while the low-kinetic-energy portion suggests internal conversion to other states where the dynamics imparts less energy to relative kinetic energy. One possibility is that a frustrated C-Cl bond dissociation on the new state leads instead to HCl elimination.

The cofragment of primary HCl photoelimination is CHCl. Production of this fragment is evidenced by the data of Figure 3.7 at *m/e*=48 ($CH^{35}Cl^+$), Figure 3.3 at *m/e*=49 ($C^{37}Cl^+$), and Figure 3.2 at *m/e*=35 ($^{35}Cl^+$); ions of *m/e*=47 ($C^{35}Cl^+$) were also observed, but for the sake of brevity those data are shown in Appendix B rather than in this chapter. Notably, the total kinetic energy distribution of the HCl photoelimination channel, which is shown in Figure 3.6 and derived from the TOF data at *m/e*=38 of Figure 3.5, does not describe the observed kinetic energy distribution of CHCl or its daughter fragments. The reason for this seeming discrepancy is as follows. The energy diagram of Figure 3.1 shows that vibrationally hot CHCl undergoes secondary dissociation, so CHCl fragments with vibrational energy above the dissociation threshold of 77.4 kcal/mol are unstable to secondary dissociation and thus cannot be dissociatively ionized to Cl^+. (The CCl product cannot be detected as Cl^+ either, because the appearance threshold of Cl^+ from CCl is 17.1 eV, far higher than the 13.7 eV energy used at m/e=35.) Only those CHCl fragments with vibrational energy just *below* the dissociation threshold may dissociatively ionize to Cl^+: the adiabatic endoergicity of dissociative ionization is 16.9 eV, so CHCl fragments with more than ~3 eV of vibrational energy (69.2 kcal/mol) could be ionized by the 13.7 eV synchrotron radiation, due to its large bandwidth (~4.2% full width at half maximum). In addition, all CHCl fragments with vibrational energy below the dissociation

threshold can be ionized to, and detected as, $CHCl^+$. Thus, detection of CHCl depends strongly on the partitioning of energy into vibration of CHCl, and therefore on the kinetic energy release of the photoelimination event. Only a portion of the total photoelimination kinetic energy distribution will give rise to CHCl that is sufficiently hot to be dissociatively ionized, and a different portion will likewise give rise to CHCl that is sufficiently cold to be ionized but not dissociatively ionized.

The total HCl photoelimination P(E_T) is divided into portions by separately fitting the data at *m/e*=35 (Cl^+, Figure 3.2), *m/e*=49 ($C^{37}Cl^+$, Figure 3.3), and *m/e*=48 ($CH^{35}Cl$, Figure 3.7). The kinetic energy distributions leading to different behaviors of the CHCl photofragments are plotted underneath the main blue curve in Figure 3.6. The lowest E_Ts (described by the green curve) produce hot CHCl fragments that undergo H-loss and give signal as CCl^+. Slightly higher E_Ts (red curve peaking near 18 kcal/mol) produce CHCl fragments with energy near the dissociation threshold, which are dissociatively ionized and detected as Cl^+. The remainder of the distribution (orange curve peaking near 25 kcal/mol and extending to 70 kcal/mol) produces CHCl that undergoes neither dissociation nor dissociative ionization, and is detected as $CHCl^+$.

By partitioning the total photoelimination P(E_T) in this manner, the data at *m/e*=48 ($CH^{35}Cl^+$), shown in Figure 3.7, are easily fitted. In the figure, the TOF signal that is fit with a solid orange line arises from those CHCl fragments that are stable to secondary dissociation and are detected as $CHCl^+$. The portion of the HCl elimination P(E_T) leading to this TOF distribution is the solid orange curve in Figure 3.6. The rest of the signal at *m/e*=48 arises mostly from spurious detection of ions of mass 49, namely $CH_2{}^{35}Cl^+$ and $C^{37}Cl^+$. The solid blue curve in Figure 3.7 shows the TOF distribution of primary $CH_2{}^{35}Cl^+$ ions, as in the data at *m/e*=49 of Figure 3.3. The solid green curve is also seen in the data at both *m/e*=48 and *m/e*=49; and

because the relative height of the blue and green curves is the same in both figures, it is reasonable to conclude that the TOF distribution fitted by the green curve does not arise from *m/e*=48 $CH^{35}Cl$, but rather represents the result of the low quadrupole resolution, so ionization of $C^{37}Cl$ formed by secondary dissociation of vibrationally hot $CH^{37}Cl$ to H + $C^{37}Cl$ contributes to the *m/e*=48 spectrum.

3.3.4. Minor channels: H + $CHCl_2$ and Cl_2 + CH_2

In the data of Figures 3.3 and 3.7 (at *m/e*=49 and *m/e*=48 respectively), some signal is observed at long flight times. We have fitted this signal as arising from dissociative ionization of $CHCl_2$ formed by the primary photodissociation $CH_2Cl_2 + h\nu \rightarrow H + CHCl_2$. The P($E_T$) of this dissociation is shown in Figure 3.8. The appearance of this channel is consistent with an observation by Lin et al. that CH_3Cl also undergoes H-loss when photoexcited at 157 nm; indeed, our P(E_T) for H-loss from CH_2Cl_2 bears a remarkable similarity to their P(E_T) for H-loss from CH_3Cl.[10]

A small signal was detected at *m/e*=70 ($^{35}Cl_2^+$) and at *m/e*=14 (CH_2^+). Some of the ions at these masses can be momentum-matched, indicating that a primary photoelimination channel producing Cl_2 + CH_2 does occur. Moreover, some of the CH_2 signal can be fitted as arising from secondary photodissociation of nascent CH_2Cl radicals. However, the intensity of the signal is so weak that these are clearly minor phenomena, vastly overshadowed by C−Cl photofission and HCl photoelimination. For completeness, we provide the data at *m/e*=70 and *m/e*=14 in Appendix B.

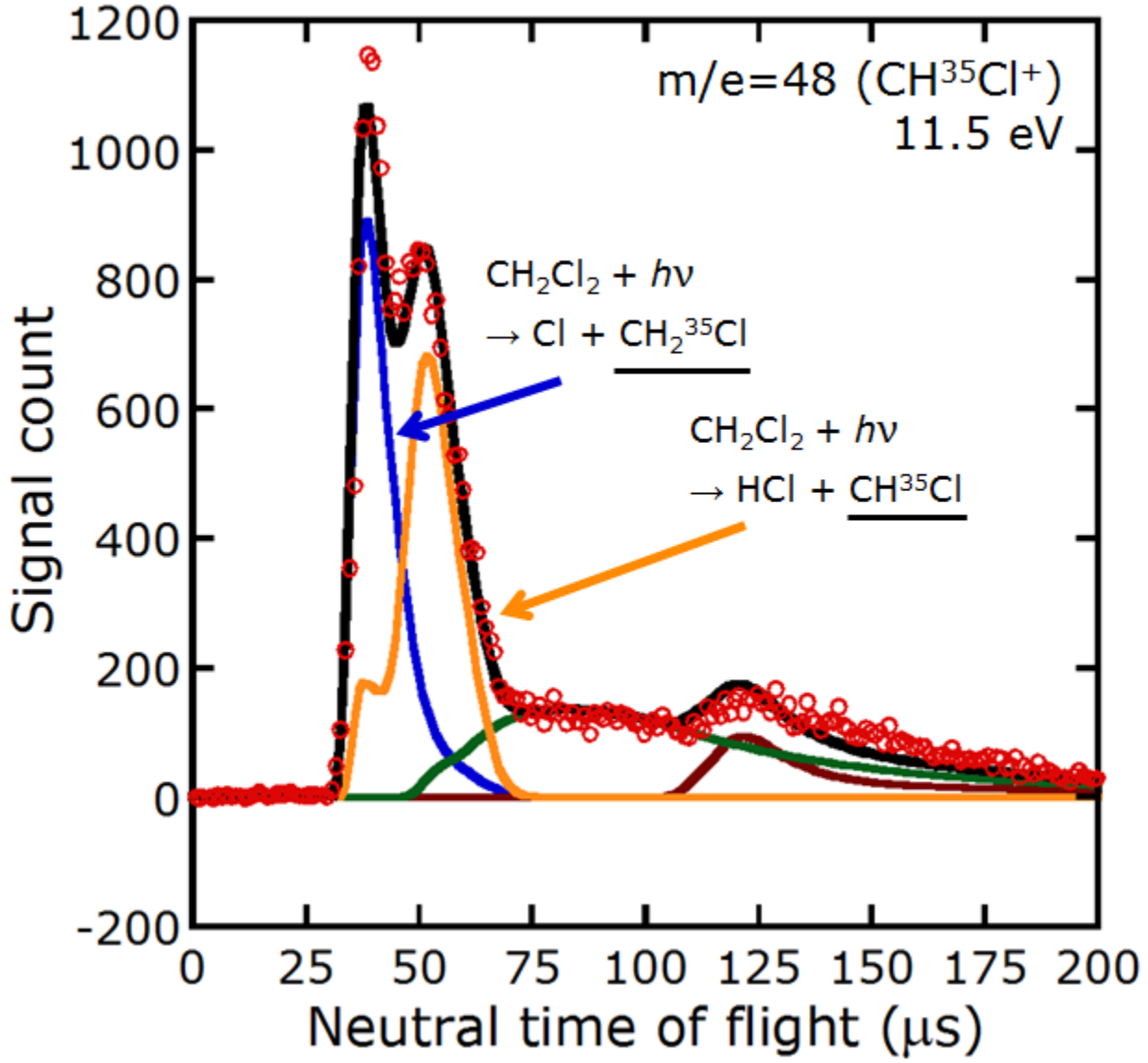

Figure 3.7. Time-of-flight distribution of fragments whose ions were observed at a nominal quadrupole setting of *m/e*=48 ($CH^{35}Cl^{+}$). The signal at *m/e*=49, seen in Figure 3.3, is also present here (blue, green, and dark red line fits), due to the low resolution of the mass filter. The orange curve represents the fitted TOF distribution of primary $CH^{35}Cl$ fragments that are stable to both vibrational dissociation and dissociative ionization, as described in the text.

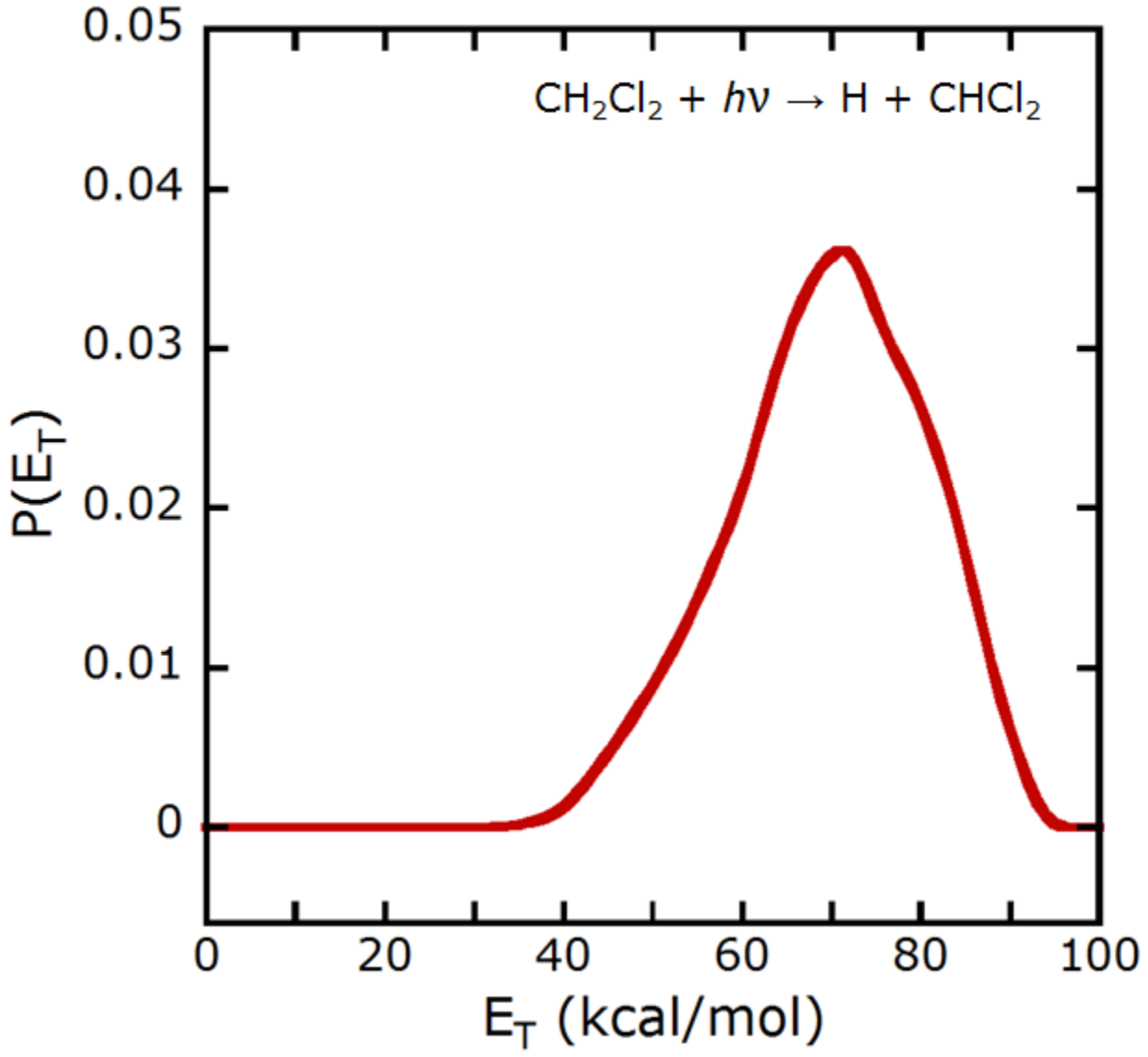

Figure 3.8. Recoil kinetic energy distribution of the primary photodissociation event $CH_2Cl_2 + h\nu \rightarrow H + CHCl_2$. The $CHCl_2$ product appears as its daughter ion, $C^{37}Cl^+$, in the TOF data at m/e=49 and m/e=48 shown in Figures 3.3 and 3.7. The adiabatic appearance threshold of CCl^+ from $CHCl_2$ is calculated to be 11.4 at the G4 level of theory, so this dissociative ionization is accessible at both the 13.7 eV energy used for the m/e=49 data, and the 11.5 eV energy used for the m/e=48 data. In the figures, the contribution of $CHCl_2$ is plotted as a dark red curve.

3.3.5. Assessing the quality of the forward convolution fits

The accuracy of our measured photoionization cross section of CH_2Cl to CH_2Cl^+ at 13.7 eV (described in the next section) depends on the accuracy of our forward convolution fits to the data. Therefore, we should take care to account for any apparent disagreements between our fits and the data.

For determining the photoionization cross section of CH_2Cl, the most important fits are those for the primary photodissociation channel, plotted as solid blue curves in Figures 3.2 and 3.3. In support of this fit, we can confidently assert that there is no physically reasonable mechanism, other than primary C−Cl bond photofission, that can give rise to either the leading edge of the data at low flight times or the sharp peak. These two features can only be fitted as shown in Figures 3.2 and 3.3. The ion signal at slightly longer flight times, just beyond the peak, is also fitted unambiguously by considering the *m/e*=49 data of Figure 3.3. The only possible sources of signal (aside from H-loss signal at long flight times) are $CH_2{}^{35}Cl^+$ (*m/e*=49), arising from C−Cl bond photofission, and $CH^{37}Cl^+$ (*m/e*=50), arising from HCl photoelimination. However, the HCl data of Figure 3.5 cannot support the existence of a nontrivial number of $CH^{37}Cl$ fragments with neutral flight times below ~45 μs. Therefore, the fit shown here is necessary at most flight times longer than the peak time as well. Effectively, the P(E_T) of primary C−Cl photofission shown in Figure 3.4 is unambiguously assigned for E_T > ~24 kcal/mol. In terms of integrated ion signal, less than 10% of the ion signal attributed to C−Cl photofission could conceivably arise from other sources instead.

Assessing the rest of the data is less straightforward. The fit to the HCl data of Figure 3.5 is unremarkable, aside from the interesting trimodal P(E_T) described in Section 3.C. Other conceivable channels that could produce HCl include photodissociation of any of the CH_xCl_y

radical photofragments, and dissociative ionization of very hot CH_2Cl photofragments. Photodissociation of radicals is unlikely because the observed signal scales linearly with laser power. Dissociative ionization of CH_2Cl could occur only in a tiny fraction of all C−Cl photofission events.

The most uncertain part of this analysis is the TOF distributions of the different behaviors of the CHCl fragments, represented by the red, green, and orange curves in Figures 3.2, 3.3, and 3.7. The TOF distributions of these CHCl fragments overlap one another, as well as the TOF distributions of Cl and CH_2Cl, so the fits describing CHCl will affect the measured value of σ_{CH_2Cl/CH_2Cl^+}. Importantly, however, the total HCl photoelimination P(E_T) is fixed and unambiguous, and the various P(E_T)s describing CHCl are derived from the total P(E_T) based on both the fit to the data and conservation of energy. As a result, there is little ambiguity or freedom in the assignment of the P(E_T)s where they overlap the primary Cl and CH_2Cl data, and only small adjustments would be permissible without either violating conservation of energy or considerably worsening the fit. Thus the C−Cl bond photofission P(E_T), and the measured value of σ_{CH_2Cl/CH_2Cl^+}, cannot be considerably different from what we determine in the next section.

3.3.6. Determining the photoionization cross section of CH_2Cl

The data show that photodissociation of CH_2Cl_2 produces Cl and CH_2Cl; the time-of-flight (TOF) distributions of these fragments are fitted by the solid blue curve in Figures 3.2 and 3.3. The integral under each curve is the total integrated ion signal due to this photodissociation channel. The ratio of integrated signals is related to the total number of neutral fragments, as well as several other factors, in the following way:

$$\frac{S_{\mathrm{Cl/Cl^+}}}{S_{\mathrm{CH_2Cl/CH_2Cl^+}}} = \frac{N_{\mathrm{Cl}}}{N_{\mathrm{CH_2Cl}}} \cdot \frac{\sigma_{\mathrm{Cl/Cl^+}}}{\sigma_{\mathrm{CH_2Cl/CH_2Cl^+}}} \cdot \frac{f_{35}{}_{\mathrm{Cl/Cl}}}{f_{35}{}_{\mathrm{Cl/Cl}}} \cdot \frac{TS_{\mathrm{Cl}}}{TS_{\mathrm{CH_2Cl}}} \tag{5}$$

Subscripts indicate the identity of the neutral fragment and its corresponding ion. Here *S* is the integrated ion signal, *N* is the total number of neutral fragments produced, σ is the (partial) photoionization cross section, and *f* is the isotopic abundance. Only a fraction of each type of neutral fragment will enter the detector, and of those that do, fragments with lower speeds have a greater chance of being ionized; to correct this kinematic bias, the "theoretical signal" terms *TS* are introduced, which are the ion signal that would be obtained in the case where $N = 1$, $\sigma = 1$, $f = 1$. Forward convolution fitting software provides the *TS* values. We use this expression and the data in this paper to calculate $\sigma_{\mathrm{CH_2Cl/CH_2Cl^+}}$.

We first note that $N_{\mathrm{Cl}}/N_{\mathrm{CH_2Cl}} \approx 1$. The photodissociation event produces Cl and CH_2Cl as co-fragments, so there is certainly a 1-to-1 ratio of these fragments after photodissociation. It is possible in an experiment like this for some of the CH_2Cl to undergo vibrational dissociation, or secondary photodissociation, which would effectively reduce $N_{\mathrm{CH_2Cl}}$. In this experiment, vibrational dissociation of CH_2Cl is exceptionally unlikely due to the high endoergicity (94 kcal/mol) of this process; indeed, whenever the photochemical kinetic energy release is greater than ~10 kcal/mol, secondary dissociation is forbidden by conservation of energy. On the other hand, secondary photodissociation must occur to some extent, and there is evidence of a photodissociation process, namely $CH_2Cl + h\nu \rightarrow CH_2 + Cl$, in the appearance of a very small shoulder (not fitted here) near 23 μs in the *m/e*=35 TOF data of Figure 3.2. The data imply that secondary photodissociation is a rare event, and so does not appreciably reduce the number of CH_2Cl fragments.

Next we must calculate $\sigma_{\mathrm{Cl/Cl^+}}$ under these experimental conditions. The ionizing

radiation in this experiment is not monochromatic, but rather has an energy distribution of approximately 4.2% full-width-half-maximum. Thus, in this experiment the effective photoionization cross section of atomic chlorine is equal to a weighted average of chlorine's cross section across the bandwidth of the radiation. Using the cross section data of Ruscic and Berkowitz,[5-7] we find that σ_{Cl/Cl^+} = 22.8 Mb in this experiment.

Finally, the ratio of isotopic abundances is clearly 1; the *S* terms are obtained by integration of the TOF distributions indicated by solid blue curves in the figures; and the *TS* terms are provided by kinematic software[10] based on the P(E_T)s and the geometry of the instrument. This leaves only the σ_{CH_2Cl/CH_2Cl^+} term unknown. We note in passing that it is not necessary to include a term correcting for the number of photolysis laser shots or possible drifts in laser power, because the data at *m/e*=35 and *m/e*=49 were collected in brief, alternating sets, with the same number of laser shots making up each set.

Combining all of these terms,

$$\frac{19499}{34687} = \frac{1}{1} \cdot \frac{22.8\ \text{Mb}}{\sigma_{CH_2Cl/CH_2Cl^+}} \cdot \frac{1}{1} \cdot \frac{18259}{27835} \ , \qquad (6)$$

we find that σ_{CH_2Cl/CH_2Cl^+} = 26.6 Mb at 13.7 eV based on our data. Importantly, this value is implicitly integrated over the bandwidth of the synchrotron radiation; the "monochromatic" photoionization cross section may differ. The key source of uncertainty in this Figure 3.is the quality of the forward convolution fits, as described above in Section 3.E. Briefly, adjusting the fits can change the values of *S* and *TS* by a few percent. Another possible source of error is the fact that the CH_2Cl fragments formed in this experiment are vibrationally hot; therefore, the observed photoionization cross section may differ from that of cold CH_2Cl.

3.4. Conclusion

Dichloromethane photolyzed at 157 nm undergoes C−Cl bond photofission and HCl photoelimination, with an additional small amount of H-loss and Cl_2 photoelimination. The kinetic energy release of the photodissociation channels, as characterized by forward convolution fitting, is consistent with that of the same channel in other chloro- compounds photoexcited at 157 nm. Based on the kinetic energy release of the C−Cl photofission channel, practically all of the nascent CH_2Cl fragments are stable to secondary dissociation. By comparing the integrated ion signal at *m/e*=35 and *m/e*=49, the absolute partial photoionization cross section of CH_2Cl to *me*=49 is determined to be 26.6 Mb at 13.7 eV. Due to the nature of the experiment, it is difficult to place an error bar on this figure; however, given the natural uncertainty in our forward convolution fits alone, we would estimate an uncertainty of at about 10% in this measured cross section. In the companion paper on the photodissociation of 2-chloroacetaldehyde by Adams et al.,[14] the relative photoionization cross sections of Cl to Cl^+ and CH_2Cl to CH_2Cl^+ allowed us to quantify the product branching ratio between two of the primary photodissociation channels at 157 nm, Cl + vinoxy and HCO + CH_2Cl. This demonstrates how important partial photoionization cross sections of radical species are in quantifying the product branching in photodissociation and kinetics experiments.

3.5. References

1. Wayne, R. P. *Chemistry of Atmospheres*. 3rd ed.; Oxford University Press: Oxford, U.K., 2000.

2. Finlayson-Pitts, B. J.; Pitts, J. N. *Chemistry of the Upper and Lower Atmosphere: Theory,*

Experiments, and Applications. Academic: New York, 1999.

3. Tsang, W. Mechanisms for the formation and destruction of chlorinated organic products of incomplete combustion. *Combust. Sci. Technol.* **1990**, *74*, 99-116.

4. Taatjes, C. A.; Osborn, D. L.; Selby, T. M.; Meloni, G.; Fan, H.; Pratt, S. T. Absolute Photoionization Cross-Section of the Methyl Radical. *J. Phys. Chem. A* **2008**, *112*, 9336-9343.

5. FitzPatrick, B. L.; Maienschein-Cline, M.; Butler, L. J.; Lee, S.-H.; Lin, J. J. Determining the Partial Photoionization Cross-Sections of Ethyl Radicals. *J. Phys. Chem. A* **2007**, *111*, 12417-12422.

6. Ruscic, B.; Berkowitz, J. Photoionization of Atomic Chlorine. *Phys. Rev. Lett.* **1983**, *50*, 675.

7. Berkowitz, J. *Atomic and Molecular Photoabsorption: Absolute Total Cross Sections*. Academic: San Diego, California, 2002.

8. Robicheaux, F.; Greene, C. H. Regularities in calculated photoionization cross sections for the halogens. *Phys. Rev. A* **1992**, *46*, 3821-3833.

9. Ratliff, B. J.; Alligood, B. W.; Butler, L. J.; Lee, S.-H.; Lin, J. J.-M. Product Branching from the CH_2CH_2OH Radical Intermediate of the OH + Ethene Reaction. *J. Phys. Chem. A* **2011**, *115*, 9097−9110.

10. Lin, J. J.; Chen, Y.; Lee, Y. Y.; Lee, Y. T.; Yang, X. Photodissociation Dynamics of CH_3Cl at 157.6 nm: Evidence for $CH_2(\tilde{X}^3B_1/\tilde{a}^1A_1)$+HCl Product Channels. *J. Chem. Phys. Lett.* **2002**, *361*, 374−382.

11. Lee, S.-H.; Lee, Y.-Y.; Lee, Y. T.; Yang, X. Photodissociation Dynamics of Propene at 157.6 nm: Kinetic Energy Distributions and Branching Ratios. *J. Chem. Phys.* **2003**, *119*, 827−838.

12. CMLAB2, version 6/93, modified by J. D. Myers. This is an interactive version built on the original cmlab2 program: Zhao, X. Ph.D. Dissertation, University of California, 1988.

13. Frisch, M. J.; Trucks, G. W.; Schlegel, H. B.; et al. Gaussian 09, Revision A.02; Gaussian, Inc: Wallingford, CT, 2009.

14. Adams, J. D.; Scrape, P. G.; Li, S.; Lee, S.-H.; Butler, L. J. Dissociative Photoionization of the Elusive Vinoxy Radical. Submitted.

CHAPTER 4

A NEW FRANCK-CONDON APPROACH TO ESTIMATING ENERGY PARTITIONING IN DIATOMIC ELIMINATION PATHWAYS

Part of this work was previously published in Lee, P.-W.; Scrape, P. G.; Butler, L. J.; Lee, Y.-P., *J. Phys. Chem. A* **2015**, *119*, 7293-7304, copyright 2015 American Chemical Society. Reproduced with permission. The analysis has been modified slightly: in the published version the IRCs are treated as discrete, while here they are fitted to a continuous function. The criteria for selecting a point along the IRC for use in the Franck-Condon approximation have been refined in light of the continuous IRCs. These modifications change some numeric results, but do not affect the conclusions of the study.

4.1. Introduction

The partitioning of energy during a molecular dissociation into translations, rotations, and vibrations of the products is a key dynamical phenomenon that reflects the elementary quantum-chemical processes underlying chemical reactivity. However, there is currently no theoretical model that reliably estimates how the available energy will be partitioned. For dissociation channels with no exit barrier and in which the dissociating species is thermalized and has negligible angular momentum, statistical theories generally suffice to describe the partitioning.[1,2] All other cases require more elaborate approaches. Some impulse models attempt with mixed success to relate the internal energy of the daughter fragments to parameters such as the experimentally observed translational energy release,[3] or the calculated displacement vectors of the transition state.[4] Trajectory studies on calculated potential energy surfaces (whether of the quasiclassical or

ab initio flavor) are often quite successful, but require significant computing power to perform.[5]

This chapter describes a new model that estimates the vibrational energy of a departing diatomic fragment in a dissociation with finite exit barrier. The model is described in detail in Section 4.2. The only input required by the model is a calculated intrinsic reaction coordinate (IRC) surface; thus, it has the advantages of being computationally efficient, general in scope, and free of empirical parameters. Its key assumption is that the nascent daughter fragments cease to interact at a certain point, *beyond the transition state*, on the dissociation pathway; thus, following a quasi-Franck-Condon approximation, the vibrational excitation of the diatomic fragment can be inferred from the distance between the two atoms at the point of non-interaction.

The experimental system described by the model in this chapter is the photodissociation of gas-phase acryloyl chloride, $CH_2CHC(O)Cl$, at 193 nm. This species exhibits rich photochemistry due to its enone (C=C-C=O) group and chloride moiety; one product channel at this wavelength is HCl photoelimination. In the experimental study, Lee et al. employed step-scan Fourier transform infrared (FTIR) spectroscopy to detect emission of the HCl products.[6] Their data revealed that there are two distinct HCl photoelimination channels: the major channel, with a branching fraction of 0.80 ± 0.15, produces rotationally and vibrationally hot HCl ($T_{rot} \approx 5000$ K, $v \leq 7$); the minor channel produces rotationally and vibrationally cold HCl ($T_{rot} \approx 1000$ K, $v \leq 4$). The observed branching fractions were entirely consistent with a ground-state process, wherein the major channel is direct HCl elimination from the hot acryloyl chloride molecule, while the minor channel arises from a 1,3-sigmatropic Cl shift producing 3-chloro-1-propen-1-one ($CH_2ClCHCO$) which then undergoes HCl elimination. Figure 4.1 shows the stationary points along these dissociation pathways. An ancillary result in this chapter, presented in Section 4.3.1, is a determination of the theoretical branching ratio based on these stationary points and RRKM theory; the RRKM

branching ratio is 0.81:0.19, a staggeringly good agreement with the experiment.

Despite the excellent agreement between the experimental and theoretical branching ratios, it is desirable to provide additional support for the hypothesis that the photoelimination is a ground-state process. The model developed in this chapter shows that the major channel on the potential energy surface produces hot HCl in accordance with the experiment, and that the minor channel produces cold HCl.

4.2. Methods

4.2.1. The Franck-Condon post-TS non-interaction model

General principles of the model are described in this section. Section 4.3 discusses an explicit application of the model to the case of acryloyl chloride.

The transition state (TS) of a dissociation is the first-order saddle point on the potential energy surface (PES) from which descent along the PES in one direction leads toward complete dissociation (the "product well"), while descent in the opposite direction leads back to the bound molecular geometry (the "reactant well"). A simple approach to estimating the energy partitioning during dissociation starts by assuming that the two fragments cannot exchange energy within the product well. Under this assumption, at the TS geometry the products are in a sense "fully formed" and the partitioning of energy is complete; further descent into the product well corresponds to relaxation within the nascent fragments, and repulsion between them.

If one of the daughter fragments is a diatomic (denoted A-B), this non-interaction assumption allows the vibrational energy of the diatomic to be calculated in a manner reminiscent of the Franck-Condon principle. Since the A-B molecule is "fully formed" at the transition state, no further vibrational energy can flow into it, and from that point on it must vibrate within its one-

dimensional harmonic well. However, the A-B interatomic distance at the TS (denoted $\boldsymbol{R}_{TS}$) is not in general the equilibrium A-B bond length (denoted $\boldsymbol{R}_{eq}$). Therefore the nascent A-B molecule must possess at least as much vibrational energy as is required for it to vibrate with $\boldsymbol{R}_{TS}$ as a classical turning point, in the same sense that a stretched spring must possess at least as much energy as is required to stretch it.

The obvious deficiency of this simple analysis is the non-interaction assumption, since it is intuitively clear that energy *can* continue to flow during the descent into the product well. It is equally clear, however, that energy flow must eventually become negligible, as the two products must eventually become independent. Thus the simple approach can be improved considerably by identifying the true point of non-interaction along the dissociation trajectory. Dissociation in fact occurs along infinitely many trajectories. However, the intrinsic reaction coordinate (IRC), a one-dimensional subsurface of the complete PES connecting the TS to the reactant and product wells via a steepest-descent path, serves in some sense as a representative or most-probable trajectory.

The new Franck-Condon model described here assumes that a geometry along the IRC, rather than the TS, should be taken as the point of non-interaction. Under this assumption, the dissociation trajectory has a "transition-state region" after the saddle point, in which the two nascent fragments cannot recombine yet continue to exchange energy. The end of this transition-state region along the IRC marks the geometry at which energy exchange ceases. If one of the daughter fragments is a diatomic, the vibrational excitation of the diatomic may be calculated from the interatomic distance of the diatomic at the end of the transition-state region. The example of acryloyl chloride in Section 4.3 is representative.

Since the end of the TS region is a point where energy exchange ceases and where repulsion and relaxation begin, the endpoint must be characterized by an abrupt change in the curvature of

the potential energy surface and in the motion of the atoms along the IRC. This chapter's description of the model proposes two points that may be taken as the end of the TS region. The first is quite general: the TS region ends at the point where the curvature of the PES changes sharply, indicated by the fact that the second derivative of energy with respect to the reaction coordinate has an inflection point (or equivalently the point where the fourth derivative of energy is zero, i.e., $d^4E/dq^4 = 0$). The second proposed end of the TS region refers specifically to interatomic motion in the elimination of a diatomic. In the dissociation process A–R–R`–B → A–B + R–R`, the atom A must approach the atom B in order to abstract it and form the product A–B. The end of the TS region is the point where A most closely approaches R` along its route to abstract B. After this point of closest approach, atom A departs from R` as part of the fragment A–B; this departure represents the end of energy exchange and the beginning of repulsion and relaxation. In the case of acryloyl chloride presented below, the two hypothesized endpoints give similar results.

4.2.2. Computational methods

Energies of stationary geometries were calculated at the G4//B3LYP/6-311++G(3df,2pd) level of theory, including zero-point correction, using the Gaussian 09 software package.[7] Intrinsic reaction coordinate calculations were performed at the B3LYP/6-311++G(3df,2pd) level of theory, with a reaction coordinate step size of 0.0279 $amu^{1/2}$ bohr, but without zero-point correction. Molecular geometries were rendered using the Molden program.[8]

4.3. Results

4.3.1. Theoretical branching ratio of HCl photoelimination from acryloyl chloride

Two conformers, *s-trans*-$CH_2CHC(O)Cl$ and *s-cis*-$CH_2CHC(O)Cl$, of acryloyl chloride exist, with the former more stable by ~1 kJ mol^{-1} than the latter. Calculations at the G4//B3LYP level show two pathways to eliminate HCl on the S_0 surface of acryloyl chloride. Both yield HCl + $H_2C=C=C=O$, but with very different energetics and dynamics en route. The stationary points for these pathways are shown in Figure 4.1. The major path involves a four-center elimination through the *s-cis* conformer with a barrier ~209 kJ mol^{-1}. The minor path involves a sigmatropic 1,3-Cl shift from the *s-trans* conformer to $CH_2ClCHCO$, with a barrier ~190 kJ mol^{-1}, followed by four-center elimination over a barrier with energy ~238 kJ mol^{-1}.

A theoretical branching ratio between the two HCl photoelimination pathways was determined using RRKM theory, as follows.[9] The competition between the two pathways, involving the three local minima, dissociative transition states, and transition states of isomerization, were modeled as a set of five first-order rate equations: one equation each for the number density as a function of time of each of the three minima and two product pathways. These equations involve six nonzero rate coefficients, namely the forward and reverse coefficients for both the *cis-trans* isomerization and the Cl shift as well as the forward coefficients for two HCl elimination pathways. (The reverse coefficients for HCl elimination, corresponding to a collision of $H_2C=C=C=O$ + HCl leading to recombination, are essentially zero because of the trivial probability of such a collision occurring before the $H_2C=C=C=O$ dissociates further.) These coefficients were determined with RRKM theory. To calculate the sums and densities of states, the semiclassical technique of Whitten Rabinovitch, as implemented in the RRKM software, was

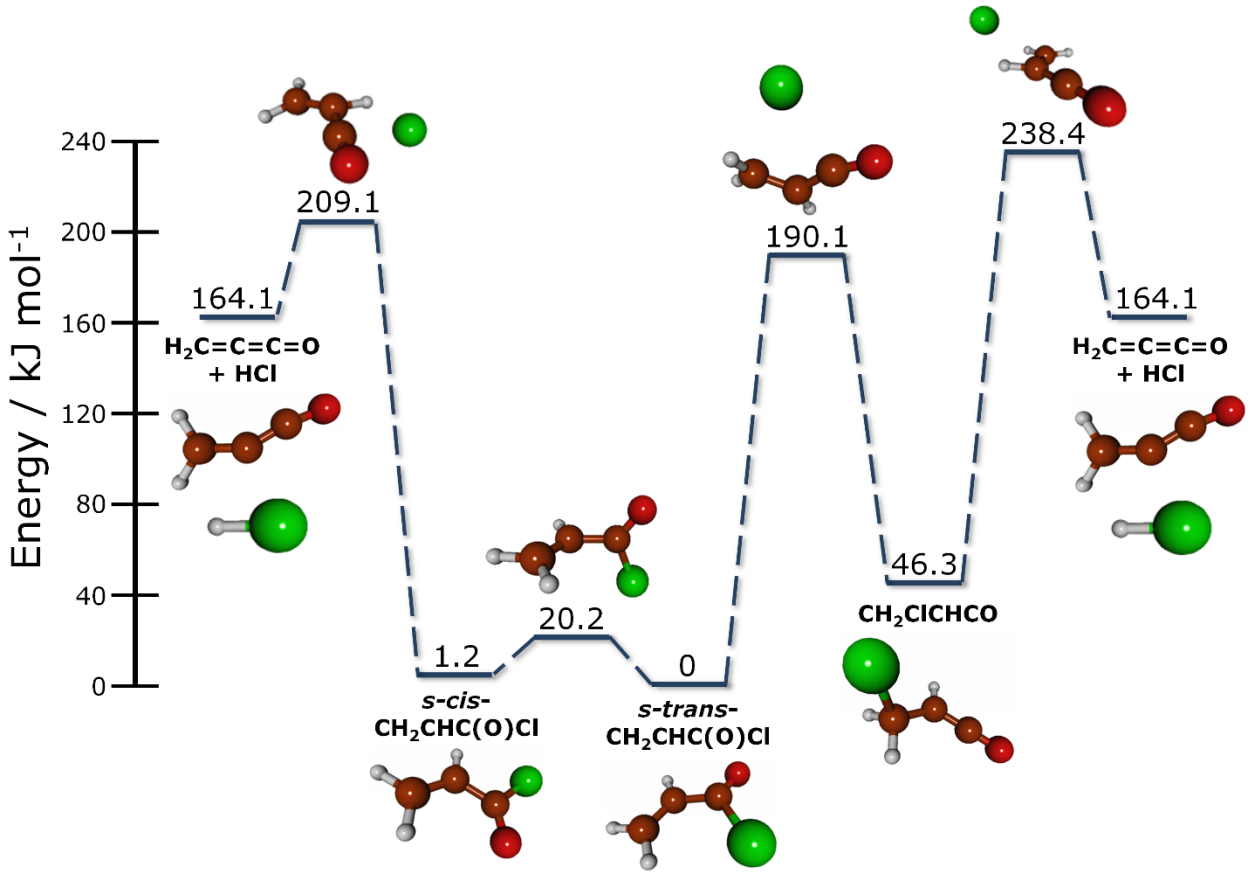

Figure 4.1. Minima and transition states for the two HCl-elimination channels on the S_0 surface of acryloyl chloride. Energies relative to the energy of the *s-trans* conformer are calculated at the G4//B3LYP/6-311++G(3df,2pd) level. All energies include the zero-point vibrational energy.

employed. Direct CO loss from ground-state acryloyl chloride (barriers not shown in Figure 4.1) was also considered in the RRKM analysis; however, the barriers to CO loss were found to be simply too large for CO loss to affect the HCl elimination branching ratio.

The theoretical branching ratio between the two elimination channels was determined as the ratio of the populations in the product asymptote of the two HCl elimination channels in the infinite-time limit. This calculation predicts a statistical branching ratio of 0.81:0.19 for direct HCl elimination from the *s-cis* conformer : HCl elimination from 3-chloro-1-propen-1-one after the Cl shift.

4.3.2. Application of the new Franck-Condon model to acryloyl chloride

The energies along the intrinsic reaction coordinate for the two pathways calculated at the B3LYP level of theory are plotted in Figure 4.2. In the figure, open red diamonds represent elimination from the *s-cis* conformer, filled blue circles represent elimination from the 1,3-Cl shifted intermediate, and energies are given relative to the B3LYP energy of the *s-cis* conformer. The energy along each reaction coordinate has a relatively flat plateau in the vicinity of the transition state, after which the Cl atom approaches the H atom to eliminate HCl. Choosing the correct geometry to predict Franck-Condon factors for the vibrational states of HCl hence required close consideration. Near the mass-weighted displacement along the reaction coordinate of $S \approx 0.5$ on the *s-cis* IRC and $S \approx 2.5$ on the Cl-shifted IRC, indicated by arrows in Figure 4.2, the plateau ends and the energy drops precipitously. The new Franck-Condon model described in Section 4.2.1 associates his sharp change in energy with the formation of the nascent H-Cl bond; thus the H-Cl distance at that point along the reaction coordinate should be used to approximate the vibrational energy imparted to the eliminated HCl.

The coordinate at which the plateau in the IRC ends corresponds to an inflection point in the second derivative of energy; the second and fourth derivatives of energy are plotted in Figure 4.3. For the major *s-cis* elimination channel, the second derivative has its inflection point at $S = 0.48$, with an elimination H–Cl bond length of ~1.69 Å. The Franck-Condon estimate for the HCl vibrational energy using the outer turning point of 1.69 Å gives $v \approx 7$ vibrational quanta. For the minor Cl shift channel, the plateau ends at $S = 2.24$, where the H-Cl distance is ~1.66 Å, equivalent to $v \approx 6$ quanta in the stretch of the HCl product from that pathway. Thus, this new Franck-Condon model correctly predicts that the major *s-cis* elimination channel imparts greater vibrational energy to the HCl fragments than does the minor channel, and also gives a close estimate of the vibrational energy imparted by the two channels.

As mentioned in the description of the model in Section 4.2.1, interatomic distances may also be used as an indicator of the endpoint of the transition-state region. Figure 4.4 shows the interatomic distance between the Cl and central C atom for each pathway plotted as a function of progress along the reaction coordinate. In both cases, the C–Cl separation decreases as the Cl atom approaches to abstract a hydrogen atom. The distance of closest approach in Figure 4.4 represents the point at which the Franck-Condon approximation should be applied, since (by assumption) the H–Cl bond is formed there; beyond the distance of closest approach, the nascent HCl molecule transits away from the propadienone co-fragment. For the *s-cis* elimination channel, the C–Cl distance is minimized at coordinate $S = 0.47$, with an elimination H–Cl bond length of ~1.69 Å, equivalent to $v \approx 7$. For the Cl-shifted channel, the C–Cl distance is minimized at coordinate $S = 2.37$, corresponding to an H–Cl bond length of ~1.61 Å and $v \approx 5$. These results are consistent with choosing the position along the reaction coordinate for the Franck-Condon analysis for H–Cl vibration based on the drop in potential energy along the IRC. This agreement provides confidence

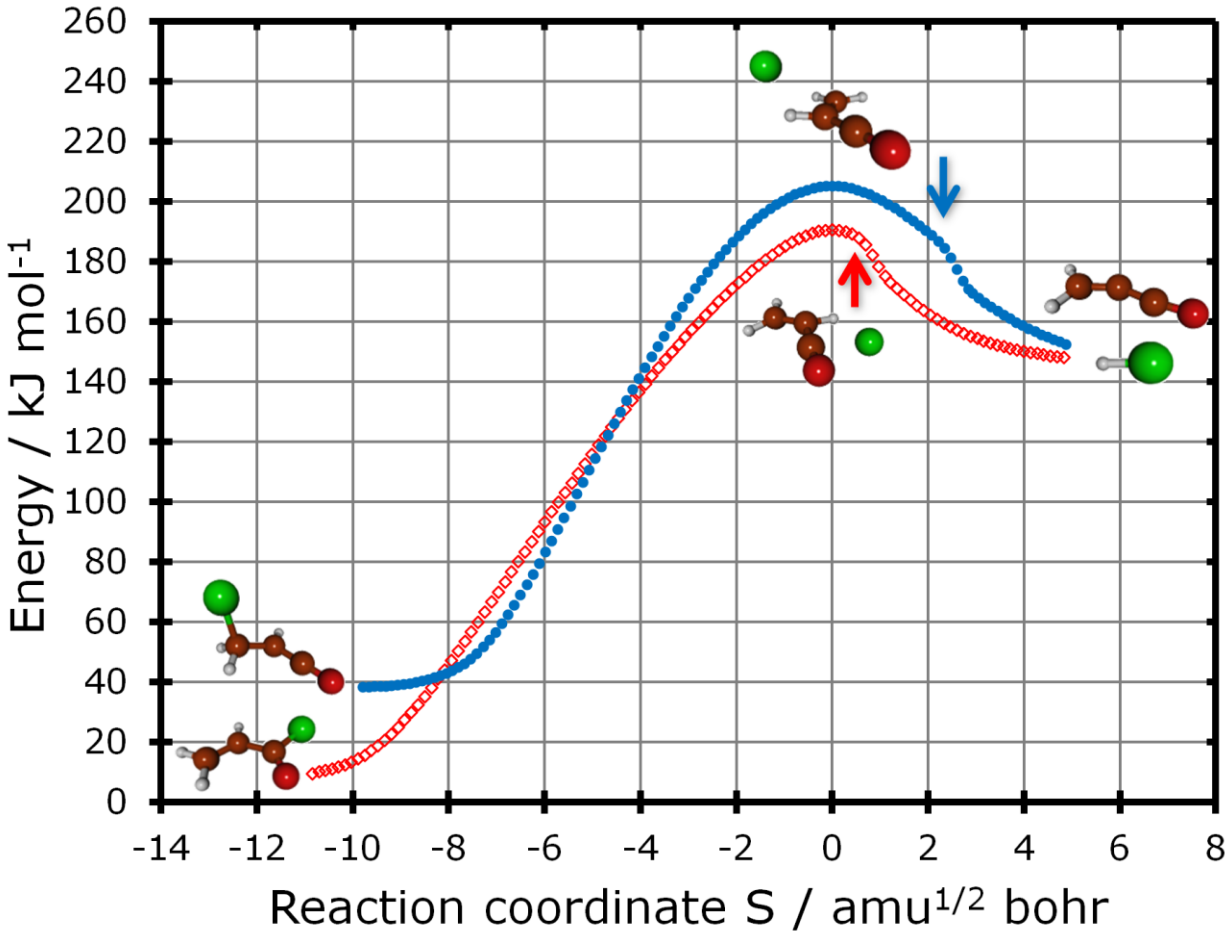

Figure 4.2. Intrinsic reaction coordinate (IRC) calculation for HCl elimination from the 1,3-Cl-shifted (filled blue circles) and *s-cis* (empty red diamonds) isomers. The minimum potential energy of the *s-cis* conformer without zero-point correction is chosen as zero. As IRC points were calculated at the B3LYP/6-311++G(3df,2pd) level, the barrier heights are not identical to the G4 results in Figure 9, even after zero-point correction. The geometry at the kink near $S = 0.5$ for *s-cis* IRC and $S = 2.5$ for the 1,3-Cl-shifted IRC, indicated respectively by red and blue arrows, was used for the Franck-Condon estimate of the amount of vibrational energy in the eliminated HCl molecule, as described in the text.

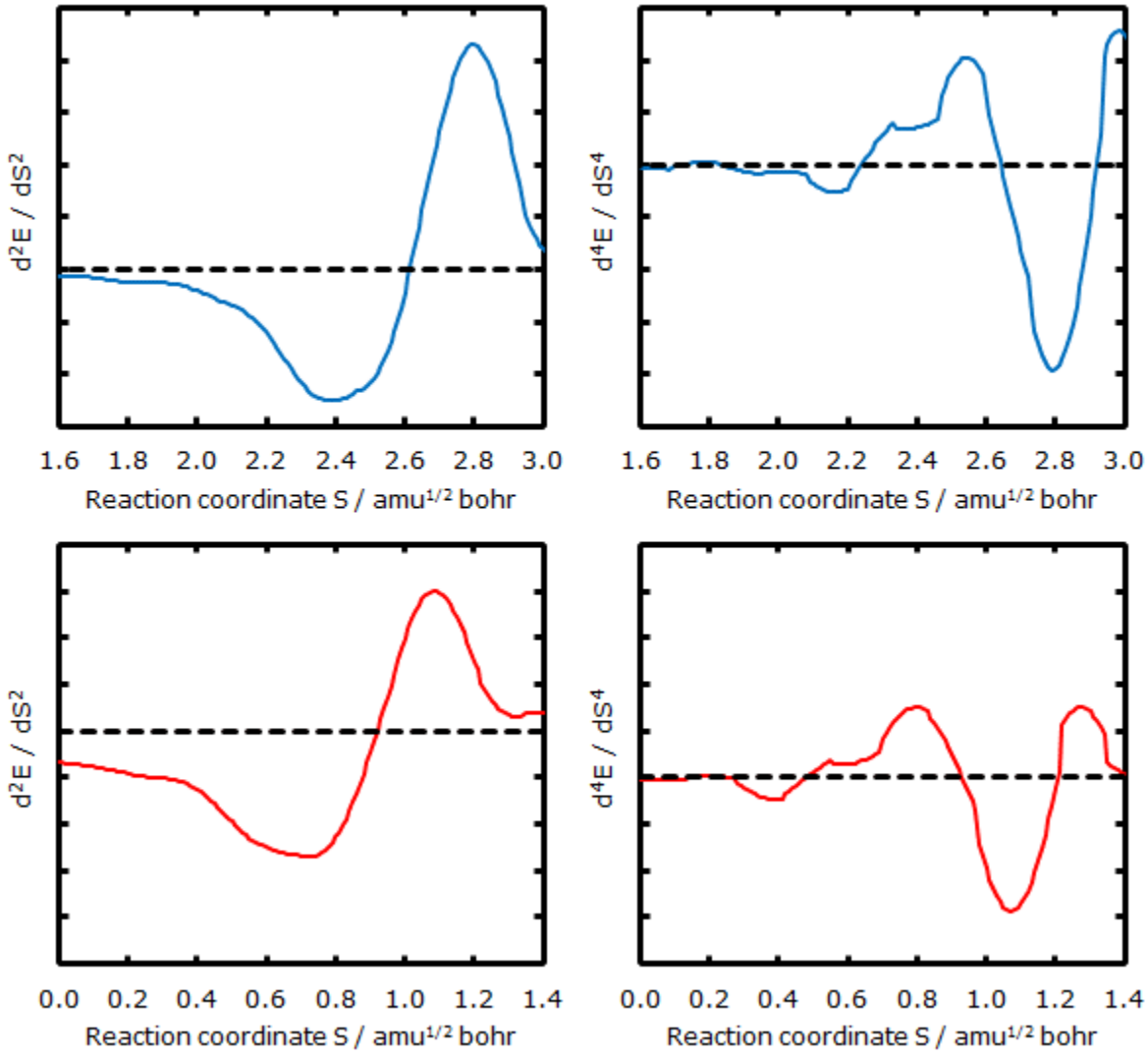

Figure 4.3. Second derivatives (left column) and fourth derivatives (right column) of the IRC leading to HCl elimination from the Cl-shifted (blue line) and *s-cis* (red line) conformers of acryloyl chloride.

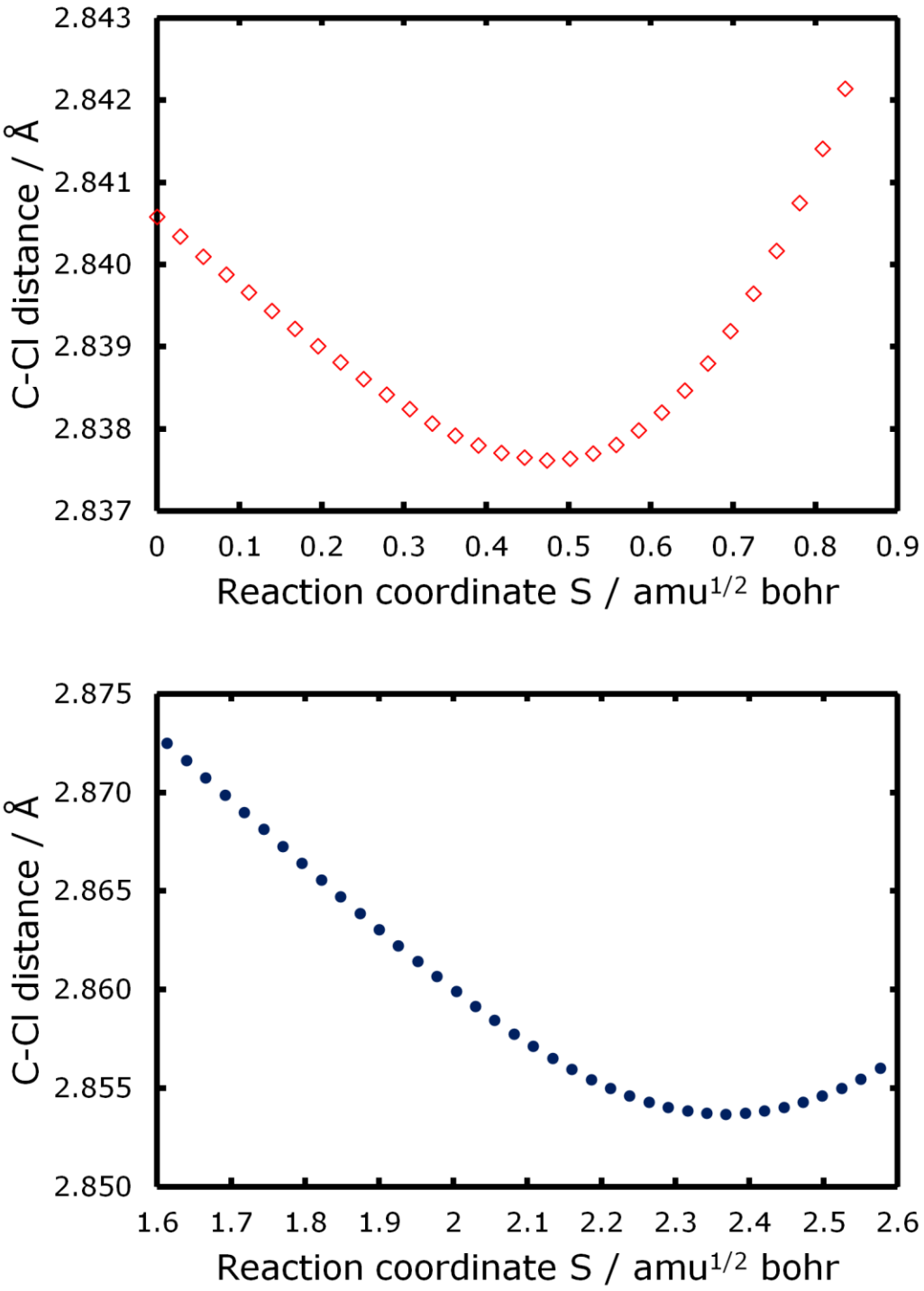

Figure 4.4. Distance between the C and Cl atoms involved in HCl elimination from the *s-cis* conformer (open red diamonds) and the 1,3-Cl-shifted isomer (filled blue circles). The distance of closest approach of the Cl to the C atom identifies the geometry along the IRC to use for the Franck-Condon estimate for the HCl vibrational distribution.

in using these geometries for the Franck-Condon prediction for vibrational energy imparted to the HCl product. This new Franck-Condon method thus appears to be much more reliable than the simpler method of using the geometry at the formal transition state for HCl elimination from the Cl-shifted intermediate. Indeed, in this case the H–Cl bond distance at the formal transition state for the minor pathway is anomalously large, as it is a roaming-like transition state; rather, the Cl atom must approach the CH moiety in the radical again to actually eliminate HCl.

4.4. Conclusion

The theoretical calculations of Section 4.3 predict that two paths exist to eliminate HCl on the S_0 surface of acryloyl chloride: the major path is a four-center elimination through the *s-cis* conformer, and the minor path involves a 1,3-Cl shift from the *s-trans* conformer to $CH_2ClCHCO$, reaction (5), followed by four-center elimination. The statistical prediction for the branching ratio between these two pathways, 0.81 : 0.19, agrees well with the experimental result of 0.80 : 0.20, indicating that the observed major channel is to be associated with elimination from the *s-cis* conformer, and the minor channel with elimination from a 1,3-Cl-shifted geometry.

The calculations also explain the bimodal vibrational distribution of quantum states measured for the HCl product. For the *s-cis* elimination channel, the new Franck-Condon model predicts excitation of $v \approx 7$ in HCl, whereas for the 1,3-Cl shifted channel the model predicts $v \approx 5$. This result agrees qualitatively with the experimental observation of up to $v = 7$ for the major channel and $v = 4$ for the minor channel, reinforcing the identification of the major channel with HCl elimination from the *s-cis* conformer and the minor channel with elimination from the 1,3-Cl-shifted intermediate. Notably, this Franck-Condon analysis does not make the traditional choice of using the H–Cl distance at the formal transition state, as that distance is not meaningful for

reactions characterized by roaming. Rather, the new procedure described here for identifying the correct point along the IRC to generate the Franck-Condon prediction, the point at which the roaming Cl atom has re-approached the C atom to which the H atom is attached, provides a superior prediction.

4.5. References

1. Hunter, M.; Reid, S. A.; Robie, D. C.; Reisler, H. The monoeneretic unimolecular reaction of expansion-cooled NO_2: NO product state distributions at excess energies 0-3000 cm^{-1}. *J. Chem. Phys.* **1993**, *99*, 1093.

2. Wittig, C.; Nadler, I.; Reisler, H.; Noble, M.; Catanzarite, J.; Radhakrishnan, G. Nascent product excitations in unimolecular reactions: the separate statistical ensembles method. *J. Chem. Phys.* **1985**, *83*, 5581.

3. Ratliff, B. J.; Womack, C. C.; Tang, X. N.; Landau, W. M.; Butler, L. J.; Szpunar, D. E. Modeling the Rovibrationally Excited C_2H_4OH Radicals from the Photodissociation of 2-Bromoethanol at 193 nm. *J. Phys. Chem. A* **2010**, *114*, 4934-4945.

4. Lin, S.-R.; Lin, S.-C.; Lee, Y.-C.; Chou, Y.-C.; Chen, I.-C.; Lee, Y.-P. I. Three-center versus four-center HCl-elimination in photolysis of vinyl chloride at 193 nm: Bimodal rotational distribution of HCl ($v \leq 7$) detected with time-resolved Fourier-transform spectroscopy. *J. Chem. Phys.* **2001**, *114*, 160-168.

5. Fu, B.; Zhang, D. H.; Bowman, J. M. Quasiclassical trajectory studies of $^{18}O(^3P) + NO_2$ isotope exchange and reaction to O_2 + NO on D_0 and D_1 potentials. *J. Chem. Phys.* **2013**, *139*, 024303.

6. Lee, P.-W.; Scrape, P. G.; Butler, L. J.; Lee, Y.-P. Two HCl-Elimination Channels and Two CO-Formation Channels Detected with Time-Resolved Infrared Emission upon Photolysis of Acryloyl

Chloride [$CH_2CHC(O)Cl$] at 193 nm. *J. Phys. Chem. A* **2015**, *119*, 7293-7304.

7. M. J. Frisch, G. W. Trucks, H. B. Schlegel et al., GAUSSIAN 09, Revision A.02, Gaussian, Inc., Wallingford, CT, 2009.

8. Schaftenaar, G.; Noordik, J. H. Molden: a Pre- and Post-processing Program for Molecular and Electronic Structures. *J. Comput.-Aided Mol. Design* **2000**, *14*, 123-134.

9. Hase, W. L.; Bunker, D. L. *Quantum Chemistry Program Exchange*, Program No. 234; Indiana University: Bloomington, IN,1974.

CHAPTER 5

HIGH-ACCURACY AB INITIO THERMOCHEMISTRY OF METHYLENE AND THE WATER DIMER

5.1. Introduction

The calculation of chemical bond energies and other thermodynamic properties to sub-kilojoule accuracy is becoming more realistic with the growth of computing power and new developments in electronic structure theory. A recently-developed model chemistry known as "high-accuracy extrapolated *ab initio* thermochemistry", or HEAT, [1-3] formalizes the calculation of total energies for small molecules in a manner that is rigorous, computationally feasible, and free of empirical parameters. The HEAT method has been applied to calculate the formation enthalpy of several molecules containing two to four atoms, as well as larger systems including the allyl radical[4] and benzene,[5] and achieves agreement with the best experiments to within 1 kJ/mol. HEAT has also exhibited excellent accuracy in calculations of the energetic barriers to several bimolecular reactions.[6-8] These results show that HEAT is a promising tool in the study of chemical dynamics as well. The HEAT protocol is described briefly in Section 5.2.

This study applies the HEAT method to two chemical systems: the singlet-triplet gap of methylene and the dissociation energy of the water dimer are calculated and compared to experimental data. These systems pose interesting challenges to electronic structure theory, but the thermodynamic properties are known experimentally with exceptional precision; thus, this study allows a characterization of the successes and (possible) deficiencies of HEAT.

Methylene poses a twofold challenge for quantum chemistry. The singlet, $^1CH_2$, has a two-

configurational wavefunction: in the dominant configuration the HOMO is $(3a_1)^2$, but there is a strong contribution from $(1b_1)^2$ as well. The triplet, $^3CH_2$, is quasilinear: the potential energy surface is nearly flat along the bending mode.[9-13] To correctly calculate the singlet-triplet gap, $T_0(CH_2)$, a model chemistry must treat the electronic structure of the two spin states equally well by accounting for both the multireference $^1CH_2$ (either by assuming the two-configurational state *a priori* or by including a very high level of correlation) and the quasilinear $^3CH_2$ (by including an appropriate correction for vibrational anharmonicity).

Others have also attempted high-accuracy thermochemical studies of CH_2.[14-19] An important prior work is that of Császár et al.,[14] who calculated $T_0(CH_2)$ via a composite *ab initio* protocol broadly similar to HEAT but differing substantially in several details. Unlike HEAT, the method of Császár was tailored to the CH_2 system, whereas HEAT is intended to be general in scope; thus, as discussed below, their result is in slightly better agreement with experiment than the HEAT result. Around the same time, Flores and Gdanitz approached the problem in another way, calculating the nonrelativistic Born-Oppenheimer electronic contribution to $T_0(CH_2)$ by the multireference averaged coupled-pair functional method; their result matched experiment to within ~1 kJ/mol.[10]

The water dimer, $(H_2O)_2$, is a standard loosely-bound complex of broad scientific interest. Importantly, it serves as a prototype for hydrogen bonding in general, and as a precursor to larger water clusters in particular.[20,21] As a result, there is a deeply pragmatic motivation to study its vibrational properties and its binding energy D_0; thus, these problems have been approached by many theoretical and experimental methods.[20-30] One theoretical challenge is that the vibrational mode leading to dissociation is quite anharmonic; thus, the usual harmonic approximation will fail to give a correct zero-point vibrational energy for the dimer. Another challenge is that accurate determination of D_0 suffers from the basis set superposition error (BSSE):[26,31] the quantum

calculation of the dimer includes more basis functions than does the calculation of the monomer, so the two monomer units within the dimer are treated more accurately than a lone monomer, leading to an artificial lowering of the dimer energy. The BSSE can be counteracted by using the same basis functions in the calculation of the monomer as are used for the dimer—the so-called "counterpoise method"—but this is computationally expensive, especially for large clusters. A simpler alternative is to perform calculations at the complete-basis-set limit, wherein both the cluster and the monomers use the same (complete) basis set by definition.

Many researchers have found that the CCSD(T) method is entirely adequate to calculate the dissociation energy D_0 of $(H_2O)_2$. A theoretical benchmark result comes from the complete *ab initio* potential energy surfaces and quasiclassical trajectory calculations of Huang, Braams, Bowman, and collaborators.[21,28,32-34] They used counterpoise-corrected all-electron CCSD(T)/aug-cc-pVTZ energies, modified by empirical parameters, with vibrational zero-point energy given by the quantum diffusion Monte Carlo method. Their complete potential energy surfaces predict D_0 to within a few wavenumbers of the experimental result. The vibrational properties of water clusters were studied using second-order vibrational perturbation theory with CCSD(T) at the extrapolated complete-basis-set limit by Howard et al.,[24] Howard and Tschumper,[23] and Temelso et al.[29] This result for D_0 differed from experiment by <0.5 kJ/mol. The HEAT study reported here is similarly accurate. The results reveal, in agreement with a conclusion of Lane via a different calculation scheme,[35] that the fortuitous cancellation of higher-order correlation and other corrections leads to the success of the usual all-electron nonrelativistic Born-Oppenheimer CCSD(T) method in this case.

5.2. Computational methods

In the first part of this study, several variations of the HEAT protocol are invoked to calculate

both the splitting between the $\tilde{X}^3B_1$ and $\tilde{a}^1A_1$ states of CH_2, and the dissociation energy of the H_2O dimer. These variations differ in the basis sets and high-level correlation used, with these options encoded in the name of the variation; thus, for example, "HEAT345-(Q)" represents the HEAT protocol using triple-, quadruple-, and pentuple-zeta basis sets and a CCSDT(Q) correction. Specifically, $T_0(CH_2)$ and D_0 of the water dimer are calculated by the HEAT345-X and HEAT456-X formulations, with X = (Q), Q, and QPH; moreover, another part of HEAT, the diagonal Born-Oppenheimer correction, is also considered at several levels of theory. A complete description of the HEAT protocol is reported elsewhere.[1-3] Briefly, the total energy of a species within the HEAT paradigm is calculated as the sum:

$$E_{\mathrm{HEAT}} = E_{\mathrm{HF}}^{\infty} + \Delta E_{\mathrm{CCSD(T)}}^{\infty} + \Delta E_{\mathrm{CCSDT}} + \Delta E_{\mathrm{HLC}} + \Delta E_{\mathrm{REL}} + \Delta E_{\mathrm{ZPE}} + \Delta E_{\mathrm{DBOC}}. \quad (1)$$

Here E_{HF}^{∞} is the Hartree-Fock energy, extrapolated to the complete basis set limit using the basis sets aug-cc-pCVXZ, with X = T, Q, and 5 in the HEAT345 suite and with X = Q, 5, and 6 in HEAT456. The extrapolation scheme is $E_{\mathrm{HF}}^{\infty} = E_{\mathrm{HF}}^{X} - a\exp(-bX)$, with the three free parameters a, b, and E_{HF}^{∞} determined from the three HF energies.

$\Delta E_{\mathrm{CCSD(T)}}^{\infty}$ is the electronic correlation energy calculated by CCSD(T) (not the total CCSD(T) energy), which is extrapolated by a two-point method using the basis sets aug-cc-pCVXZ, with X = Q and 5 for HEAT345 and X = 5 and 6 for HEAT456. The extrapolation scheme is $\Delta E_{\mathrm{CCSD(T)}}^{\infty} = \Delta E_{\mathrm{CCSD(T)}}^{X} - a/X^3$.

$\Delta E_{\mathrm{CCSDT}}$ is a frozen-core correction to the CCSD(T) energy, obtained by calculating the difference between the frozen-core CCSD(T) and CCSDT energies. Symbolically, $\Delta E_{\mathrm{CCSDT}} = E_{\mathrm{CCSDT}}^{\infty}(\mathrm{fc}) - E_{\mathrm{CCSD(T)}}^{\infty}(\mathrm{fc})$. In this case, the extrapolation to the complete basis-set limit is performed using cc-pVTZ and cc-pVQZ basis sets.

ΔE_{HLC} is a frozen-core "high-level correlation" correction, obtained by calculating the

difference between the frozen-core CCSDT and higher-level CC energies. Symbolically, $\Delta E_{\mathrm{HLC}} = E_{\mathrm{CCSDTX}}^{\mathrm{cc-pVDZ}}(\mathrm{fc}) - E_{\mathrm{CCSDT}}^{\mathrm{cc-pVDZ}}(\mathrm{fc})$; only the cc-pVDZ basis set is used. Due to the computational expense of high-level correlation, only CCSDTQ and CCSDT(Q) are typically used; in this study, however, CCSDTQPH is also used for methylene, to investigate whether the inclusion of such a high level of correlation is useful.

ΔE_{REL} is a correction for scalar relativistic effects, which is calculated at the CCSD(T)/aug-cc-pCVTZ level of theory. This correction includes one-electron mass-velocity terms and one- and two-electron Darwin terms.

ΔE_{ZPE} is the zero-point vibrational energy, calculated at the CCSD(T)/cc-pVQZ level of theory. The zero-point energy includes a treatment of anharmonicity via second-order vibrational perturbation theory.

Finally, ΔE_{DBOC} is the diagonal Born-Oppenheimer correction, which is a first-order correction to the Born-Oppenheimer approximation of the form $\Delta E_{\mathrm{DBOC}} = \langle \Psi_e(\mathbf{r};\mathbf{R}) | \hat{T}_n | \Psi_e(\mathbf{r};\mathbf{R}) \rangle$ where Ψ_e is the electronic wavefunction with electronic coordinates **r** and nuclear coordinates **R**, and $\hat{T}_n$ is the nuclear kinetic energy operator. In this study, ΔE_{DBOC} it is calculated at both the HF/aug-cc-pVTZ and CCSD/aug-cc-pCVQZ levels of theory; in the case of CH_2 it is moreover calculated at the CCSDT and CCSDTQ levels of theory, using the aug-cc-pCVQZ basis set.

Molecular geometries were optimized at the CCSD(T)/cc-pVQZ level of theory. RHF reference wavefunctions were used for $^1CH_2$, H_2O, and $(H_2O)_2$; UHF references were used for $^3CH_2$. All calculations were performed using the CFOUR (Coupled-Cluster techniques for Computational Chemistry) program,[36] except for those involving correlation effects above CCSDT, which moreover used the string-based many-body MRCC[37] code interfaced to CFOUR.

5.3. Results

5.3.1. Overview

In the following subsections we present the calculated values of each contribution to the total HEAT energy of $^3CH_2$, $^1CH_2$, H_2O, and $(H_2O)_2$, , as well as the appropriate differences needed to calculate the singlet-triplet gap of CH_2 and the dissociation energy of $(H_2O)_2$. In terms such as E_{HF}^{∞} that involve extrapolation, the superscript ∞ is replaced by "345" and "456" to represent the use of HEAT345- or HEAT456-type basis set extrapolation. Likewise, the terms ΔE_{HLC} and ΔE_{DBOC} are given a superscript to indicate what level of theory was used in the calculation, such as $\Delta E_{\mathrm{HLC}}^{\mathrm{CCSDTQ}}$ for a high-level correction using CCSDTQ. Total HEAT energies for all of the HEAT345-X and HEAT456-X methods are included in the tables; all of these results use the CCSD-type DBOC. The tables also include experimental values, as well as the values recommended by the Active Thermochemical Tables (ATcT) of Ruscic.[38]

5.3.2. Singlet-triplet gap T_e and T_0 of CH_2

Table 5.1 shows the values of the individual HEAT terms for $^3CH_2$ and $^1CH_2$, and the differences between them. The total HEAT energies of the two species, and the total T_e (difference of electronic energy) and T_0 (difference of zero-point corrected energy), are given in Table 5.2. For $^3CH_2$ the optimized geometric parameters were $r_{\mathrm{CH}} = 1.07436$ Å and $\angle_{\mathrm{HCH}} = 133.734°$; for $^1CH_2$ they were $r_{\mathrm{CH}} = 1.10517$ Å and $\angle_{\mathrm{HCH}} = 102.115°$. These values agree quite well with experiment and with other high-level calculations.[10] Fundamental frequencies calculated by VPT2 were 1019, 3045, and 3259 cm^{-1} for the triplet and 1368, 2818, and 2871 cm^{-1} for the singlet. The

experimentally-determined fundamentals for $^1CH_2$ are 1353, 2806, and 2865 cm^{-1}; VPT2 thus slightly overestimates each of these. The low-frequency bending mode of $^3CH_2$ is found experimentally at 963 cm^{-1}, also overestimated by VPT2. The high-frequency stretching modes of $^3CH_2$ have not been conclusively characterized, but fitting of experimental data predicts fundamentals of approximately 3000 cm^{-1} and 3230 cm^{-1}. The VPT2 results and comparisons with experiment are discussed in detail in Section 5.4.1.5.

5.3.3. Dissociation energy of $(H_2O)_2$

Tables 4 and 5 show the calculations of the HEAT terms for the water monomer and dimer, as well as the contribution of each term to the total D_0, simply computed as twice the value for the monomer less the value for the dimer. For H_2O the optimized geometric parameters were $r_{OH} = 0.95623$ Å and $\angle_{HOH} = 104.246°$. The optimized structure of $(H_2O)_2$ is shown in Figure 5.1. Fundamental frequencies of the monomer calculated by VPT2 (comparisons with experiment in parentheses) were 1609 (+14 vs. experiment), 3677 (+20), and 3771 (+15) cm^{-1}, and for the dimer they were 95 (+7), 103 (-5), 112 (+9), 150 (+7), 310, 513, 1614, 1631, 3628 (+26), 3670 (+19), 3747 (+17), and 3759 (+14) cm^{-1}.[24] Gas-phase experimental data are not available for four of the vibrations.

Species	$^3CH_2$ (Hartree)	$^1CH_2$ (Hartree)	Diff. (cm^{-1})
$E_{HF}^{\infty,345}$	−38.941 051	−38.896 153	9853.98
$E_{HF}^{\infty,456}$	−38.940 970	−38.896 081	9851.96
$\Delta E_{CCSD(T)}^{345}$	−0.207 842	−0.237 430	−6493.91
$\Delta E_{CCSD(T)}^{456}$	−0.207 475	−0.237 089	−6499.60
ΔE_{CCSDT}	−0.000 458	−0.000 766	−67.67
$\Delta E_{HLC}^{CCSDT(Q)}$	−0.000 071	−0.000 152	−17.90
ΔE_{HLC}^{CCSDTQ}	−0.000 081	−0.000 182	−22.33
$\Delta E_{HLC}^{CCSDTQPH}$	−0.000 084	−0.000 189	−23.05
ΔE_{DBOC}^{HF}	0.002 154	0.002 368	46.90
ΔE_{DBOC}^{CCSD}	0.002 234	0.002 502	58.84
ΔE_{REL}	−0.016 052	−0.016 155	−22.63
ΔE_{ZPE}	0.017 110	0.016 504	−133.17

Table 5.1. Calculated terms used by the HEAT protocol to determine $T_e(CH_2)$ and $T_0(CH_2)$. Final HEAT energies are reported in Table 5.2. The HEAT terms are listed with 0.2 cm^{-1} precision to permit their use as high-accuracy benchmarks, and for comparison to other high-accuracy methods.

HEAT energy	$^3CH_2$ (Ha)	$^1CH_2$ (Ha)	T_e (cm^{-1})	T_0 (cm^{-1})
345-(Q)	−39.146 128	−39.131 650	3310.71	3177.54
456-(Q)	−39.145 680	−39.131 237	3303.00	3169.84
345-Q	−39.146 138	−39.131 681	3306.27	3173.11
456-Q	−39.145 690	−39.131 267	3298.57	3165.40
345-QPH	−39.146 141	−39.131 687	3305.55	3172.39
456-QPH	−39.145 693	−39.131 274	3297.85	3164.68
ATcT[a]	–	–	–	3149±14
Expt.[b]	–	–	3223	3147± 5

Table 5.2. Final HEAT energies of triplet and singlet CH_2, and the values of T_e and T_0 obtained as the difference between the singlet and triplet HEAT energies. Also included are experimental and recommended values. All HEAT results use the DBOC term calculated by CCSD. The HEAT terms are listed with 0.2 cm^{-1} precision to permit their use as high-accuracy benchmarks, and for comparison to other high-accuracy methods. [a]Ref. 38. [b]Empirical result of refs. 18, 19.

Species	H_2O (Hartree)	$(H_2O)_2$ (Hartree)	Diff. (cm^{-1})
$E_{HF}^{\infty,345}$	−76.067 761	−152.140 917	1184.02
$E_{HF}^{\infty,456}$	−76.067 529	−152.140 475	1188.74
$\Delta E_{CCSD(T)}^{345}$	−0.373 670	−0.749 875	556.29
$\Delta E_{CCSD(T)}^{456}$	−0.370 876	−0.744 283	555.72
ΔE_{CCSDT}	0.000 033	0.000 085	−4.42
$\Delta E_{HLC}^{CCSDT(Q)}$	−0.000 483	−0.000 989	5.19
ΔE_{HLC}^{CCSDTQ}	−0.000 453	−0.000 926	4.16
ΔE_{DBOC}^{HF}	0.002 710	0.005 395	5.53
ΔE_{DBOC}^{CCSD}	0.002 828	0.005 631	5.40
ΔE_{REL}	−0.055 192	−0.110 357	−5.91
ΔE_{ZPE}	0.021 246	0.045 580	−677.74

Table 5.3. Calculated terms used by the HEAT protocol to determine D_e and D_0 of the water dimer. Final HEAT energies are reported in Table 5.4. The HEAT terms are listed with 0.2 cm^{-1} precision to permit their use as high-accuracy benchmarks, and for comparison to other high-accuracy methods.

HEAT energy	H_2O (Hartree)	$(H_2O)_2$ (Hartree)	D_0 (cm^{-1})
345-(Q)	−76.472 999	−152.950 841	1062.83
456-(Q)	−76.469 973	−152.944 808	1066.98
345-Q	−76.472 970	−152.950 778	1061.80
456-Q	−76.469 944	−152.944 744	1065.95
ATcT[a]	–	–	1105±35
Expt.[b]	–	–	1105±10

Table 5.4. Total HEAT energies of H_2O and $(H_2O)_2$ and the final result for D_0. All HEAT values use the DBOC calculated by CCSD. The HEAT terms are listed with 0.2 cm^{-1} precision to permit their use as high-accuracy benchmarks, and for comparison to other high-accuracy methods. [a]Ref. 38. [b]Refs. 21, 34.

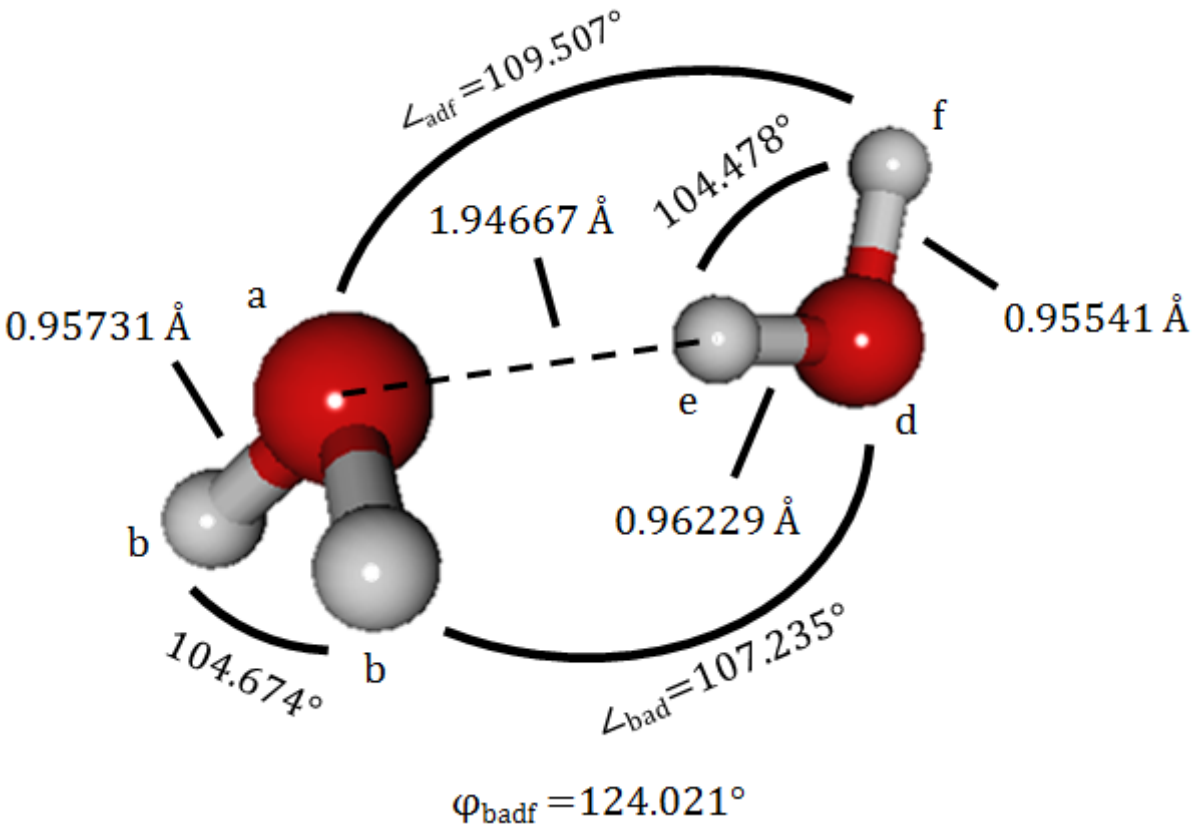

Figure 5.1. Optimized minimum-energy geometry of the water dimer at the CCSD(T)/cc-pVQZ level of theory, as used by the HEAT protocol.

5.4. Discussion

5.4.1. HEAT results for CH_2

5.4.1.1. Basis set convergence

The results in Table 5.1 show the dependence of the HEAT energies of $^3CH_2$ and $^1CH_2$ on the size of the extrapolated basis set. The rows titled E_{HF} show that ascending from the 345 basis to the 456 basis increases the calculated HF energy of both species by a miniscule ~0.2 kJ/mol, so the HF treatment is seen to be well-converged at the 345 level. Indeed, the individual pentuple-zeta energies (not shown in the table) are only ~30 cm^{-1} above the extrapolated values, so it is understandable that inclusion of a hextuple-zeta calculation has little effect. However, the rows titled $\Delta E_{\mathrm{CCSD(T)}}$ show, as anticipated above, that the correlation energies of each species change by a more significant 2 kJ/mol under the larger extrapolation scheme; the 456 basis, therefore, is needed to calculate the best *total* HEAT energy. To calculate T_0, however, only requires a correct *difference* between the singlet and triplet energies; encouragingly, increasing the size of the basis set contributes less than 3 cm^{-1} to T_0. Thus, while it is not clear whether the *total* correlation energies are well-converged under 456 extrapolation, the error is at least systematic, a desirable feature in quantum calculation. In the case of CH_2, then, we conclude that HEAT456 confers only a trivial advantage over HEAT345.

5.4.1.2. Convergence of correlation effects above CCSD(T)

The rows of Table 5.1 indexed as $\Delta E_{\mathrm{CCSDT}}$ and ΔE_{HLC} show the contributions of (frozen-core) CCSDT and higher-level correlations to the total HEAT energy of CH_2. Inclusion of $\Delta E_{\mathrm{CCSDT}}$ is clearly necessary to obtain good accuracy in the total HEAT energy of both species, as it contributes >1 kJ/mol of stabilization to the triplet, and fully 2 kJ/mol to the singlet. The greater

stabilization of the singlet is a result of its two-configurational character, which requires a high level of correlation to treat properly. Thus the CCSDT term leads to a lowering by 68 cm^{-1} of the calculated T_0. Every version of the HEAT protocol also includes ΔE_{HLC}; one goal of this study is to evaluate the convergence of the different HLC options. Improving the HLC treatment from CCSDT(Q) to CCSDTQ changes the energy of $^3CH_2$ by 2 cm^{-1}, and the energy of $^1CH_2$ by 7 cm^{-1}, together leading to a change of 5 cm^{-1} in T_0. This is certainly not a large absolute difference, but in a relative sense it does amount to a significant ~30% of $\Delta E_{\mathrm{HLC}}^{\mathrm{CCSDT(Q)}}$. Going further, the change in total energy of each species when ascending from Q-level correlation to QPH is <2 cm^{-1}, and the total change in T_0 is <1 cm^{-1}. Thus, the Q-level correlation can be considered better-converged than the (Q)-level correlation, while the QPH-level correlation confers no significant advantage over the Q-level correlation in this case.

5.4.1.3. The diagonal Born-Oppenheimer correction (DBOC)

The next two rows of Table 5.1 concern the diagonal correction to the Born-Oppenheimer approximation, ΔE_{DBOC}, evaluated by both the HF and CCSD methods. In the case of CH_2, others have also evaluated $\Delta E_{\mathrm{DBOC}}^{\mathrm{HF}}$ using slightly different approaches than the prescribed HEAT method.[14,39] Specifically, they concluded that this term contributes approximately +48 cm^{-1} to T_0 if single-configuration SCF is used for $^1CH_2$, and approximately 40 cm^{-1} if two configurations are used. Those studies used basis sets up to TZ2P+f; the value varies slightly with basis set, so the HEAT result of 47 cm^{-1}, which uses single-reference SCF with the aug-cc-pVTZ basis, is consistent with the previous work.

The new result in this work is $\Delta E_{\mathrm{DBOC}}^{\mathrm{CCSD}}$. The CCSD DBOC correction is more destabilizing for both $^3CH_2$ and $^1CH_2$ than is the HF DBOC, as is expected for most species;[3] moreover, the

singlet is destabilized by an additional 12 cm^{-1} over the triplet, so the calculated singlet-triplet splitting is increased by that amount. Thus, the contribution of $\Delta E_{\mathrm{DBOC}}^{\mathrm{CCSD}}$ to T_0 is +59 cm^{-1}. It may be, however, that none of these methods is satisfactory for the case CH_2, which (as shown in Section 5.4.1.3) requires a higher-level treatment than CCSD. If we instead calculate the DBOC using CCSDT correlation, we find that its contribution to T_0 is $\Delta E_{\mathrm{DBOC}}^{\mathrm{CCSDT}}$ = 28 cm^{-1}, in agreement with the sign of the two-configuration SCF correction but in disagreement with its magnitude. Thus, while $\Delta E_{\mathrm{DBOC}}^{\mathrm{CCSD}}$ is certainly more rigorous than the HF calculations, the use of CCSD may still introduce some (small) error when comparing systems such as $^1CH_2$ and $^3CH_2$ that have vastly different levels of correlation.

5.4.1.4. The one- and two-electron relativistic corrections

The relativistic correction to the total energy, ΔE_{REL} in Table 2, includes mass-velocity and one- and two-electron Darwin terms, as in most variations of the HEAT protocol. Its contribution to the singlet-triplet splitting is -23 cm^{-1}, arising from a stabilization of 42.1 kJ/mol in the triplet and slightly more in the singlet. The two-electron term is typically considered negligible with respect to the more important mass-velocity and one-electron terms. In the CH_2 case, the two-electron term (not included in the table) stabilizes both species by about 3.1 kJ/mol, or 7.4% of the total ΔE_{REL}; its contribution to the total T_0 is thus an absolutely negligible 2 cm^{-1}. Predictably, the value $\Delta E_{\mathrm{REL}} =$ -23 cm^{-1} is in near perfect agreement with the value of -22 cm^{-1} determined by Császár et al.,[14] who also used CCSD(T) correlation and a large basis set. The original SCF result of Davidson et al., which used an ROHF reference for the triplet and two-configuration HF for the singlet, is -29 cm^{-1};[40] the CCSD(T) result is to be preferred, however, because of the need to include high levels of correlation for an adequate description of CH_2.

5.4.1.5. Zero-point energy and error due to the VPT2 model

The harmonic oscillator model fails utterly to describe the zero-point energy of $^3CH_2$, because of the molecule's significant anharmonicity.[14,41] This species is in fact quasilinear, with a large HCH bond angle (133° at equilibrium), a low barrier along the bending mode, and strong coupling between the bending mode and the C_2 rotation. Indeed, the anharmonicity of $^3CH_2$ is so extreme that the usual anharmonic correction, second-order vibrational perturbation theory (VPT2), cannot compensate for the error of the harmonic model.[41] The calculated harmonic bending frequency is $v_2 = 1019$ cm^{-1}, which is much larger than the experimental result of 963 cm^{-1}.[42] In the case of CH_2, superior approaches to calculating the ZPE include the Morse oscillator rigid bender internal dynamics (MORBID) Hamiltonian, as considered by Comeau et al.[13] and Jensen and Bunker,[19] and the nonrigid-rotation large-amplitude internal-motion Hamiltonian (NRLH), considered by Császár et al.[14] Nevertheless, the HEAT suite employs VPT2, so we report that result here. Table 5.1 shows that the calculated zero-point vibrational energy, including the VPT2 correction, is 44.9 kJ/mol in the triplet and 43.3 kJ/mol in the singlet; the difference of ZPEs thus contributes -133 cm^{-1} to T_0. The harmonic contribution to T_0 (not shown in the table) is -144 cm^{-1}, so VPT2 provides only a small adjustment. By comparison, Császár et al., using the NRLH method, calculated that the ZPE difference contributes -124 cm^{-1} to T_0,[14] while Comeau et al. calculated this value to be -127 cm^{-1} using an *ab initio* MORBID approach.[13] The ZPE has not yet been determined experimentally, because there has been no experimental observation of the stretching fundamentals of $^3CH_2$; instead, the best empirical estimate of ΔE_{ZPE} is -76 cm^{-1}, derived by Jensen and Bunker using the MORBID method fitted to experimental data.[19]

5.4.1.6. Total HEAT energies of CH_2 and discussion of errors

Table 5.2 shows the final HEAT results for $^3CH_2$ and $^1CH_2$ using six different versions of the HEAT protocol. Additionally, the last two rows of the table show the singlet-triplet splitting calculated using the enthalpies of formation in the Active Thermochemical Tables, as well as an empirical value. The ATcT result is $T_0 = 3149 \pm 14$ cm^{-1},[38] while the commonly accepted empirical values for T_e and T_0 are 3223 cm^{-1} and 3147±5 cm^{-1} respectively.[18,19] The HEAT values for T_e are approximately 80 cm^{-1} (~1 kJ/mol) higher than the empirical value. However, every iteration of the HEAT protocol is seen to give a T_0 within +30 cm^{-1} of the empirical and ATcT values, a remarkably good agreement. The use of a larger basis set and a higher level of correlation reduce the calculated T_0, giving better agreement with the empirical and ATcT values: the T_0 acquired at the highest level of theory, HEAT456-QPH, is lower by 13 cm^{-1} than the T_0 acquired at the lowest level of theory, HEAT345-(Q). Most of this 13 cm^{-1} difference is due to the choice of 345- vs. 456-based extrapolation (see Section 5.4.1.1), not to the choice of higher-level correlation. Thus, the lowest level of the HEAT protocol, HEAT345-(Q), is almost as accurate as HEAT456-QPH, yet is considerably less computationally expensive. Notably, the T_e calculated by the methylene-specific protocol of Császár et al. was 3262 cm^{-1}, or only ~40 cm^{-1} nearer to the empirical value than the HEAT result. Their scheme differed from this one primarily in the use of an ROHF reference wavefunction for $^3CH_2$ and a valence-only basis set extrapolation with separate treatment of core correlation; this distinction alone accounts for nearly all of the 40 cm^{-1} disagreement.

As mentioned above, some features of HEAT are not ideal for the case of CH_2. The final result agrees exceptionally well with the empirical value in spite of these deficiencies, indicating the robustness of the HEAT method, but for the sake of completeness these issues are discussed in detail here. First, the CCSDT and HLC corrections use a frozen-core approximation, ignoring correlation

of the core and valence electrons. The prior work of Császár et al., which did not use a frozen core, showed that correlation of the core electrons contributes approximately 100 cm^{-1} to T_0, most of which is recovered by CCSD(T).[14] However, at higher levels of theory, correlation of the core electrons does produce a small negative contribution to T_0, which is not captured in the frozen-core CCSDT and HLC results of HEAT. Second, the DBOC calculated by CCSD introduces a positive error (increasing the calculated T_e), evidenced by the fact that the calculated contribution of $\Delta E_{\mathrm{DBOC}}^{\mathrm{CCSD}}$ is nearly 20 cm^{-1} greater than the two-configuration HF result,[39] and nearly 40 cm^{-1} greater than the $\Delta E_{\mathrm{DBOC}}^{\mathrm{CCSDT}}$ result. Most importantly, however, the use of VPT2 for calculating the vibrational ZPE leads to error due to the extreme anharmonicity of $^3CH_2$. In the absence of experimental observation of the $^3CH_2$ stretching fundamentals, the magnitude of this ZPE error is difficult to characterize. However, empirical results (see Section 5.4.1.5) suggest a ZPE contribution to T_0 of -76 cm^{-1}, whereas the VPT2 result is -133 cm^{-1}, a considerable disagreement. Summarizing, the HEAT result for T_0 likely includes positive errors due to the treatment of core correlation and the DBOC, fortuitously cancelled by a negative error due to the use of VPT2.

5.4.2. H_2O and $(H_2O)_2$

5.4.2.1. Convergence of basis set and higher-level correlation

Calculations of D_0 for the water dimer are expected to suffer some basis set superposition error, which vanishes as the size of the basis set is increased. Table 5.3 shows the dependence of the HEAT energies of H_2O and $(H_2O)_2$ on the size of the extrapolated basis set. The E_{HF} and $\Delta E_{\mathrm{CCSD(T)}}$ terms are clearly well-converged under the 345 basis set: ascending to 456 extrapolation confers a change of a trivial +5 cm^{-1} in the HF energy and −1 cm^{-1} in the CCSD(T) correlation energy. The large size and apparent convergence of these basis sets gives us confidence that the HEAT protocol,

in this case, avoids the basis set superposition error. This conclusion is consistent with a previous result of Lane and Kjaergaard,[31] who found that the CCSD(T)/aug-cc-pVTZ dissociation threshold of $(H_2O)_2$ is within 1 kJ/mol of the CCSD(T)/aug-cc-pV∞Z limit.

The contributions of correlation affects above CCSD(T) are presented in the next few rows of Table 5.3. The $\Delta E_{\mathrm{CCSDT}}$ term destabilizes both H_2O and $(H_2O)_2$ by a few wavenumbers, leading to a net reduction of D_0 by 4 cm^{-1}. The ΔE_{HLC} term, however, contributes significantly to the total HEAT energies: including high-level correlation stabilizes the monomer by 1.2 kJ/mol and the dimer by 2.5 kJ/mol. Thus, higher-level correlation in the *total* HEAT energies is not converged at the CCSDT level. The *change* in D_0 owing to ΔE_{HLC}, however, is only ~4 cm^{-1}, which is equal and opposite to the change due to $\Delta E_{\mathrm{CCSDT}}$. These results prove that, fortuitously, the calculation of D_0 is "well-converged" at the CCSD(T) level because the higher correlations are small in magnitude and cancel one another.

5.4.2.2. The diagonal Born-Oppenheimer and relativistic corrections

The rows of Table 5 indexed as ΔE_{DBOC} and ΔE_{REL} give the HEAT corrections due to the DBOC and relativistic effects in the monomer, dimer, and D_0. These terms contribute strongly to the absolute HEAT energies of each species: the DBOC is approximately 7 kJ/mol per H_2O unit, and the relativistic correction is approximately 145 kJ/mol per H_2O unit. However, the two corrections affect the dimer with almost exactly double their magnitude for the monomer, so the DBOC and relativistic corrections to D_0 are an insignificant +5 cm^{-1} and −6 cm^{-1} respectively. Ascending from the HF treatment of the DBOC to a CCSD treatment destabilizes both species, as expected; the amount of destabilization is again almost exactly twice as much in the dimer as in the monomer, so the change in D_0 due to correlation in the DBOC is virtually zero. This result is not unusual, since, as explained

in Section 5.4.2.1, a high level of correlation is not needed to correctly describe either the monomer or the dimer. The two-electron Darwin contribution to ΔE_{REL} (not shown in the table) is a mere 5.7% of the total ΔE_{REL} in both species.

5.4.2.3. Zero-point energy and error due to basis set

The final row of Table 5.3 gives the VPT2 ZPE of H_2O and $(H_2O)_2$ and the contribution of this term to D_0. The calculated fundamental vibrational frequencies are reported in Section 5.3.3. Notably, all of the calculated frequencies are greater than their experimental values where gas-phase experimental data are available;[24] the worst offender is the ν_3 mode of $(H_2O)_2$, whose calculated fundamental of 3629 cm^{-1} is 27 cm^{-1} higher than the experimental value. The total vibrational ZPEs are therefore higher than is expected from experiment. Because the dimer is affected more strongly, the magnitude of the ZPE contribution to D_0 is exaggerated.

We attribute this discrepancy in the ZPEs to the choice of basis set. The HEAT method uses non-augmented cc-pVQZ for the calculation of ΔE_{ZPE}, but others have shown that a rigorous treatment of $(H_2O)_2$ requires diffuse functions in the basis set.[31,35] For comparison, Howard et al.[24] also performed VPT2 calculations for H_2O and $(H_2O)_2$ with CCSD(T) correlation, but their basis set was cc-pVQZ with diffuse functions attached to the oxygen atoms; their calculated frequencies were in good agreement with experiment, with two exceptions where (in diametric opposite to the HEAT results) the calculated values were far too low.

5.4.2.4. Total HEAT energies of H_2O and $(H_2O)_2$, and discussion of errors

Table 5.4 shows the total HEAT energies of H_2O and $(H_2O)_2$ as well as the total dissociation

energy, calculated using four different versions of the protocol. The D_0 recommended by the Active Thermochemical Tables and by the best available experiment are also included. The HEAT results agree quite well with the standard values, with the calculated D_0 being only 0.5 kJ/mol too low. Coincidentally, an agreement within 0.5 kJ/mol is a commonly accepted threshold of quality for "sub-chemical accuracy"; thus the HEAT method does achieve sub-chemical accuracy in this case. The results obtained with different versions of HEAT lie within 7 cm^{-1} of one another, meaning that the different versions of the protocol agree with one another extraordinarily well. Therefore, in this case the least expensive HEAT protocol, HEAT345-(Q), performs only trivially worse than the technically superior protocols, and can be recommended.

The total *electronic* contribution to D_0, consisting of every term in the total HEAT energy except ΔE_{ZPE}, is exceptionally well-converged at the CCSD(T)/aug-cc-pCV∞Z level. That is, all of the corrective terms $\Delta E_{\mathrm{CCSDT}}$, ΔE_{HLC}, ΔE_{DBOC}, and ΔE_{REL} are only a few wavenumbers in magnitude and have opposing signs, so they cancel entirely. The total electronic contribution (not shown in Table 5.4) is approximately 1743 cm^{-1}, essentially identical to the results of others calculated at high levels of theory.[24,28,34,35] The VPT2 ZPE result of HEAT, however, differs from the diffusion Monte Carlo ZPE result of Shank et al.[28] by approximately -40 cm^{-1}, and from the VPT2 result of Howard et al.[24] (acquired with a larger basis set) by -31 cm^{-1}. If, as seems likely, the electronic contribution is not only well-converged but completely accurate, then the disagreement of the HEAT results with experiment must arise from ΔE_{ZPE}, perhaps indicating that VPT2 with the non-augmented cc-pVQZ basis set is not well-suited to this problem.

5.5. Conclusion

The results and analysis of Section 4 show that every common variation of the HEAT

protocol, including the least expensive HEAT345-(Q) method, adequately treats the thermochemistry of both methylene and the water dimer with sub-kilojoule accuracy. In the case of methylene, the best empirical estimate of T_0 is ~3148 cm^{-1}; the HEAT345-(Q) method calculates T_0 = 3178 cm^{-1}. Ascending to the level of HEAT456-QPH improves the result by only 13 cm^{-1}. Corrections to T_0 beyond CCSD(T) are clearly necessary to achieve high accuracy; the HEAT protocol includes such high-level corrections. Disagreement with the experimental value likely arises from the lack of core correlation in HEAT's CCSDT and HLC terms, from the use of VPT2 for the anharmonic correction, and from insufficient correlation in the calculation of the DBOC. In the case of the water dimer, the accepted D_0 is 1105 cm^{-1}; HEAT345-(Q) obtains 1063 cm^{-1}. The "best" result obtained (in the sense of agreement with experiment) is that of HEAT456-(Q), which only improves the HEAT345-(Q) result by 4 cm^{-1}. Corrections to D_0 beyond CCSD(T) are small in magnitude and have opposing signs, a result that explains the previous success of CCSD(T) alone for calculations of $(H_2O)_2$. In both the CH_2 and H_2O cases, the least reliable HEAT term seems to be the VPT2 zero-point energy.

The HEAT protocol is designed to be completely general, free of any empirical parameters or *a priori* assumptions about the chemical system. This study shows, however, that in the interesting cases of CH_2 and $(H_2O)_2$ the HEAT method not only achieves sub-chemical accuracy, but performs as well as previous methods that were tailored to these two systems. These results speak to both the power and the robustness of the HEAT approach.

5.6. References

1. Tajti, A.; Szalay, P. G.; Császár, A. G.; Kállay, M.; Gauss, J.; Valeev, E. F.; Flowers, B. A.;

Vásquez, J.; Stanton, J. F. HEAT: High accuracy extrapolated ab initio thermochemistry. *Journal of Chemical Physics* **2004,** *121*, 11599-11613.

2. Bomble, Y. J.; Vásquez, J.; Kállay, M.; Michauk, C.; Szalay, P. G.; Császár, A. G.; Gauss, J.; Stanton, J. F. High-accuracy extrapolated ab initio thermochemistry. II. Minor improvements to the protocol and a vital simplification. *Journal of Chemical Physics* **2006,** *125*, 064108.

3. Harding, M. E.; Vásquez, J.; Ruscic, B.; Wilson, A. K.; Gauss, J.; Stanton, J. F. High-accuracy extrapolated ab initio thermochemistry. III. Additional improvements and overview. *Journal of Chemical Physics* **2008,** *128*, 114111.

4. Tabor, D. P.; Harding, M. E.; Ichino, T.; Stanton, J. F. High-Accuracy Extrapolated Ab Initio Thermochemistry of the Vinyl, Ally, and Vinoxy Radicals. *Journal of Physical Chemistry A* **2012,** *116*, 7668-7676.

5. Harding, M. E.; Vásquez, J.; Gauss, J.; Stanton, J. F.; Kállay, M. Towards highly accurate ab initio thermochemistry of larger systems: Benzene. *Journal of Chemical Physics* **2011,** *2011*, 044513.

6. Barker, J. R.; Nguyen, T. L.; Stanton, J. F. Kinetic Isotope Effects for Cl + CH_4 ⇌ HCl + CH_3 Calculated Using ab Initio Semiclassical Transition State Theory. *Journal of Physical Chemistry A* **2012,** *116*, 6408-6419.

7. Nguyen, T. L.; Stanton, J. F. Ab Initio Thermal Rate Calculations of HO + HO = O(^{3}P) + H_2O Reaction and Isotopologues. *Journal of Physical Chemistry A* **2013,** *117*, 2678-2686.

8. Nguyen, T. L.; Stanton, J. F.; Barker, J. R. Ab Initio Reaction Rate Constants Computed Using Semiclassical Transition-State Theory: HO + H_2 -> H_2O + H and Isotopologues. *Journal of Physical Chemistry A* **2011,** *115*, 5118-5126.

9. Schaefer, H. F., III. Methylene: A Paradigm for Computational Quantum Chemistry. *Science*

1986, *231,* 1100-1107.

10. Flores, J. R.; Gdanitz, R. J. Accurately solving the electronic Schrödinger equation of small atoms and molecules using explicitly correlated (r12-)MR-CI. VIII. Valence excited states of methylene (CH_2). *Journal of Chemical Physics* **2005,** *123,* 144316.

11. Li, X.; Piecuch, P.; Paldus, J. A study of $^1A_1$-$^3B_1$ separation in CH_2 using orthogonally spin-adapted state-universal and state-specified coupled-cluster methods. *Chemical Physics Letters* **1994,** *224,* 267-274.

12. Sherrill, C. D.; Van Huis, T. J.; Yamaguchi, Y.; Schaefer III, H. F. Full configuration interaction benchmarks for the X^3B_1, a^1A_1, b^1B_1, and c^1A_1 states of methylene. *Journal of Molecular Structure (Theochem)* **1997,** *400,* 139-156.

13. Comeau, D. C.; Shavitt, I.; Jensen, P.; Bunker, P. R. An ab initio determination of the potential-energy surfaces and rotation-vibration energy levels of methylene in the lowest triplet and singlet states and the singlet-triplet splitting. *Journal of Chemical Physics* **1989,** *90,* 6491-6500.

14. Császár, A. G.; Leininger, M. L.; Szalay, V. The standard enthalpy of formation of CH_2. *Journal of Chemical Physics* **2003,** *118,* 10631-10642.

15. Furtenbacker, T.; Czakó, G.; Sutcliffe, B. T.; Császár, A. G.; Szalay, V. The methylene saga continues: Stretching fundamentals and zero-point energy of X^3B_1 CH_2. *Journal of Molecular Structure* **2006,** *780-781,* 283-294.

16. Gu, J.-P.; Hirsch, G.; Buenker, R. J.; Brumm, M.; Osmann, G.; Bunker, P. R.; Jensen, P. A theoretical study of the absorption spectrum of singlet CH_2. *Journal of Molecular Structure* **2000,** *517-518,* 247-264.

17. Yamaguchi, Y.; Sherrill, C. D.; Schaefer, H. F., III. The X^3B_1, a^1A_1, b^1B_1, and c^1A_1 Electronic States of CH_2. *Journal of Physical Chemistry* **1996,** *100,* 7911-7918.

18. Bunker, P. R.; Jensen, P.; Kraemer, W. P.; Beardsworth, R. The potential surface of X^3B_1 methylene (CH_2) and the singlet-triplet splitting. *Journal of Chemical Physics* **1986,** *85,* 3724-3731.

19. Jensen, P.; Bunker, P. R. The potential surface and stretching frequencies of $\tilde{X}^3B_1$ methylene (CH_2) determined from experiment using the Morse oscillatorrigid bender internal dynamics Hamiltonian. *Journal of Chemical Physics* **1988,** *89,* 1327-1332.

20. Mukhopadhyay, A.; Cole, W. T. S.; Saykally, R. J. The water dimer I: Experimental characterization. *Chemical Physics Letters* **2015,** *633,* 13-26.

21. Rocher-Casterline, B. E.; Ch'ng, L. C.; Mollner, A. K.; Reisler, H. Communication: Determination of the bond dissociation energy (D_0) of the water dimer, $(H_2O)_2$, by velocity map imaging. *Journal of Chemical Physics* **2011,** *134,* 211101.

22. Klopper, W.; van Duijneveldt-van de Rijdt, J. G. C. M.; van Duijneveldt, F. B. Computational determination of equilibrium geometry and dissociation energy of the water dimer. *Physical Chemistry Chemical Physics* **2000,** *2,* 2227-2234.

23. Howard, J. C.; Tschumper, G. S. Benchmark Structures and Harmonic Vibrational Frequencies Near the CCSD(T) Complete Basis Set Limit for Small Water Clusters: $(H_2O)_n$=2,3,4,5,6. *Journal of Chemical Theory and Computation* **2015,** *11,* 2126-2136.

24. Howard, J. C.; Gray, J. L.; Hardwick, A. J.; Nguyen, L. T.; Tschumper, G. S. Getting down to the Fundamentals of Hydrogen Bonding: Anharmonic Vibrational Frequencies of $(HF)_2$ and $(H_2O)_2$ from Ab Initio Electronic Structure Computations. *Journal of Chemical Theory and Computation* **2014,** *10,* 5426-5435.

25. Samanta, A. K.; Czakó, G.; Wang, Y.; Mancini, J. S.; Bowman, J. M.; Reisler, H. Experimental and Theoretical Investigations of Energy Transfer and Hydrogen-Bond Breaking in Small Water and HCl Clusters. *Accounts of Chemical Research* **2014,** *47,* 2700-2709.

26. Schütz, M.; Brdarski, S.; Widmark, P.-O.; Lindh, R.; Karlström, G. The water dimer interaction energy: Convergence to the basis set limit at the correlated level. *Journal of Chemical Physics* **1997,** *107,* 4597-4605.

27. Schütz, M.; Rauhut, G.; Werner, H.-J. Local Treatment of Electron Correlation in Molecular Clusters: Structures and Stabilities of $(H_2O)_n$, n = 2-4. *Journal of Physical Chemistry A* **1998,** *102,* 5997-6003.

28. Shank, A.; Wang, Y.; Kaledin, A.; Braams, B. J.; Bowman, J. M. Accurate ab initio and "hybrid" potential energy surfaces, intramolecular vibrational energies, and classical ir spectrum of the water dimer. *Journal of Chemical Physics* **2009,** *130,* 144314.

29. Temelso, B.; Archer, K. A.; Shields, G. C. Benchmark Structures and Binding Energies of Small Water Clusters with Anharmonicity Corrections. *Journal of Physical Chemistry A* **2011,** *115,* 12034-12046.

30. Tschumper, G. S.; Leininger, M. L.; Hoffman, B. C.; Valeev, E. F.; Schaefer, H. F., III; Quack, M. Anchoring the water dimer potential energy surface with explicitly correlated computations and focal point analyses. *Journal of Chemical Physics* **2002,** *116,* 690-701.

31. Lane, J. R.; Kjaergaard, H. G. Explicitly correlated intermolecular distances and interaction energies of hydrogen bonded complexes. *Journal of Chemical Physics* **2009,** *131,* 034307.

32. Huang, X.; Braams, B. J.; Bowman, J. M. Ab Initio Potential Energy and Dipole Moment Surfaces of $(H_2O)_2$. *Journal of Physical Chemistry A* **2006,** *110,* 445-451.

33. Huang, X.; Braams, B. J.; Bowman, J. M.; Kelly, R. E. A.; Tennyson, J.; Groenenboom, G. C.; van der Avoird, A. New ab initio potential energy surface and the vibration-rotation-tunneling levels of $(H_2O)_2$ and $(D_2O)_2$. *Journal of Chemical Physics* **2008,** *128,* 034312.

34. Ch'ng, L. C.; Samanta, A. K.; Czakó, G.; Bowman, J. M.; Reisler, H. Experimental and

Theoretical Investigations of Energy Transfer and Hydrogen-Bond Breaking in the Water Dimer. *Journal of the American Chemical Society* **2012,** *134,* 15430-15435.

35. Lane, J. R. CCSDTQ Optimized Geometry of Water Dimer. *Journal of Chemical Theory and Computation* **2013,** *9,* 316-323.

36. CFOUR, Coupled-Cluster techniques for Computational Chemistry, a quantum-chemical program package by J.F. Stanton, J. Gauss, M.E. Harding, P.G. Szalay with contributions from A.A. Auer, R.J. Bartlett, U. Benedikt, C. Berger, D.E. Bernholdt, Y.J. Bomble, L. Cheng, O. Christiansen, M. Heckert, O. Heun, C. Huber, T.-C. Jagau, D. Jonsson, J. Jusélius, K. Klein, W.J. Lauderdale, F. Lipparini, D.A. Matthews, T. Metzroth, L.A. Mück, D.P. O'Neill, D.R. Price, E. Prochnow, C. Puzzarini, K. Ruud, F. Schiffmann, W. Schwalbach, C. Simmons, S. Stopkowicz, A. Tajti, J. Vázquez, F. Wang, J.D. Watts and the integral packages MOLECULE (J. Almlöf and P.R. Taylor), PROPS (P.R. Taylor), ABACUS (T. Helgaker, H.J. Aa. Jensen, P. Jørgensen, and J. Olsen), and ECP routines by A. V. Mitin and C. van Wüllen. For the current version, see http://www.cfour.de.

37. M. Kállay (2007); see http://www.mrcc.hu.

38. B. Ruscic, Active Thermochemical Tables (ATcT) values based on ver. 1.112 of the Thermochemical Network (2013); available at ATcT.anl.gov.

39. Handy, N. C.; Yamaguchi, Y.; Schaefer, H. F., III. The diagonal correction to the Born-Oppenheimer approximation: Its effect on the singlet-triplet splitting of CH_2 and other molecular effects. *Journal of Chemical Physics* **1986,** *84,* 4481-4484.

40. Davidson, E. R.; Feller, D.; Phillips, P. Relativistic Corrections for Methylene. *Chemical Physics Letters* **1980,** *76,* 416-417.

41. Clabo Jr., D. A.; Allen, W. D.; Remington, R. B.; Yamaguchi, Y.; Schaefer, H. F., III. A Systematic Study of Molecular Vibrational Anharmonicity and Vibration-Rotation Interaction by

Self-Consistent-Field Higher-Derivative Methods, Asymmetric Top Molecules. *Chemical Physics* **1988,** *123,* 187-239.

42. Sears, T. J.; Bunker, P. R.; McKellar, A. R. W.; Evenson, K. M.; Jennings, D. A.; Brown, J. M. The rotational spectrum and hyperfine structure of the methylene radical CH_2 studied by far-infrared laser magnetic resonance spectroscopy. *Journal of Chemical Physics* **1982,** *77,* 5348-5362.

APPENDIX A

SUPPLEMENTAL INFORMATION FOR CHAPTER 2

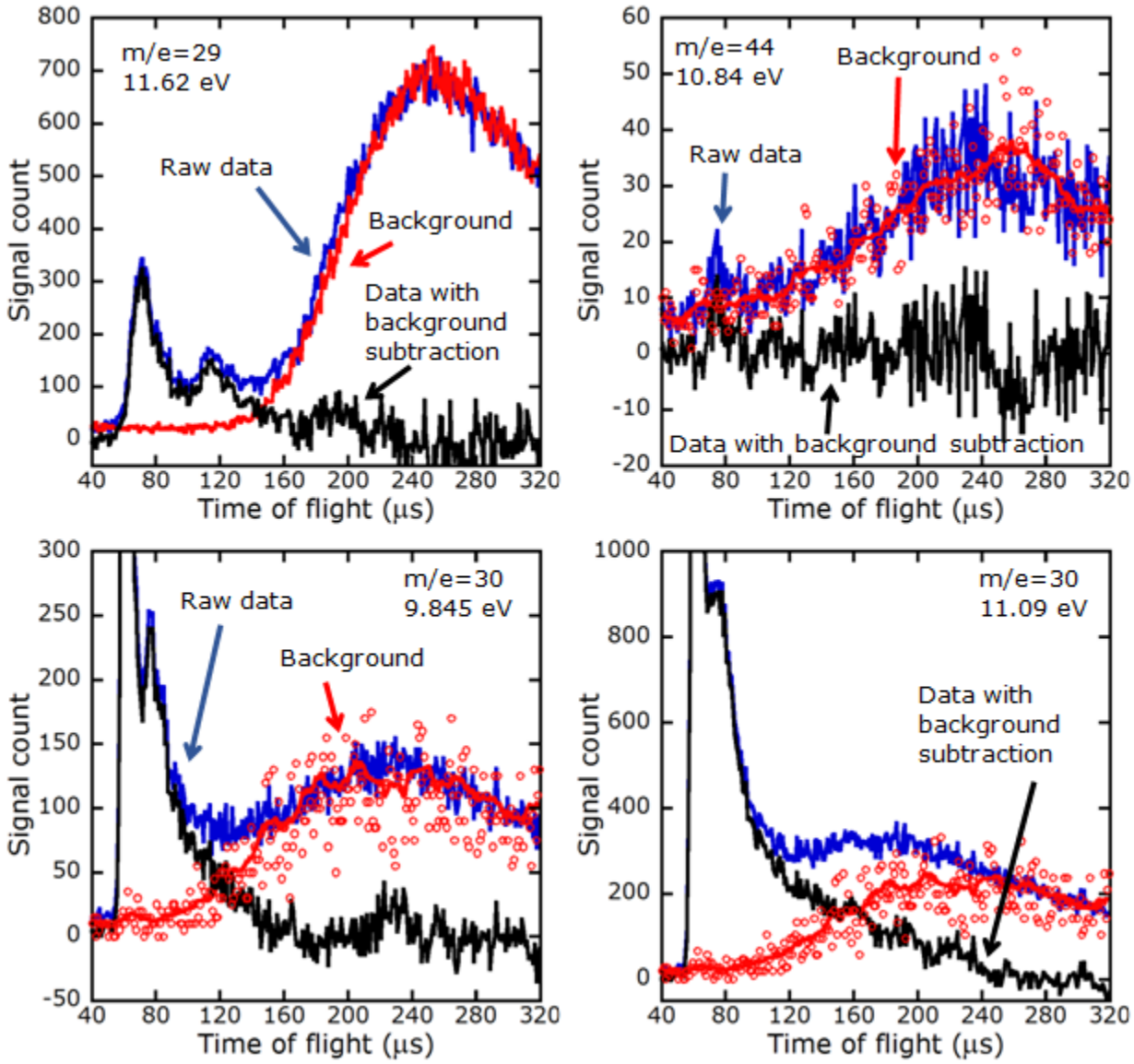

Figure A.1. Laser-independent background signal, and photofragment TOF data with and without subtraction of this background signal. We used the background-subtracted data (black) in our fitting, as the background signal interfered with analysis at these masses; in the main text we present the fits superimposed on the original data (blue). The background signal was determined by collecting a TOF spectrum without firing the photodissociation laser. The background signal is shown as red circles, which were interpolated by a moving average method to remove random noise, giving the solid red line. (At m/e=29 no random noise correction was necessary.) At m/e=30, the photofragment data and background signal were accumulated for different lengths of time, so it was necessary to scale the background signal to match the shape of the photofragment data at long times; at m/e=29 and m/e=44 the two were collected simultaneously, so no such scaling was needed.

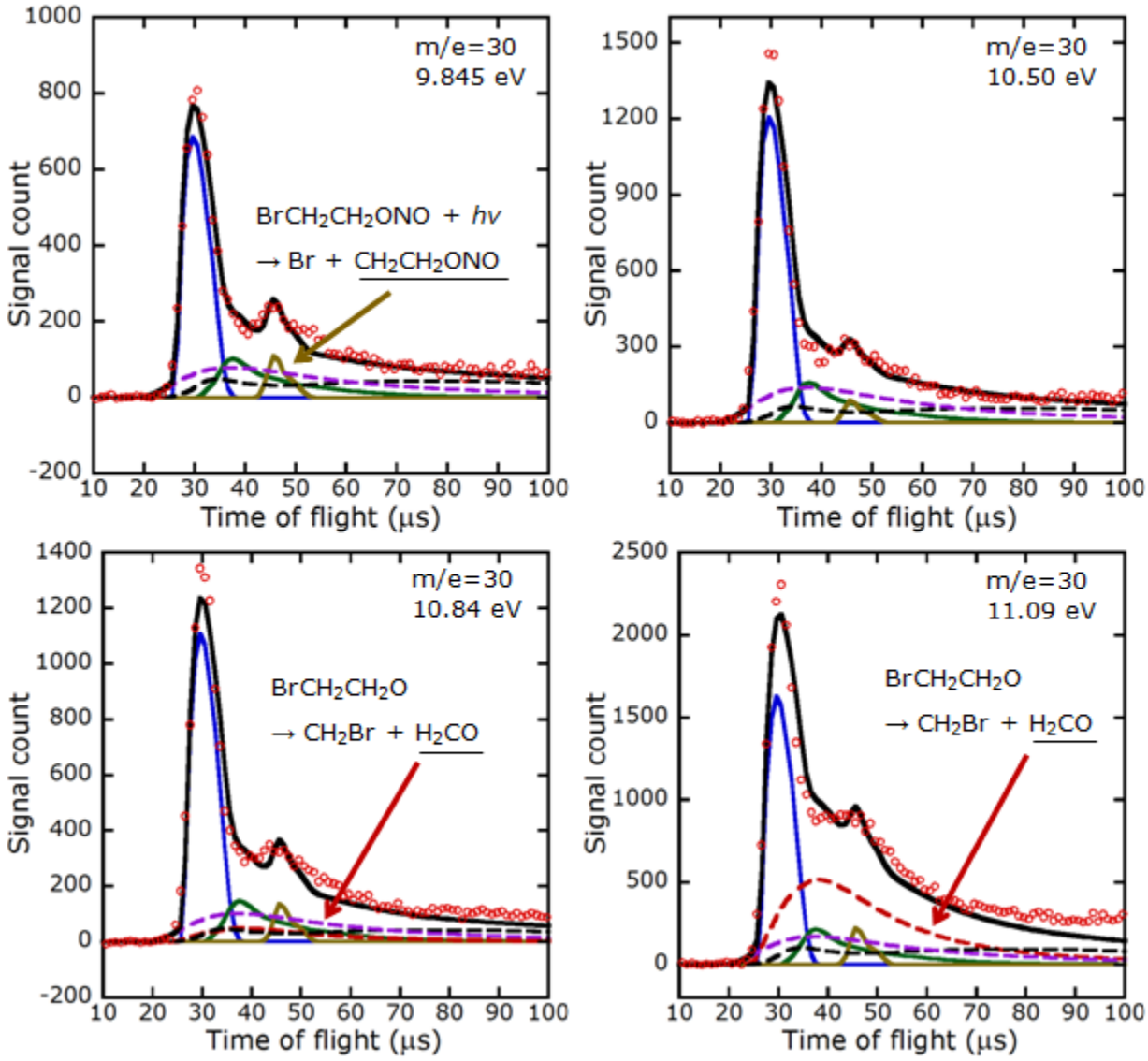

Figure A.2 (five frames; continued on next page).

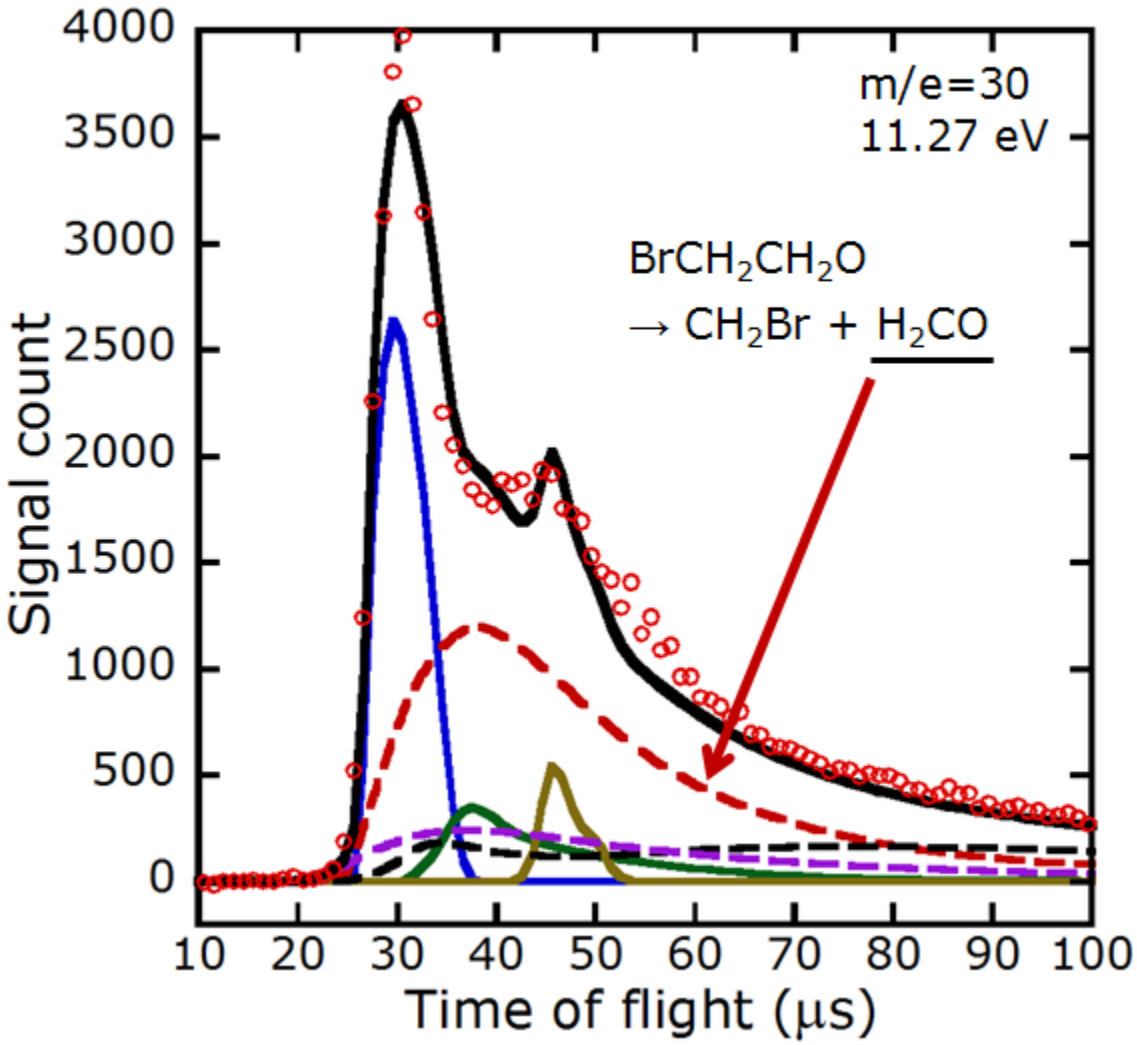

Figure A.2 (five frames; continued from previous page). TOF data and fits for m/e=30 (NO^+, H_2CO^+) at five synchrotron energies. A contribution from H_2CO^+ is not observed at 9.845 and 10.50 eV, and appears weakly at 10.84 eV; this is to be expected, as its photoionization threshold is 10.89 eV (Dodson et al., JPCA 119 (2015), 1279-1291). The contribution from this source increases at higher synchrotron energies, as expected from its increasing photoionization cross section; the contributions from all other channels have been held at a constant ratio, because the different sources of NO are not expected to lead to NO with appreciably different photoionization cross sections. The relative contribution of stable CH_2CH_2ONO radicals has been adjusted in each figure to give the best total fit; this is physically reasonable because the relative photoionization cross section to observe $CH_2CH_2ONO^+$ as NO^+ need not be constant among the energies considered.

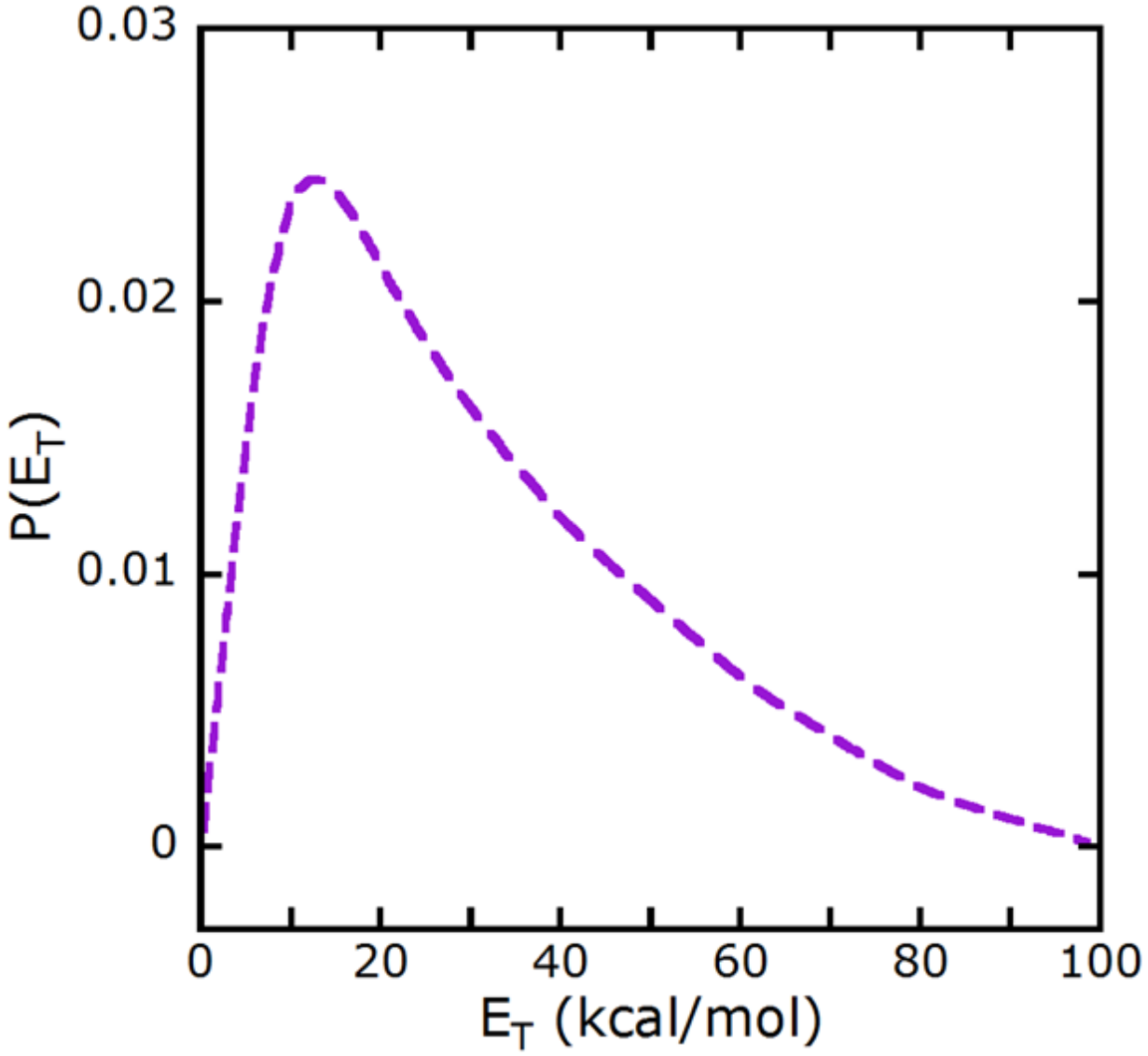

Figure A.3. $P(E_T)$ used for the photodissociation of NO_2 to NO + O. Reproduced from Butler et al., J. Chem. Phys. 79 (1983), 1708-1722.

A.1. Secondary dissociation of HNO to H + NO

Secondary dissociation of primary HNO photofragments is energetically accessible if the dissociation does not partition too much energy into rotations. Any HNO having E_{vib} > 47.5 kcal/mol will undergo secondary dissociation to H + NO (using energies from Active Thermochemical Tables). The contribution of dissociating HNO to the data at m/e=30 is represented by the solid green line in Figure 2.6. The TOF distribution of the signal is fitted using the $P(E_T)$ of Figure 2.5 for photoelimination of HNO from $BrCH_2CH_2ONO$ (the kinetic energy release of the secondary dissociation is safely neglected because, by conservation of momentum, the trajectory of the NO fragment is nearly indistinguishable from the trajectory of the dissociating HNO). NO^+ signal from the dissociative ionization of HNO would have the same predicted TOF distribution, but the signal cannot arise from this source because photoionization at both 9.845 eV and 11.09 eV is below the 11.3 eV adiabatic appearance energy of NO^+ from HNO. (We calculate this value by adding the 47.0 kcal/mol dissociation threshold of HNO to the 9.26 eV ionization threshold of NO.)

The primary photoelimination event produces HNO with a range of E_T, E_{rot}, and E_{vib}. In these experiments we were unable to determine how much of the HNO is formed with sufficient E_{vib} to undergo secondary dissociation. It is noteworthy that the entire HNO photoelimination $P(E_T)$ fits the HNO signal at m/e=31, the NO signal at m/e=30, and the signal due to dissociative ionization of $BrCH_2CHO$ at m/e=29 and m/e=15; this agreement would not be expected if some E_T preferentially led to secondary dissociation of HNO. Nevertheless, it is possible that HNO formed with low E_T does preferentially dissociate, and that the HNO signal at long flight times (~60 μs) arises from secondary dissociation of CH_2CH_2ONO rather than from primary HNO. Further study is required to elucidate the internal energy partitioning of HNO.

A.2. Photodissociation of $BrCH_2CHO$ to produce CH_2Br + HCO

In Figure A.4 we show data acquired at m/e=29 (HCO^+) with a synchrotron energy of 11.62 eV. The major contributions to the data are: dissociative ionization of primary $BrCH_2CHO$ photofragments (solid green line) and of the $BrCH_2CHO$ product of $BrCH_2CH_2O$ (solid blue line); dissociative ionization of the oxirane product of CH_2CH_2ONO (dashed black line); and dissociative ionization of the H_2CO product of $BrCH_2CH_2O$ (dashed red line). A small amount of signal, shown by the dashed green line peaking near 40 μs, is not explained by these other channels. We have attempted to fit it as photodissociation of $BrCH_2CHO$ leading to C-C bond photofission, producing the products CH_2Br + HCO. This follows a suggestion by Nelson et al. (Int. J. Chem. Kinet. 22 (1990), 577-590) that this photofission channel is accessed in the related molecule CCl_3CHO, and is analogous to a C-C bond photofission channel in $ClCH_2CHO$ observed by Adams et al., currently under review for publication in the Journal of Physical Chemistry A. The channel is fitted using an isotropic $I(\theta)$ and the $P(E_T)$ shown in Figure A.5.

We include in the fit at m/e=93 (Figure 2.18) no contribution from the CH_2Br product of this hypothesized photodissociation. We believe that the $BrCH_2CHO$ channel is not competitive with the $BrCH_2CH_2O$ channel, as it contributes little signal to the data at m/e=29, less indeed than is contributed by the energetically unfavorable oxirane channel or dissociative ionization of H_2CO. Also, whereas a significant fraction of $BrCH_2CH_2O$ should dissociate by the lowest-barrier CH_2Br channel, C-C bond photofission in $BrCH_2CHO$ requires an unlikely multiphoton event, which selectively cleaves the C-C bond rather than the C-Br bond; thus the $BrCH_2CH_2O$ channel should dominate. Even so, we did attempt to fit the data at m/e=93 including fragments from photodissociation of $BrCH_2CHO$, but could not derive an acceptable fit with this channel present.

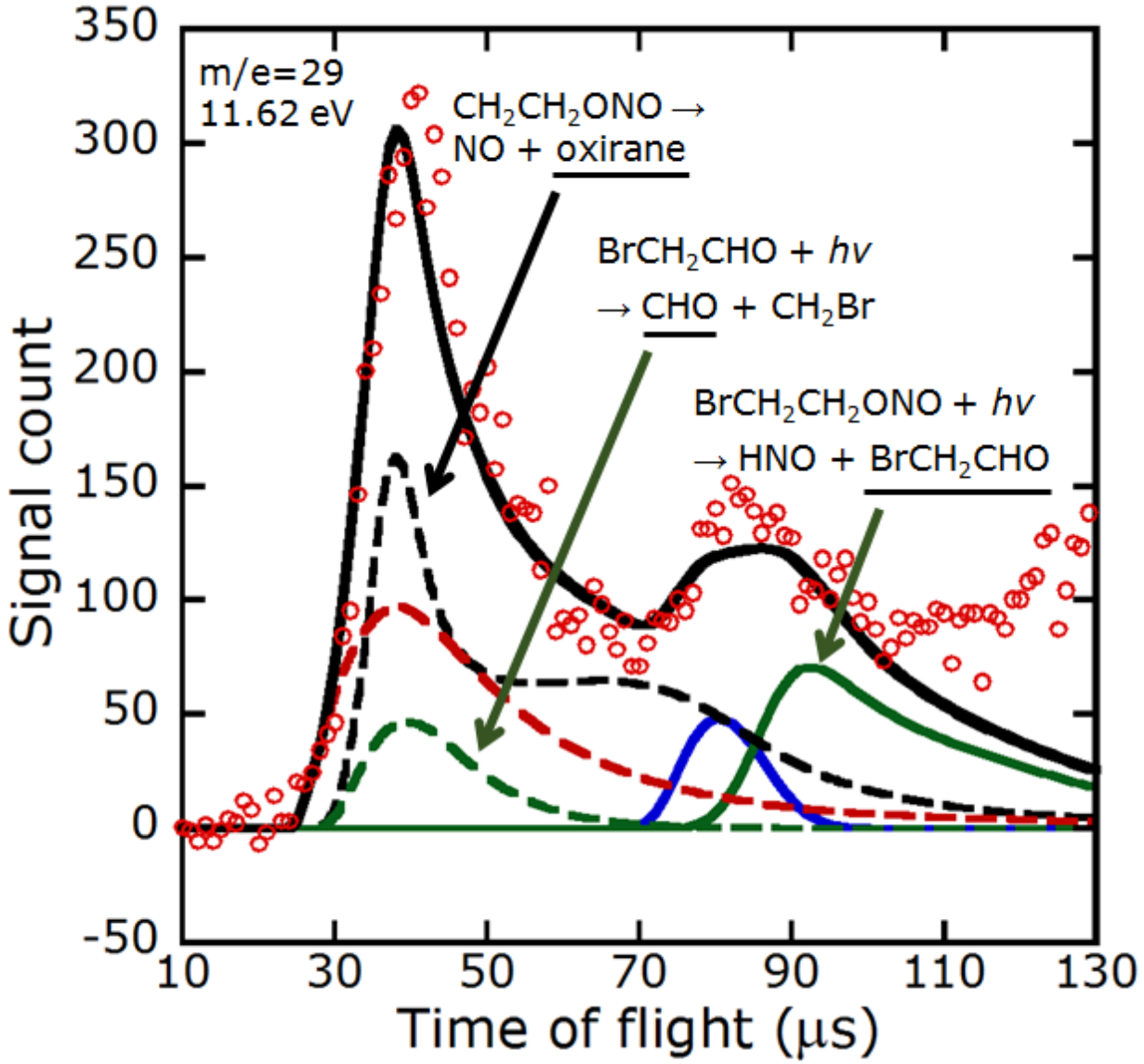

Figure A.4. Time-of-flight spectrum of the signal at m/e=29 (HCO^+) at a synchrotron energy of 11.62 eV. Dissociative ionization of $BrCH_2CHO$ to HCO^+ is apparent (solid blue and solid green lines), as well as dissociative ionization of the oxirane product of CH_2CH_2ONO (dashed black line). Dissociative ionization of the H_2CO product of $BrCH_2CH_2O$ is shown in red dashed line. The contribution of the green dashed line is tentatively assigned to photodissociation of $BrCH_2CHO$, described above.

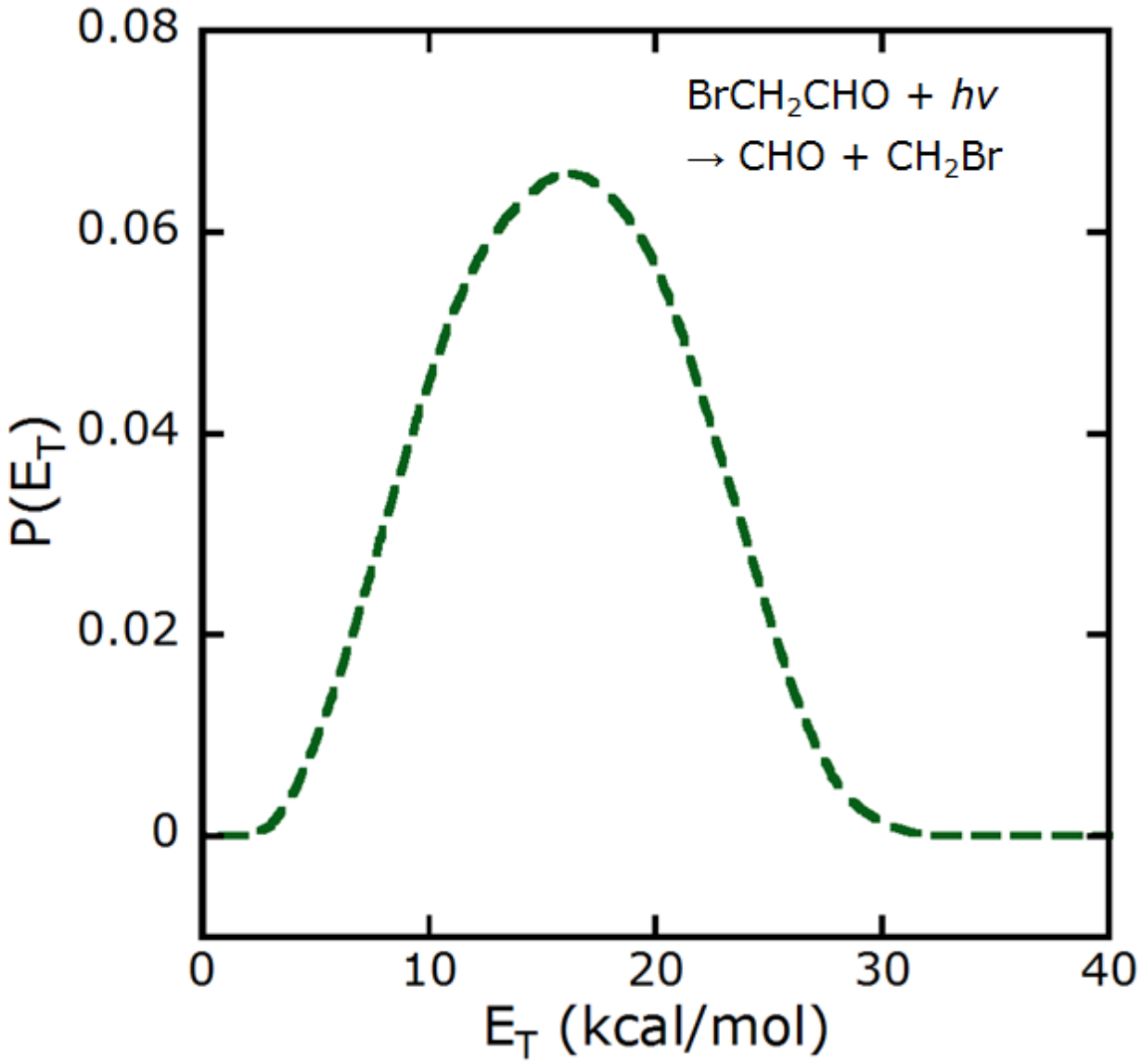

Figure A.5. Photofragment recoil kinetic energy distribution of the secondary photodissociation $BrCH_2CHO + h\nu \longrightarrow CH_2Br + HCO$, derived by forward convolution fitting of the data of Figure A.4.

A.3. Possible sources of HBr fragments

The TOF data of Figure A.6, collected at m/e=82 ($H^{81}Br^+$) with a photon energy of 14.59 eV, seem to evidence some HBr photofragments in this experiment. The source of this signal is not clear. We can fit it as a sum of two sources: secondary photodissociation of $BrCH_2CHO$ to HBr + ketene, as a green line peaking near 80 μs; and a small contribution from secondary dissociation of $BrCH_2CH_2O$ to HBr + vinoxy, as a blue line peaking near 55 μs. The photodissociation pathway from $BrCH_2CHO$ is analogous to the 193 nm photodissociation of $ClCH_2CHO$ leading to HCl + ketene; indeed, to fit this contribution we have used, without modification, the $P(E_T)$ derived by Miller et al. for $ClCH_2CHO$ (J. Chem. Phys. 121 (2004), 1830-1838), which gives a TOF prediction in remarkable agreement with the data.

Data at m/e=42 (ketene) would corroborate this assignment of the m/e=82 signal to photodissociation of $BrCH_2CHO$. We did not collect such data in this experiment; however, we can deduce by the following argument that this m/e=82 signal cannot represent primary photoelimination of HBr from the precursor. Primary photoelimination of HBr from $BrCH_2CH_2ONO$ is conceivable, with vinyl nitrite, CH_2CHONO, as a cofragment. However, CH_2CHONO formed with any physically reasonable kinetic energy release (i.e., below ~90 kcal/mol) would be inconsistent with the other data: the neutral flight time of stable CH_2CHONO would be longer than the observed signal at any of its dissociative ionization products; and its most facile secondary dissociation channel, to vinoxy + NO, could not produce the sharp signal seen at m/e=43. We therefore exclude any possibility of primary HBr photoelimination. Therefore, we infer that the only source of HBr that can account for the data at long time is secondary photodissociation of $BrCH_2CHO$.

Some of the $BrCH_2CH_2O$ radicals should have enough vibrational energy to surmount the

30 kcal/mol barrier to form HBr + vinoxy. The two other channels, having far lower barriers, are expected to be strongly favored; nevertheless, we can ascribe a small part of the signal at m/e=82 to this channel, fitted as the blue line peaking near 55 μs in Figure A.6. The fit was derived by requiring that it also fit the vinoxy data at m/e=43: by conservation of energy, the vinoxy cofragments to HBr must be stable to tertiary dissociation, so they can contribute a small amount to the observed vinoxy signal. We note, however, that the inclusion of this channel in the data at m/e=82 is essentially arbitrary: the other channel, photodissociation of $BrCH_2CHO$ to HBr + ketene, can account for all of the HBr signal with only a small adjustment to its fitted $P(E_T)$, and this photodissociation channel seems more physically reasonable based on the extremely high energetic barrier to dissociation of $BrCH_2CH_2O$ to HBr + vinoxy (see the previous work of Wang et al.).

A.4. Secondary dissociation of $BrCH_2CH_2O$ to $BrCH_2CHO$ + H

$BrCH_2CH_2O$ radicals can undergo secondary dissociation via H loss, producing H + $BrCH_2CHO$. The mass of H is so small compared to $BrCH_2CHO$ that, by conservation of momentum, the $BrCH_2CHO$ fragments have virtually the same velocity as the original $BrCH_2CH_2O$ fragments; thus the $BrCH_2CHO$ from this channel can be treated using only the primary O-NO bond photofission $P(E_T)$. Like the primary $BrCH_2CHO$ fragments described in Chapter 2, this channel also gives signal due to dissociative ionization at m/e=15, 29, and 79, represented by a dark blue line with a neutral flight time near 80 μs in each figure. This secondary source of $BrCH_2CHO$, however, also gives signal at the parent cation of m/e=122 with a synchrotron energy of 13.78 eV; the data and fit are shown in Fig. S8. Interestingly, the primary $BrCH_2CHO$ co-fragment to HNO evidently does not photoionize to give the m/e=122

parent ion; it may be that only vibrationally cold fragments, produced through the secondary dissociation channel, lead to a bound cation at 13.78 eV. This $BrCH_2CHO$ + H channel was also observed in the previous study by its dissociative ionization (under electron bombardment) to m/e=29 and m/e=79.

Many fragments observed in this study form from photodissociation of $BrCH_2CHO$. We have assumed throughout Chapter 2 and this Appendix that photodissociation occurs exclusively in the primary $BrCH_2CHO$ co-fragments to HNO, not in the secondary fragments of this channel. The primary fragments, being vibrationally hot, might be expected to have a higher photoabsorption cross section than the vibrationally cold $BrCH_2CHO$ of this secondary channel. Nevertheless, it must be noted that the velocity distributions of the photoproducts of $BrCH_2CHO$ are essentially identical from either source, as the velocity distributions of the $BrCH_2CHO$ themselves are quite similar. It was therefore impossible in this experiment to discriminate between photodissociation of the $BrCH_2CHO$ formed in these two channels.

A.5. Statistical justification for photodissociation of $BrCH_2CHO$

In Chapter 2, we ascribe the vinoxy signal to photodissociation of $BrCH_2CHO$, not to secondary dissociation due to vibrational excitation; this point bears some justification. We calculate that the endoergicity of the transformation $BrCH_2CHO \rightarrow Br + CH_2CHO$ is ΔH_{0K} = 60.3 kcal/mol with negligible barrier above the endoergicity. Any $BrCH_2CHO$ with $E_{vib} > 60.3$ kcal/mol will therefore dissociate, and any excess E_{vib} will be distributed statistically among the $3N-6 = 15$ vibrational degrees of freedom, one of which can be taken as the dissociation coordinate. The $P(E_T)$ observed for this dissociation (Figure 2.15) evidences a large partitioning of energy into the dissociation coordinate, $\langle E_T \rangle \sim 30$ kcal/mol; whereas the total energy

available to the $BrCH_2CHO$ fragments is less than 140 kcal/mol (see the discussion of photoelimination of HNO from the precursor), so the excess E_{vib} cannot exceed 140 – 60.3 = 80 kcal/mol. Thus, secondary dissociation of $BrCH_2CHO$ to Br + CH_2CHO with the observed E_T would require the partitioning of a very large fraction of the available energy, 30 kcal/mol out of a maximum below 80 kcal/mol, into a single one of the 15 degrees of freedom. Such an event is statistically quite unlikely. Rather, the large kinetic energy release should be attributed to photofission of the C-Br bond when the $BrCH_2CHO$ absorbs a 193 nm photon.

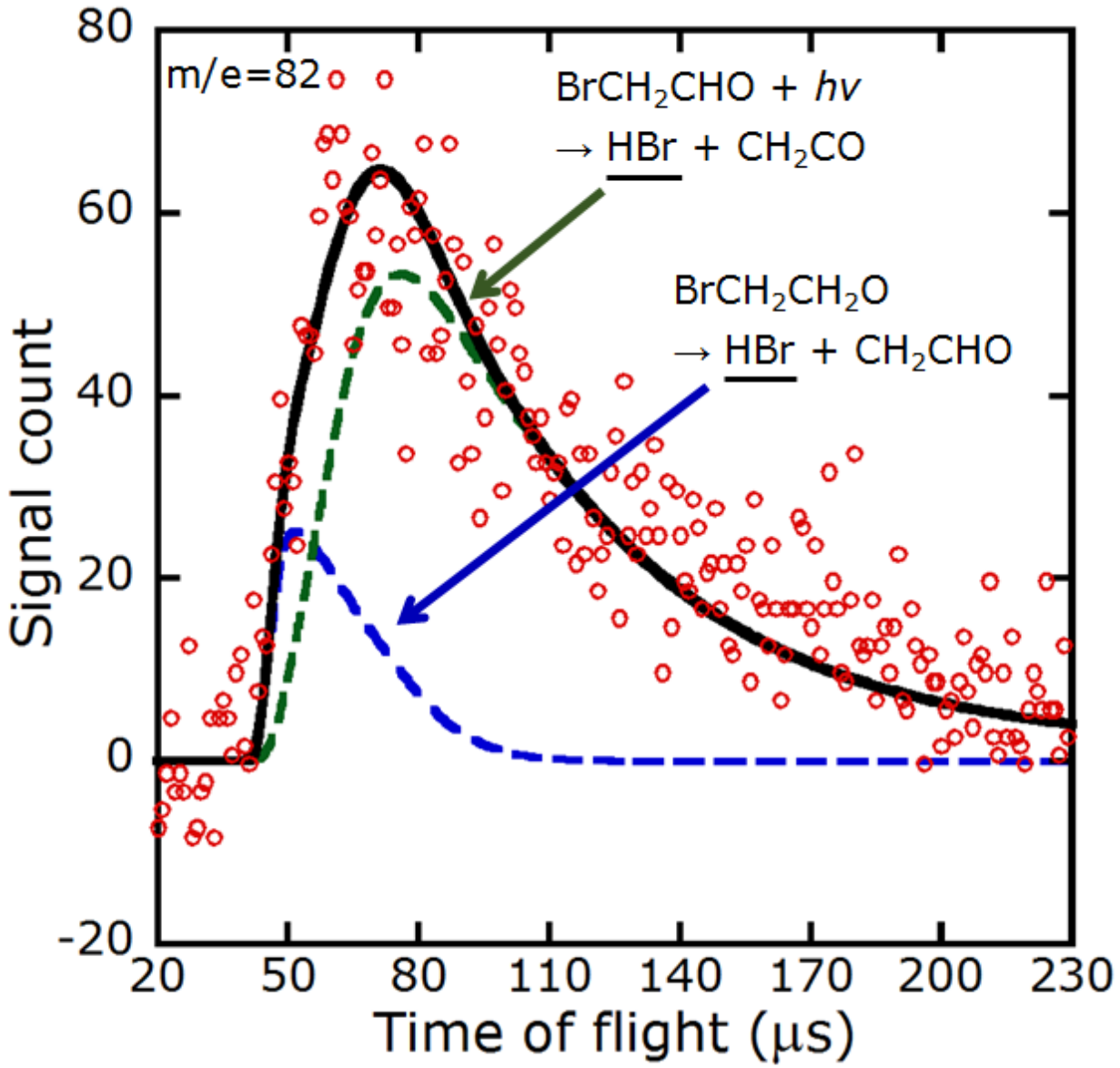

Figure A.6. Time-of-flight spectrum of m/e = 82 ($H^{81}Br^{+}$) signal at a photoionization energy of 14.59 eV. The fits are somewhat arbitrary; for details see the preceding paragraphs of this document.

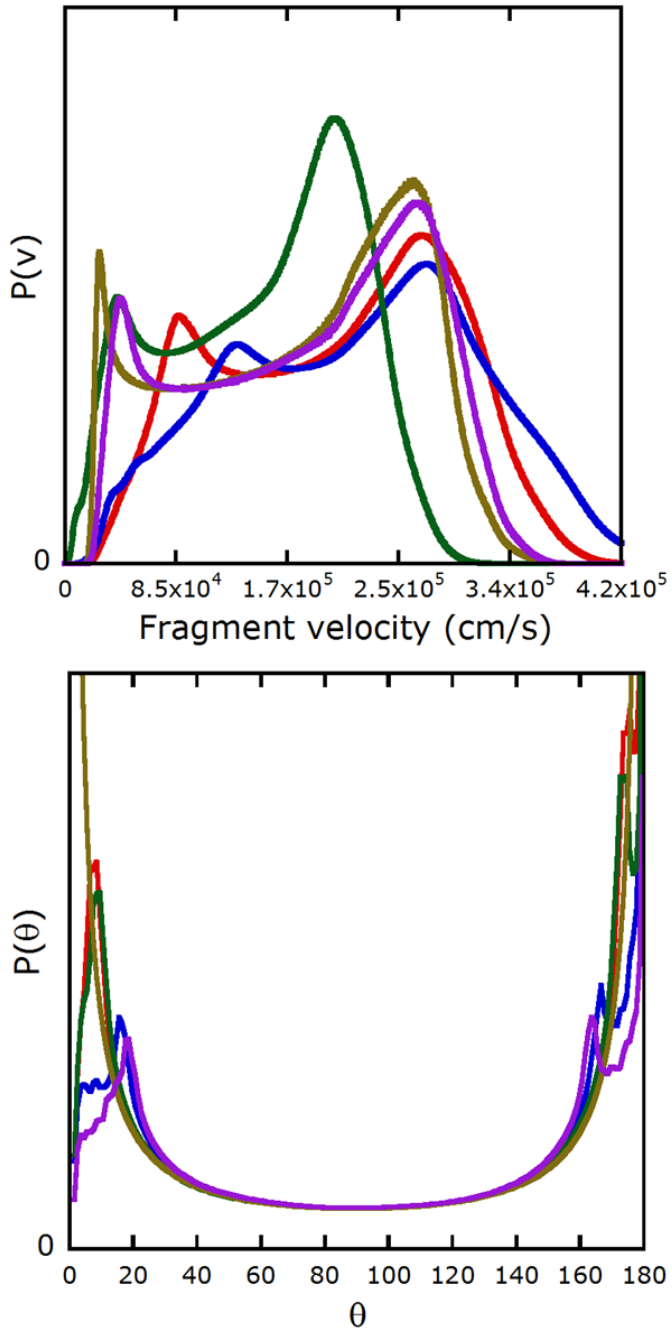

Figure A.7. Predicted speed distributions for the ethene fragments of dissociation of CH_2CH_2ONO to NO_2 + ethene, and predicted angular distributions of the NO_2 fragment of this dissociation, where 0 degrees represents scattering in the direction of the velocity of the dissociating CH_2CH_2ONO fragment. The different colors correspond to dissociation of CH_2CH_2ONO that was formed by photodissociation of each of the four precursor conformers, and from photodissociation of the *anti-trans* precursor conformer that isomerizes to *cis*-CH_2CH_2ONO before dissociation. These results were not used directly in our analysis: the speed distributions in particular show a spuriously large likelihood of low-velocity fragments, which is inconsistent with the data. The predictive model does not account for forces along the exit barrier of the reaction, which may explain this discrepancy.

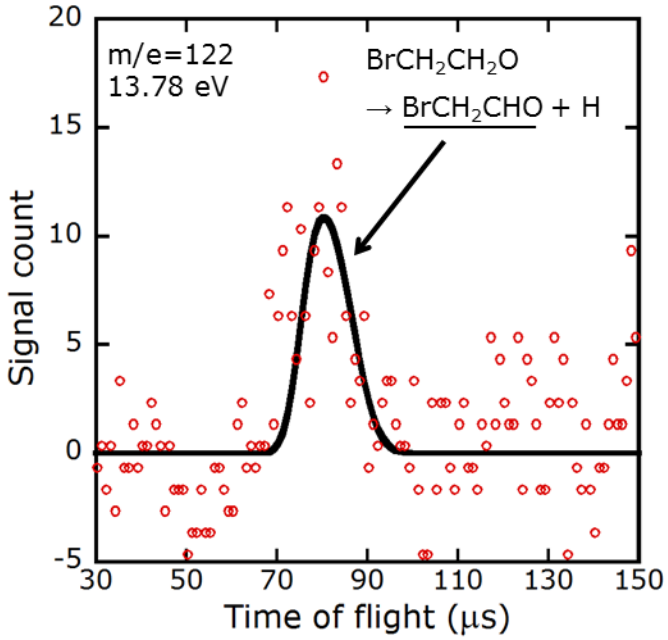

Figure A.8. Time-of-flight spectrum and fit of m/e = 122 ($BrCH_2CHO^+$) signal at a photoionization energy of 13.78 eV. This fit is produced using the distribution of recoil kinetic energies, $P(E_T)$, for primary photodissociation of $BrCH_2CH_2ONO$ leading to NO + $BrCH_2CH_2O$ to determine the velocity of dissociating $BrCH_2CH_2O$ radicals; because the departing H atom has such a low mass, the $BrCH_2CHO$ fragments have nearly the same TOF distribution as the dissociating $BrCH_2CH_2O$.

A.6. Cartesian coordinates of stationary points of CH_2CH_2ONO

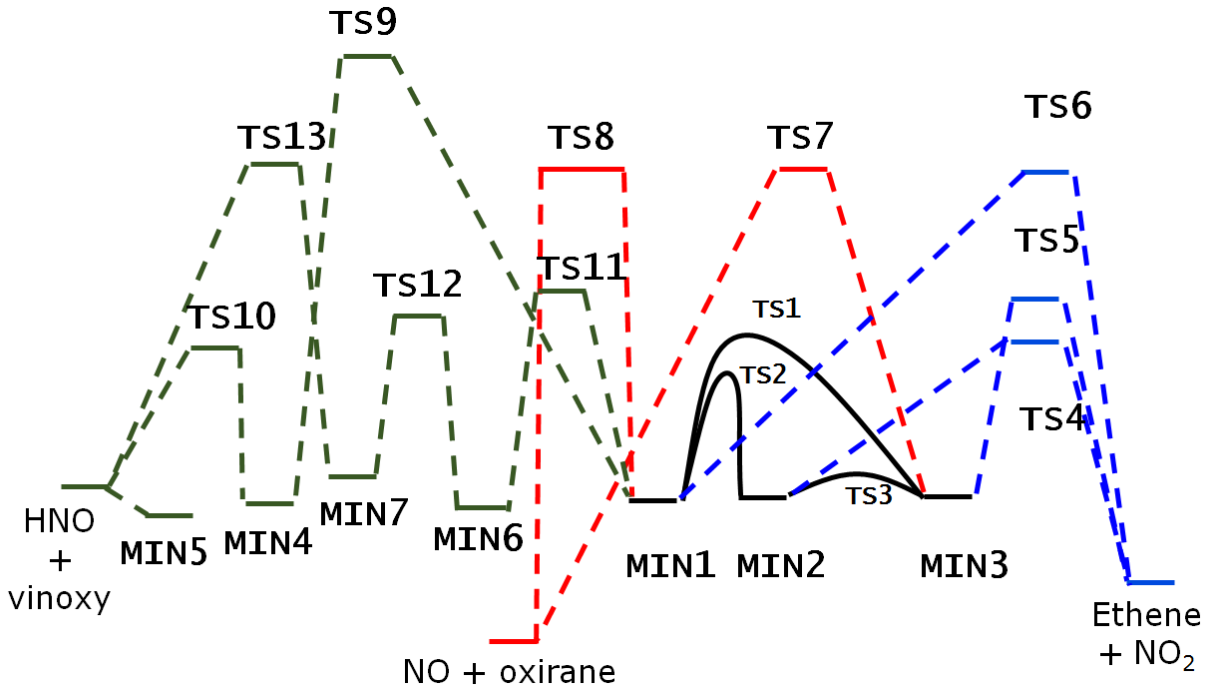

MIN1				MIN2			
C	-1.105570	0.551285	0.088111	C	1.650461	0.629167	-0.294798
C	-2.130487	-0.511477	0.065184	H	2.192879	0.342520	-1.184000
H	-1.857782	-1.530614	0.295767	C	0.940943	-0.393854	0.495370
H	-3.166395	-0.274822	-0.123778	H	1.566806	1.677214	-0.053708
H	-1.426412	1.434127	-0.467140	O	-0.217511	-0.971273	-0.221831
H	-0.856997	0.872322	1.108571	H	0.585849	-0.008444	1.448838
O	0.122519	0.092519	-0.520480	H	1.546830	-1.283646	0.661203
N	1.183855	0.094873	0.419993	N	-1.355153	-0.189496	-0.293809
O	2.182098	-0.268015	-0.063663	O	-1.276828	0.869641	0.219443
MIN3				**MIN4**			
C	-0.793360	0.475479	-0.000002	C	0.911358	0.319415	0.003662
C	-2.198970	0.037533	0.000006	C	2.224249	0.131612	0.016225
H	-2.704064	-0.186858	0.927349	H	2.665190	-0.854055	-0.015755
H	-2.704101	-0.186777	-0.927336	H	2.879320	0.988078	0.046212
H	-0.531245	1.055905	-0.884946	H	0.429326	1.286048	0.028205
H	-0.531233	1.055899	0.884944	H	-1.839981	-1.214135	-0.208377
O	0.049369	-0.736628	-0.000009	O	0.058321	-0.743237	-0.079928
N	1.420223	-0.530190	-0.000002	N	-1.337981	-0.404521	0.167576
O	1.761014	0.598514	0.000006	O	-1.756023	0.733180	-0.062902

MIN5			MIN6		
C	-1.239213	0.201530 -0.000086	C	-1.414875	-0.077708 0.059145
O	-0.655413	-0.887345 -0.000110	C	-0.399614	1.060679 0.019614
C	-2.654402	0.310335 0.000105	H	-0.476859	1.809498 -0.764481
H	-0.654413	1.133284 -0.000219	H	-0.183293	1.523508 0.981190
H	1.500666	-0.945330 0.000155	H	-1.989801	-0.165481 0.979208
O	2.157617	0.758808 -0.000033	H	-2.072107	-0.139859 -0.808156
N	2.413466	-0.417411 0.000105	O	-0.366455	-1.071593 0.008094
H	-3.258740	-0.586373 0.000229	N	0.630424	0.014096 -0.288803
H	-3.137723	1.277403 0.000126	O	1.765958	-0.056428 0.137070
MIN7			TS1		
C	1.293120	0.368331 0.180757	C	2.236026	0.093419 -0.206720
C	-0.096162	0.762982 -0.323593	C	0.913528	0.300742 0.411437
H	-0.257937	1.828834 -0.133072	O	-0.034683	-0.578550 -0.266165
H	-0.235992	0.537085 -1.381496	N	-1.399338	-0.395637 0.288056
H	2.052687	1.038642 -0.265211	O	-1.965593	0.463884 -0.242024
H	1.392571	0.544449 1.264790	H	0.571533	1.333160 0.276010
O	1.682381	-0.897531 -0.115294	H	0.921334	0.063496 1.477825
N	-1.128985	0.067897 0.495249	H	3.006789	-0.468530 0.298090
O	-1.961154	-0.503990 -0.146549	H	2.400596	0.393690 -1.231105
TS2			TS3		
C	-1.818617	-0.656237 -0.047320	C	-2.013927	-0.280024 -0.364600
H	-1.883380	-0.920846 -1.092233	H	-2.932399	0.267205 -0.216867
C	-0.999293	0.503095 0.374395	C	-0.876520	-0.122474 0.559234
H	-2.470461	-1.146887 0.661046	H	-1.896819	-0.851846 -1.273677
O	0.124817	0.752550 -0.475392	O	0.092848	0.832273 -0.016695
H	-0.668178	0.402899 1.415965	H	-0.350282	-1.059732 0.735131
H	-1.567097	1.442274 0.323309	H	-1.165498	0.314696 1.512677
N	1.095112	-0.397531 -0.422493	N	1.398234	0.400545 -0.268345
O	1.854032	-0.262034 0.436255	O	1.644658	-0.714666 0.010863
TS4			TS5		
C	1.652709	0.625325 -0.289331	C	2.245164	-0.024549 -0.000004
H	2.158570	0.470895 -1.231851	C	0.996283	0.584874 0.000004
H	1.474372	1.640775 0.028440	O	-0.223844	-0.833558 0.000002
C	1.161198	-0.454655 0.444107	N	-1.455133	-0.492618 -0.000001
H	1.583104	-1.434480 0.267390	O	-1.776202	0.658164 -0.000002
H	0.832296	-0.274187 1.458592	H	2.730866	-0.304340 -0.923686
O	-0.461197	-1.011890 -0.217614	H	2.730876	-0.304343 0.923675
N	-1.393109	-0.143201 -0.204118	H	0.637937	1.049101 0.908617
O	-1.186306	0.958812 0.214814	H	0.637933	1.049112 -0.908601
TS6			TS7		
C	-2.059582	0.624037 -0.140423	C	2.014883	-0.029468 0.363981
C	-1.569670	-0.537113 0.364667	C	0.884527	0.627167 -0.291044
O	0.371574	-0.488113 -0.500382	O	0.273370	-0.641950 -0.296699
N	1.125724	0.232183 0.297551	N	-1.523717	-0.580397 0.019722
O	2.289927	0.200189 0.007353	O	-1.884952	0.494397 0.196107
H	-1.762578	-1.481964 -0.121222	H	1.061953	1.021863 -1.292704
H	-1.164851	-0.581462 1.364436	H	0.337395	1.356777 0.314890
H	-1.926856	1.562283 0.380001	H	1.989570	-0.197523 1.428660
H	-2.542285	0.657720 -1.107301	H	2.773285	-0.524101 -0.221789

TS8				TS9			
C	2.075725	-0.483652	0.173151	C	-0.877770	0.022377	0.433557
C	1.222234	0.687950	-0.033892	O	-0.124625	1.006942	-0.041810
O	0.184655	-0.223846	-0.309239	H	-0.792205	-0.198367	1.509371
N	-1.467149	0.412261	0.195302	C	-2.095133	-0.345295	-0.182568
O	-2.265645	-0.373320	-0.019278	H	-0.100558	-0.977987	0.030241
H	1.476662	1.320085	-0.886701	N	1.142868	-0.284678	-0.454049
H	1.029499	1.297823	0.851749	O	2.102785	-0.240130	0.168191
H	2.074130	-0.986177	1.127242	H	-2.748233	-1.072156	0.280792
H	2.549913	-0.966020	-0.666824	H	-2.346946	0.044271	-1.159042
TS10				TS11			
C	0.955946	-0.211475	0.130440	C	1.323881	-0.410369	0.051608
C	2.312050	-0.265354	-0.111971	C	1.035609	1.045130	-0.099305
H	2.856649	0.628696	-0.379416	H	1.326160	1.763282	0.653380
H	2.851818	-1.192186	0.013648	H	0.828912	1.427900	-1.089809
H	0.417755	-1.137378	0.376726	H	1.980851	-0.814004	-0.722172
H	-1.843085	1.026114	0.577081	H	1.736824	-0.658991	1.031650
O	0.286314	0.864008	0.106950	O	0.034864	-1.011364	-0.136441
N	-1.622569	0.390075	-0.228817	N	-0.790127	0.137740	0.364908
O	-1.852955	-0.763359	0.005908	O	-1.847214	0.199998	-0.131212
TS12				TS13			
C	-1.389879	0.268861	-0.066460	C	-1.102603	0.199865	-0.342666
C	-0.060356	0.989568	0.112101	C	0.066370	0.910517	0.395740
H	0.113544	1.862077	-0.522269	H	0.139039	1.975587	0.187621
H	0.198316	1.215830	1.145219	H	0.133432	0.675268	1.454410
H	-2.106216	0.568909	0.713206	H	-1.603935	0.818469	-1.107307
H	-1.849549	0.470885	-1.041956	H	-0.199456	-0.337630	-1.143435
O	-1.069999	-1.063790	0.115402	O	-1.746019	-0.709387	0.255791
N	0.825025	-0.145179	-0.361989	N	1.066015	0.145597	-0.409754
O	1.891266	-0.267712	0.130333	O	1.781796	-0.642259	0.139027

APPENDIX B

SUPPLEMENTAL INFORMATION FOR CHAPTER 3

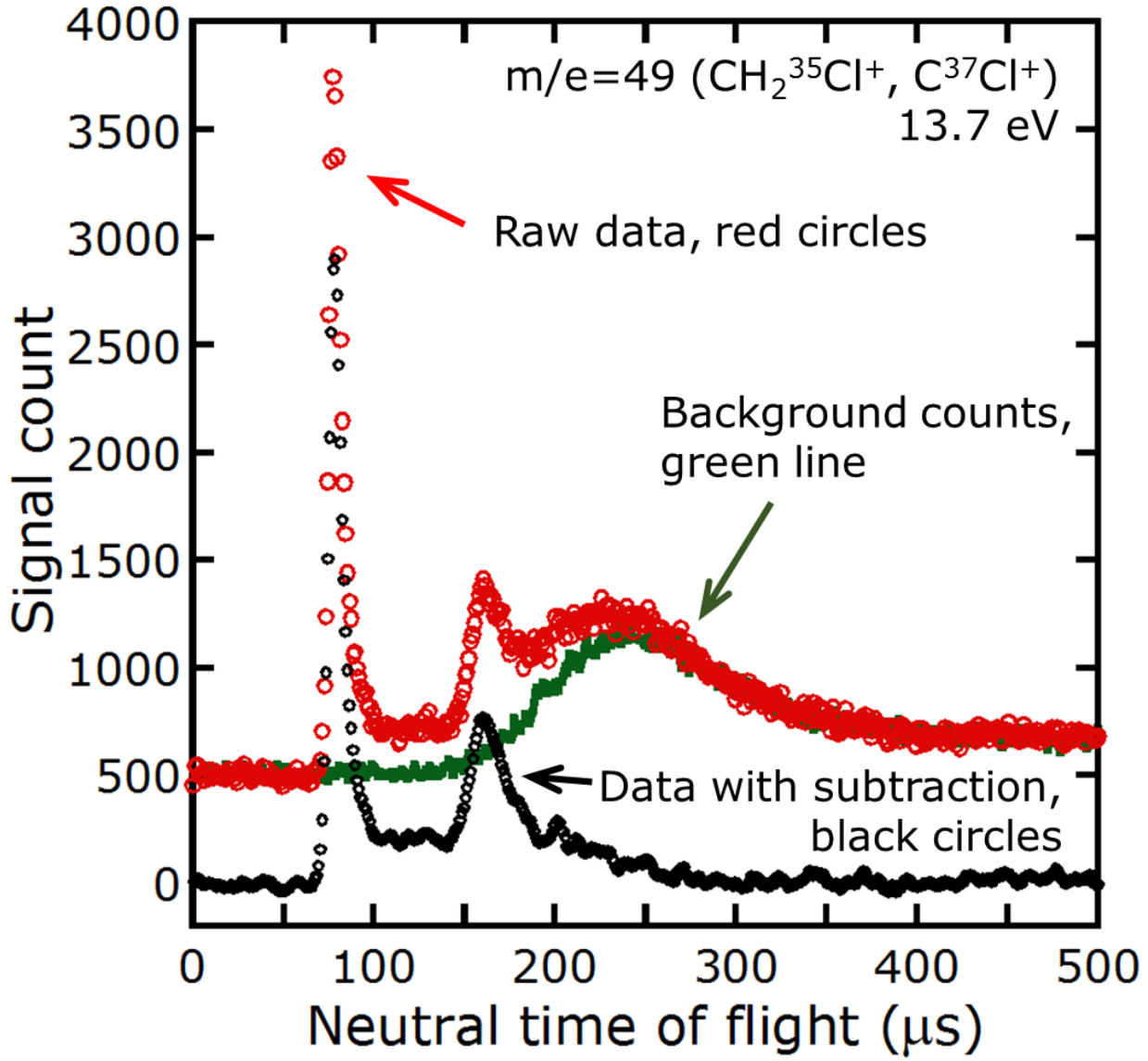

Figure B.1. Raw data, background counts, and background-subtracted data collected at *m/e*=49. The background signal (solid green line) arises from the molecular beam but not from the photolysis laser; this signal was accumulated by running the instrument without the laser firing. Background subtraction was performed by normalizing the red and green distributions to the same baseline (~500 counts), then scaling the green distribution such that subtracting the green from the red gave a net zero signal at long times. The distribution shown as black circles is the result of subtraction of the green distribution from the red data.

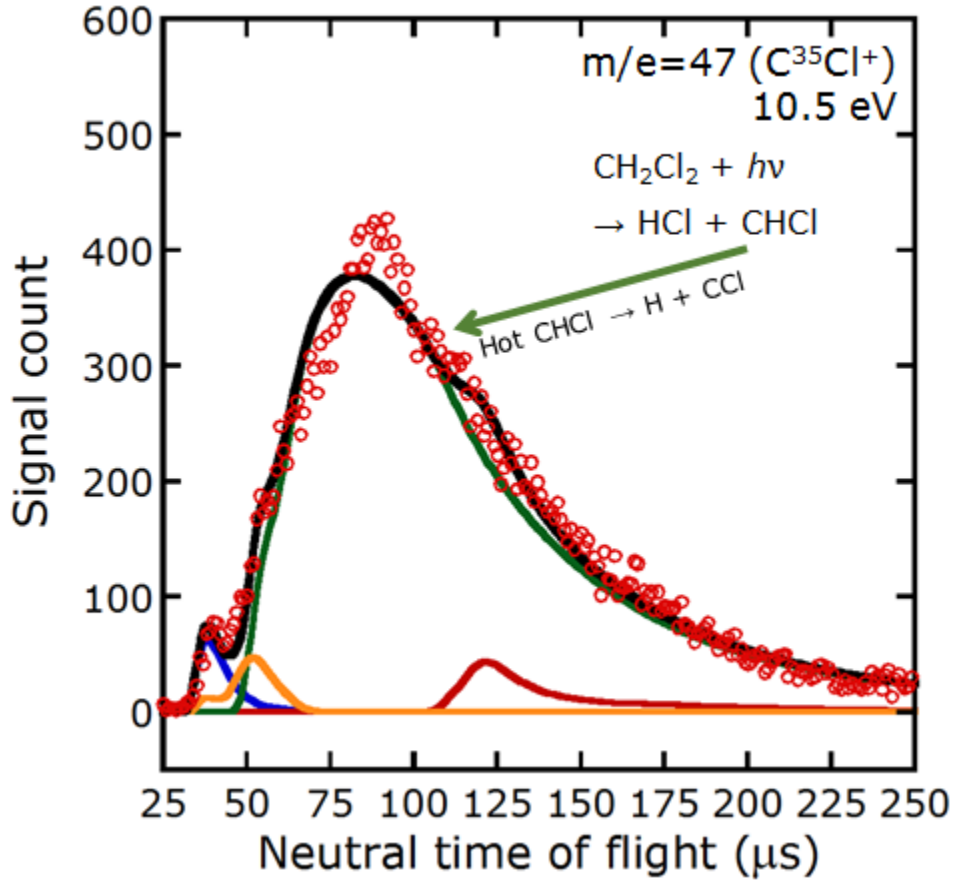

Figure B.2. Time-of-flight data collected at *m/e*=47 ($C^{35}Cl^+$). As usual, some ions of the next higher mass unit, *m/e*=48 ($CH^{35}Cl^+$), are also detected. The contribution fitted by a solid green line roughly represents $C^{35}Cl$ fragments formed by secondary dissociation of vibrationally hot CHCl photofragments. Note that the green curve is actually the TOF distribution of neutral CHCl fragments, which does not include the additional velocity—and thus, broadening of the TOF distribution—imparted in the secondary dissociation event CHCl → H + CCl. The fit can be improved by supposing that this secondary dissociation has a kinetic energy release of up to a few kcal/mol. This improvement to the fit is not attempted here, since the kinetic energy release accompanying H-loss varies significantly with the kinetic energy release of the initial C–Cl photofission event. An alternative improvement can be made by adjusting the partitioning of the HCl photoelimination P(E_T), namely, by reducing the fast tail of the green partition.

Curves of other colors have the same meanings as elsewhere in this report: blue, presumed tiny dissociative ionization of CH_2Cl; orange, vibrationally stable CHCl (*m/e*=48); dark red, presumed dissociative ionization of $CHCl_2$ photofragments.

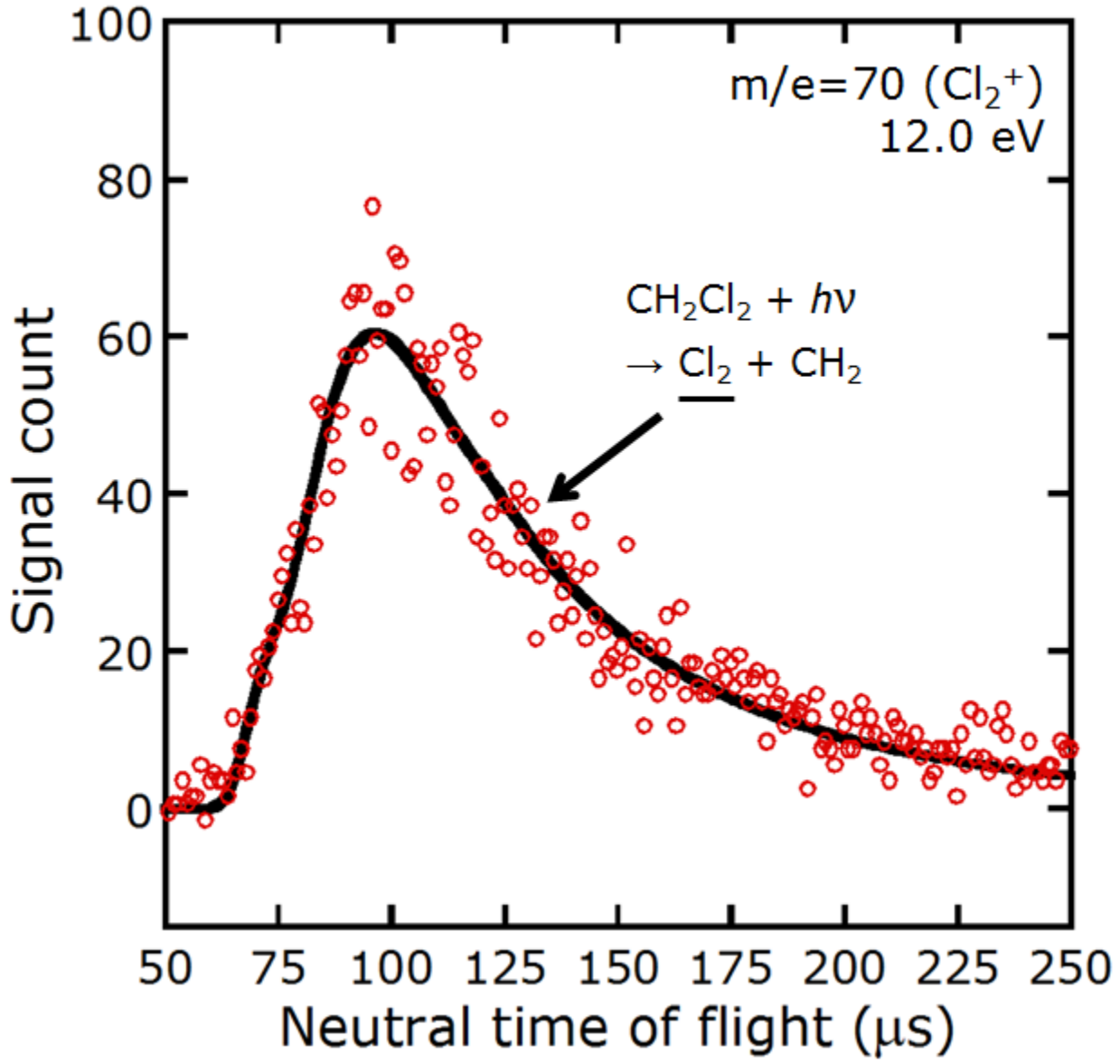

Figure B.3. Time-of-flight distribution of data collected at *m/e*=70 (Cl_2^+). The signal intensity is exceptionally small compared to the data at *m/e*=35, 38, and 49, indicating that although this pathway is accessed, it is utterly insignificant. The P(E_T) giving this TOF distribution is shown in Figure B.5.

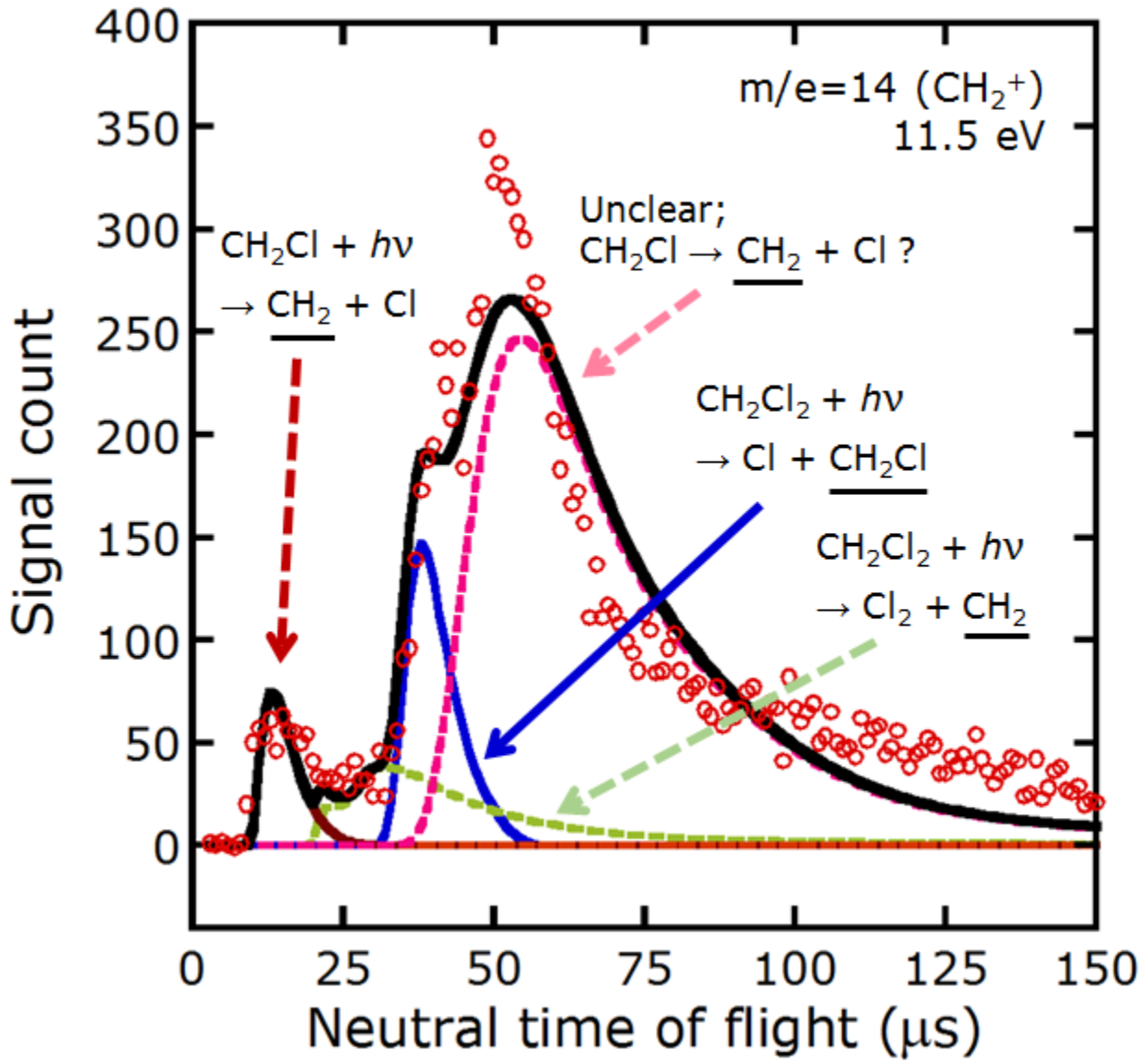

Figure B.4. Time-of-flight data and tentative forward convolution fits to data collected at *m/e*=14 (CH_2^+). Some of the signal has a clear origin; the figure is described on the following page.

(Figure B.4, continued.) The fastest fragments have such a large kinetic energy that they must, by conservation of energy, arise from a two-photon process; clearly the only two-photon process that can produce CH_2 involves the secondary photodissociation $CH_2Cl + h\nu \rightarrow CH_2 + Cl$. The $P(E_T)$ for this secondary photodissociation channel is shown in Figure B.6.

The dashed green curve with a maximum near 30 μs arises from primary CH_2 photofragments, which are momentum-matched to the Cl_2 fragments with TOF data shown in Figure B.4. The visibility of the dashed green curve, which represents an exceedingly minor photodissociation channel, suggests that the total production of CH_2^+ ions is quite small.

The largest part of the signal, peaking near 60 μs, is from an unknown source. The hypothetical fit, shown as a dashed pink line, assumes that some of the slowest primary CH_2Cl photofragments (primary $E_T \approx 10$ kcal/mol) can undergo secondary dissociation to $CH_2 + Cl$. This hypothesis is consistent with the observed signal intensity: since there are almost no CH_2Cl photofragments with a sufficiently low E_T to dissociate in this manner, the signal arising from this channel would be miniscule, perhaps of the same order of magnitude as the minor primary Cl_2 photoelimination channel.

Likewise, the solid blue curve arises from presumed dissociative ionization of a tiny fraction of the CH_2Cl fragments.

An alternative explanation for the poorly-fit data is that the true $P(E_T)$ for $Cl_2 + CH_2$ photoelimination events cannot be reliably determined from the Cl_2 data, and thus the dashed green curve in this figure is not the true TOF distribution of CH_2 photofragments. This hypothesis is not unreasonable: the partial photoionization cross section of Cl_2 varies wildly (up to 50%) near its ionization threshold, so different vibrational states of Cl_2—which may be more or less easily ionized—may be under- or over-represented in the TOF data, especially given the large bandwidth of the synchrotron radiation.

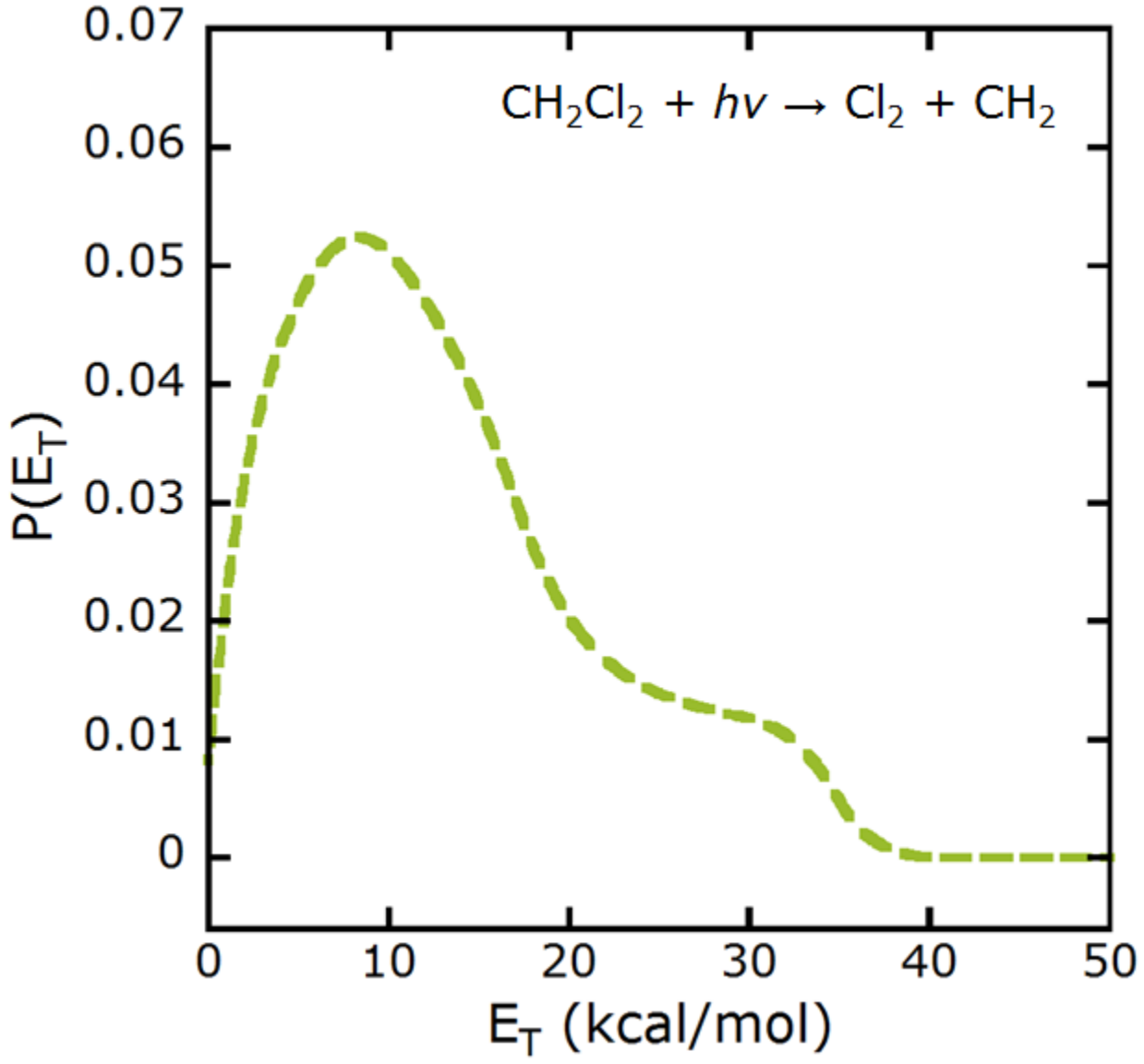

Figure B.5. Fitted recoil kinetic energy distribution of the primary Cl_2 photoelimination channel. This P(E_T) gives the TOF distributions fitted by the solid black line in the *m/e*=70 data of Figure B.3, and the dashed green lines in the *m/e*=14 data of Figure B.4.

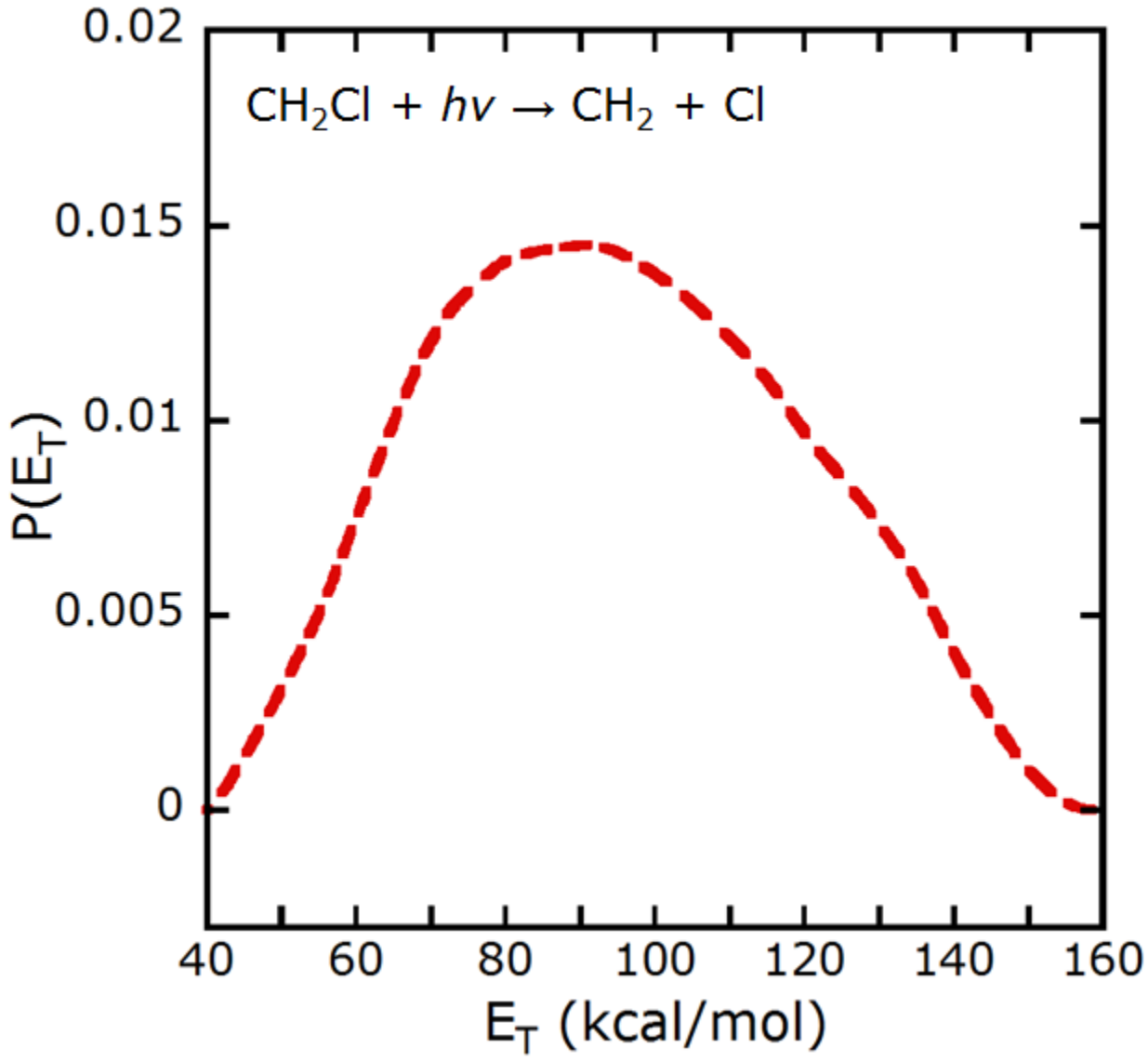

Figure B.6. Fitted recoil kinetic energy distribution of the secondary photodissociation of CH_2Cl to CH_2 + Cl. This P(E_T) is used to fit the fastest signal in the *m/e*=14 data of Figure B.4.